SSI-DT46195036

Doctoral Thesis

Study on model order reduction for Maxwell's equations based on Krylov subspace methods

Shingo Hiruma

February, 2021

Course of Systems Science and Informatics
Graduate School of Information Science and Technology
Hokkaido University

Doctoral Thesis
submitted to Graduate School of Information Science and Technology,
Hokkaido University
in partial fulfillment of the requirements for the degree of
Doctor of Philosophy.

Shingo Hiruma

Thesis Committee: Professor Hajime Igarashi (Chief examinar)
Professor Yuh Yamashita
Professor Hiroyuki Kita
Associate Professor So Noguchi

Study on model order reduction for Maxwell's equations based on Krylov subspace methods*

Shingo Hiruma

Abstract

With the recent development of the power electronics devices, the evaluation of the eddy current losses in the electromagnetic apparatuses has become significant for the designers because the high-frequency components in the power supply induce non-negligible losses. Although the finite element method (FEM) is useful to evaluate the eddy current losses, it is sometimes difficult to perform the FE analysis (FEA) when we consider the high-frequency component. Since the skin depth becomes significantly small at high-frequency, we have to subdivide the conducting domains into fine elements. As a result, we have an unsolvable size of the FE equation.

To circumvent this problem, model order reduction (MOR) techniques are developed to reduce the computational costs and time in the eddy current analysis. In this paper, new MOR techniques are presented to

1. generate a reduced-order model that is equivalent to the Cauer circuit of the electric apparatuses,
2. accelerate the homogenization method by reducing the unknowns,
3. consider the inductive and capacitive effects simultaneously.

Chapter 3 discusses a new MOR technique that allows us to obtain a Cauer circuit from a given system. Chapter 4 discusses the use of the proposed method in the homogenization method. We apply it to the FE equation of a unit cell, Dowell's equation, and homogenization FEA. Chapter 5 discusses the application of the proposed method to the Darwin model of Maxwell's equations.

Keywords: Cauer circuit, complex permeability, Darwin model, homogenization method, Krylov subspace methods, Lanczos process, Maxwell's equations, model order reduction (MOR), Stieltjes continued fraction

* Doctoral Thesis, Course of Systems Science and Informatics, Graduate School of Information Science and Technology, Hokkaido University, SSI-DT46195036, February 12, 2021.

Contents

List of Figures

List of Tables

Chapter 1.

Introduction

1.1 Background

Electromagnetic apparatuses such as motors, reactors, and inductors are essential industrial products because they are used in various fields of modern society. As a result, the power consumed by electromagnetic apparatuses accounts for a large percentage of total power consumption [1]. In response to the recent global warming issues, there is a strong demand for more efficient and energy-saving electromagnetic apparatuses. Consequently, environmental regulations are being tightened. To meet these strict regulations, designers have to optimize the system and minimize the total losses. Therefore, it becomes increasingly difficult to design electromagnetic apparatuses based on the experience of the designers, and the use of computer-aided engineering (CAE) has been becoming significant for designers.

The finite element method (FEM) [2] is often used to analyze electromagnetic apparatuses. Since a geometry is represented by a set of small finite elements in FEM, complex shapes can be represented easily. It also makes it easier to take into account the nonlinear properties of the material. Besides, it is possible to calculate physical quantities inside the electromagnetic apparatuses that cannot be obtained from experiments. Therefore, FEM is suitable for the advanced design of electromagnetic apparatuses. Although FEM is powerful and is widely used in the design process, it has its limitations. One of them is the accurate calculation of the eddy current losses at high frequencies. To achieve high accuracy, the domain in which the eddy currents flow must be divided into small finite elements to take the skin depth into account. However, this kind of subdivision results in a numerous number of elements and increases the computational cost of solving the equations.

There are three main approaches to this problem: first one is to introduce some approximations and solve Maxwell's equations analytically, the second one is to improve the solution methods to solve the finite element (FE) equations faster, and third is to generate a reduced order model (ROM) from the equations which is referred to as the model order

reduction (MOR). In the first approach, due to the approximations, we can obtain analytical expression of the losses [3, 4] but it is usually less accurate than FE solutions. In the second approach, there are a lot of studies on it, for example, parallelization techniques for the conjugate gradient solver [5, 6], multi-grid methods for electromagnetism [7, 8], and relaxation/acceleration factors for iterative methods [9, 10]. The third approach involves approximating the original equation with a low-dimensional model with minimal loss of information. This approach includes, for example, the Krylov subspace methods [11, 12, 13], the proper orthogonal decomposition (POD)-discrete empirical interpolation method (DEIM) and its variants [14, 15, 16], and, more recently, the methods using the deep learning [17]. In general, the Krylov subspace methods are suitable for linear problems, POD-DEIM for problems with nonlinear equations, and the deep learning for problems where the equations are unknown or the data have strong nonlinear correlations, respectively. For POD and other projection-based MORs, see survey paper [18].

In this study, we focus on methods based on the Krylov subspace methods. Although the methods have been applied to electromagnetic field analysis [19, 20, 11, 21], there is still not enough knowledge on the application to the homogenization or Darwin model of Maxwell's equations. If we can obtain the ROMs for these systems, we can consider their application to the design optimization and coupling with external circuits, which are difficult tasks for the conventional FEM.

1.2 Contribution of the study

1.2.1 Cauer circuit via Lanczos process (CVL)

Around 1990, the asymptotic waveform evaluation (AWE) was proposed by Pillage et al. [22] as a MOR based on the Padé approximation via the explicit moment-matching in the large-scale linear equations. AWE is a breakthrough method that can replace large linear equations with low-dimensional ROMs, and thus significantly reduce computational costs with small losses. However, it is numerically unstable due to the fact that increasing the order of moments makes the Hankel matrix near-singular [23]. In 1994, Gallivan et al. [24] reported on AWE, linking moments to the Lanczos process which is one of the Krylov subspace methods. Independently, in 1995, Feldmann [25] proposed the Pade approximation via Lanczos process (PVL), which overcame the computational instability of AWE. PVL is a method of the Padé approximation of a given transfer function that does not explicitly compute moments, but relates the Lanczos process to moments, the so-called Padé connection. Stable methods for multi-input-multi-output (MIMO) [26] and symmetric problems [27] have also been proposed, respectively. Also, passivity-preserving MOR [28, 29] methods were proposed since passivity is not guaranteed by the ROMs

generated by AWE and PVL. For more information on its application to the second order system and nonlinear problems and history, see the survey paper by Freund [30] and Bai [31] and the Ph.D thesis of Grimme [32].

In the field of computational electromagnetism, MOR based on the Krylov subspace methods (e.g., PVL) has also been applied to the finite element equation [11, 12, 13]. On the other hand, a new model reduction method, referred to as Cauer network method (CLN), was proposed by Kameari et al. [33] in 2017 to derive the Cauer circuit from Maxwell's equations in differential form based on phenomenological observations on eddy currents. Since the Cauer circuit has physical meanings, the nonlinear property due to the core saturation [21] and hysteresis [34, 35] can be introduced into the circuit. The method was soon to be extended to unbounded problems [36], introduction of multiple expansion points [37] nonlinear problems [38], MIMO systems [39], and translation mover problems [40], and is currently being actively studied. Matsuo argues that the CLN method is based on the Lanczos process by reformulating the CLN method in matrix form [41], but the relationship with the existing Krylov subspace methods such as PVL is not so clear.

Therefore, we have studied the relation between PVL and CLN and showed that CLN is equivalent to Padé approximation via the Lanczos process for self-adjoint operators in linear space and associate with SyPVL [27]. We also proposed **Cauer circuit via Lanczos process (CVL)** that can obtain Stieltjes continued fraction as Padé approximation by changing the normalization condition of PVL. Since PVL and CVL are based on the common principle, the accuracy of the model are the same, but the Cauer circuit obtained by CVL can be interpreted as the RL or RC equivalent circuit, which is compatible in circuit analysis. This is also consistent with the physical intuition that electromagnetic fields can be represented in RL or RC circuit.

Furthermore, we propose a new algorithm **CVL squared (CVLs)** that does not require matrix transposition based on a matrix polynomial representation. This algorithm is required for the generation of ROM of the Darwin model of Maxwell's equations.

1.2.2 Application to homogenization of Maxwell's equations

With the recent development of power electronic circuits, electromagnetic apparatuses are being driven at higher frequencies. Since the high frequency components of the power supply induce the eddy currents due to the skin and proximity effects, it is important to evaluate the eddy current losses in electromagnetic apparatuses such as motors [42, 43], inductors [44], induction heating appliance [45] and wireless power transfer devices [46]. Despite its great importance, as already mentioned, the use of FEM increases the computational cost. In particular, it is virtually impossible to apply FEM to the microstructure materials such as the Litz wire, which consists of very fine wires.

There are two analytical approaches to this problem. The first approach is by Dowell et al. [47, 48, 49], which replaces cylindrical conductors with rectangular conductors of equal area, approximates the windings with foils, and solves the 1D model analytically. The second approach is by Ferreira [50, 51], which uses Bessel function solutions for isolated conductors placed in a uniform magnetic field. Both methods cannot accurately take into account the effect of the reaction field created by the eddy currents caused by the proximity effect. In fact, it has been pointed out that the former and the latter methods underestimate and overestimate [52]. The former approach is modified by Nan et al. [3] to improve the accuracy using FEM, and by Wojda et al. [4] to compute the AC resistance of the Litz wires. For the latter method, in 2016, Igarashi [53] proposed a semi-analytical method using Ollendorff formula [54] to take into account the reaction field created by eddy currents.

Although the analytical approaches are straightforward to calculate the losses, the solution may not be accurate depending on the coil geometry. In contrast, there is a numerical approach using homogenization [55]. In 2003, Podoltsev et al. [56] proposed a method to obtain the complex permeability of multi-turn winding from a unit cell. Gyselinck et al. [57] generalized this approach for an arbitrary packing and conductors of arbitrary cross-sections. Although the method is for frequency domain, a formulation for time domain analysis has been proposed in [58, 59, 60, 61, 62]. This approach seems to be useful, but it is necessary to perform FE analysis for different frequencies and volume fraction. To solve this problem, Sato [63] proposed a method to obtain the complex permeability by applying PVL to FE equations of a unit cell. However, this method is based on Ollendorff's formula, and it is difficult to obtain the diamagnetic constant N for conductors of arbitrary cross-sections.

We have studied a new method to obtain the complex permeability in the form of the continued fraction as a function of frequency by applying CVL to the FE equation of a unit cell. Conventionally, FE analysis had to be performed many times at different frequencies, but using the proposed method, one can obtain the frequency characteristics with a smaller number of analyses.

The homogenization method can significantly reduce the number of unknowns, but it would be computationally advantageous if it were possible to reduce the number of unknowns further. Thus, we have developed a new method to reduce the number of unknowns by applying CVL to homogenization of Maxwell's equations. Furthermore, we show that obtained ROM can be considered as an equivalent circuit when the complex permeability can be expressed as a continued fraction. It can be shown that this equivalent circuit has an explicit expression of phenomenon such as the skin and proximity effects.

Another application of CVL is to improve the accuracy of Dowell's equation. We pro-

posed a new method simply to calculate the eddy current loss without degradation of accuracy in the high frequency range using complex permeability obtained by CVL. The created ROM is represented as an equivalent RL circuit, which enables circuit analysis using a circuit simulator.

1.2.3 Application to Darwin model of Maxwell's equations

At higher frequencies, not only the eddy currents but also the parasitic capacitance would affect the behavior. However, the effect of displacement current cannot be taken into account in the magneto-quasi-static (MQS) approximation of Maxwell's equations because they ignore the displacement current. There is a formulation called Darwin or electromagnetic-quasi-static (EMQS) approximation [64, 65, 66] which takes the effect of displacement current into account. The FE equation of the Darwin model of Maxwell's equations is asymmetric when using $A-\phi$ method [67, 68]. In the literature, the iterative method for the asymmetric matrix such as GMRES [69] and BiCGstab [70] is employed to solve the FE equations. Although it is possible to symmetrize it by imposing a Coulomb gauge [71, 72, 73], there are concerns about the deterioration of the convergence of the ICCG method [74].

Therefore, we propose a new formulation for generating ROM by applying CVLs to the Darwin model of Maxwell's equations. In the method, we can obtain ROM by solving the Poisson equations inside and outside the conductor region and gauge-free static Maxwell's equations during the iteration. Thus, we can use the ICCG solver to obtain ROM.

1.3 Dissertation outline

In Chapter 2, we describe Maxwell's equations and brief formulation of FEM. In Chapter 3, we discuss the Lanczos process, one of the Krylov subspace methods. We also describe a formulation of PVL. Then, we explain CLN and propose CVL. Based on the similarity with the conjugate gradient squared (CGS) algorithm [75] and CVL, we propose CVLs that do not require the computation of matrix transposition. In the second half of Chapter 3, we describe an application of the MQS approximation of Maxwell's equations and show that the Cauer circuit is obtained as an equivalent circuit. In Chapter 4, we first describe the theory of the homogenization method. Next, we propose a method for obtaining equivalent circuits by applying CVL to the homogenization of Maxwell's equations. Besides, we apply CVL to the equations used in the homogenization method to obtain the complex permeability in the form of a continued fractional function. At the end of Chapter 4, we try to improve the estimation accuracy of the eddy current losses in the slot winding by applying the complex permeability to Dowell's equation. In Chapter 5, we propose new

method to obtain ROM of the Darwin model of Maxwell's equations. The fact that the electric field obtained in this case does not have a correct distribution is discussed from the viewpoint of gauge invariance, and a method for improvement is described. It is shown that this method can be used to quickly calculate the characteristics near the resonant point considering the eddy currents. In Chapter 6, we summarize this thesis and describe the open problems.

Chapter 2.

Finite element analysis of Maxwell's equations

2.1 Maxwell's equations

The variables that appear in Maxwell's equations include the five vectors and one scalar listed in Table 2.1. These are functions of the spatial coordinates x, y, z and time t,

Table2.1: Physical quantities in Maxwell's equations

electric field intensity	$\boldsymbol{E}$	V/m
magnetic field intensity	$\boldsymbol{H}$	H/m
electric flux density	$\boldsymbol{D}$	C/m^2
magnetic flux density	$\boldsymbol{B}$	T
electric current density	$\boldsymbol{J}$	A/m^2
electric charge density	ρ	C/m^3

respectively. Maxwell's equations in differential form can be written in the following four equations [2].

$$\nabla \times \boldsymbol{H} = \boldsymbol{J} + \frac{\partial \boldsymbol{D}}{\partial t} \quad \text{(Ampère's law)}, \tag{2.1}$$

$$\nabla \times \boldsymbol{E} = -\frac{\partial \boldsymbol{B}}{\partial t} \quad \text{(Faraday's law)}, \tag{2.2}$$

$$\nabla \cdot \boldsymbol{B} = 0, \tag{2.3}$$

$$\nabla \cdot \boldsymbol{D} = \rho. \tag{2.4}$$

In addition to these relations, the constitutive equations

$$\boldsymbol{D} = \epsilon \boldsymbol{E}, \tag{2.5}$$

$$\boldsymbol{B} = \mu \boldsymbol{H}, \tag{2.6}$$

$$\boldsymbol{J} = \sigma \boldsymbol{E}, \tag{2.7}$$

are added where ϵ, μ, σ are dielectric permittivity, magnetic permeability and conductivity, respectively, which describe the macroscopic properties of the medium.

Besides Maxwell's equations, the current continuity equation is often used to analyze electromagnetic apparatus. On taking divergences of (2.1), we obtain

$$\nabla \cdot \boldsymbol{J} + \frac{\partial}{\partial t} \nabla \cdot \boldsymbol{D} = 0. \tag{2.8}$$

Combining with (2.4), we obtain the current continuity equation

$$\nabla \cdot \boldsymbol{J} + \frac{\partial \rho}{\partial t} = 0. \tag{2.9}$$

Although this equation is covered by (2.1), (2.4), it is more suitable for dealing with situations where materials with very high conductivity are excited by external circuits.

2.2 Complex phasor notation

In some problems, it is assumed that the variables of the system change sinusoidally. In such cases, it is convenient to represent the variables in complex phasor form. That is, a sinusoidally time-varying variable is represented by a complex number, e.g. $\boldsymbol{E}_{\mathrm{p}} = \boldsymbol{E}_{\mathrm{r}} + \mathrm{j}\boldsymbol{E}_{\mathrm{i}}$ in case of an electric field, where j denotes the imaginary unit. The corresponding time-varying variable is restored by taking the real part of $\boldsymbol{E}_{\mathrm{p}} \exp \mathrm{j}\omega$ where ω is the angular frequency. Using a phasor notation, the differential operator $\partial/\partial t$ can be simply replaced by an algebraic product of $\mathrm{j}\omega$. Hence, (2.1) and (2.2) are expressed in phasor notation as follows:

$$\nabla \times \boldsymbol{H} = \boldsymbol{J} + \mathrm{j}\omega \boldsymbol{D}, \tag{2.10}$$

$$\nabla \times \boldsymbol{E} = -\mathrm{j}\omega \boldsymbol{B}. \tag{2.11}$$

2.3 Boundary conditions

As with other differential equations, Maxwell's equations can only be solved if they are accompanied by appropriate boundary conditions at the boundaries of the domain under consideration, and by interface conditions where different materials join. If 1 and 2 represent two materials with different properties, then a set of rules at material interfaces is derived from Maxwell's equations in integral form as follows:

1. The tangential component of $\boldsymbol{E}$ is always continuous,

$$\boldsymbol{n} \times (\boldsymbol{E}_1 - \boldsymbol{E}_2) = \boldsymbol{0}. \tag{2.12}$$

2. The tangential component of $\boldsymbol{H}$ is discontinuous by an amount corresponding to any surface current $\boldsymbol{J}_{\mathrm{s}}$,

$$\boldsymbol{n} \times (\boldsymbol{H}_1 - \boldsymbol{H}_2) = \boldsymbol{J}_{\mathrm{s}}. \tag{2.13}$$

3. The normal component of $\boldsymbol{B}$ is always continuous,

$$\boldsymbol{n} \cdot (\boldsymbol{B}_1 - \boldsymbol{B}_2) = 0. \tag{2.14}$$

4. The normal component of $\boldsymbol{D}$ is discontinuous by an amount corresponding to any surface charge ρ_{s},

$$\boldsymbol{n} \cdot (\boldsymbol{D}_1 - \boldsymbol{D}_2) = \rho_{\mathrm{s}}. \tag{2.15}$$

Note that $\boldsymbol{n}$ is the unit normal to the interface of the materials from 1 to 2. The boundary conditions are given by extending the interface conditions. In other words, the interface conditions are assumed to be a fictitious material with infinite (or zero) magnetic permeability, permittivity, and conductivity. The choice of the virtual value of the fictitious material depends on the problem to be solved and must be determined appropriately.

For example, if we assume a perfect conductor of a fictitious material $\sigma = \infty$, no tangential component of the electric field can exist outside of the domain, and since there is no magnetic flux density outside, the boundary conditions become as follows:

$$\boldsymbol{n} \times \boldsymbol{E} = \boldsymbol{0}, \tag{2.16}$$
$$\boldsymbol{n} \times \boldsymbol{H} = \boldsymbol{J}_{\mathrm{s}}, \tag{2.17}$$
$$\boldsymbol{n} \cdot \boldsymbol{B} = 0, \tag{2.18}$$
$$\boldsymbol{n} \cdot \boldsymbol{D} = \rho_{\mathrm{s}}. \tag{2.19}$$

In this case, the electric field enters perpendicular to the boundary and the magnetic flux density is parallel to the boundary. This is called the perfect conductor boundary condition (PEC) and is sometimes used in combination with (2.9) to excite conductors.

For the boundary condition for the magnetic field, we often assume the following two boundary conditions

$$\boldsymbol{n} \cdot \boldsymbol{B} = 0, \tag{2.20}$$
$$\boldsymbol{n} \times \boldsymbol{H} = \boldsymbol{0} \tag{2.21}$$

which can be derived by considering a fictitious material $\mu = 0, \infty$, respectively. The former condition represents that the magnetic flux is closed in the domain and does not go out of the domain, whereas the latter condition represents that the magnetic field is perpendicular to the boundary.

In general, the boundary conditions are classified into three boundary conditions: Dirichlet Γ_{D}, Neumann Γ_{N}, Cauchy Γ_{C}. For example, PEC and (2.20) are Dirichlet conditions,

and (2.21) is homogeneous Neumann condition. Let u is the solution of the differential equations, it satisfies

$$u = u_0 \quad \text{on } \Gamma_{\mathrm{D}}, \tag{2.22}$$

$$\frac{\partial u}{\partial n} = \nabla u \cdot \boldsymbol{n} = v_0 \quad \text{on } \Gamma_{\mathrm{N}}, \tag{2.23}$$

$$\nabla u \cdot \boldsymbol{n} + \alpha u = v_0 \quad \text{on } \Gamma_{\mathrm{C}} \tag{2.24}$$

The approximating functions U satisfy the Dirichlet condition by setting $U = u$ in the equations to be solved. The homogeneous Neumann conditions

$$\frac{\partial u}{\partial n} = \nabla u \cdot \boldsymbol{n} = 0 \tag{2.25}$$

are satisfied approximately without any restrictions on the functions U. It is because the conditions are satisfied simply by neglecting the boundary integral term of the variational form of the differential equations. The Dirichlet and homogeneous Neumann conditions are also termed 'essential' and 'natural' boundary conditions because the former is enforced by restricting the functions U whereas the latter is realized by the variational form implicitly.

2.4 Three quasi-static approximations of Maxwell's equations

Instead of solving the full set of Maxwell's equations in numerical computations, we often solve Maxwell's equations in the low-frequency approximation. The electro-quasi-static (EQS), magneto-quasi-static (MQS), and electromagnetic-quasi-static (EMQS) approximations are known as the approximations [64, 65, 66]. The third approximation is also known as the Darwin model. The approximations are valid under certain restrictions on the material property and the size of the domain of the problems [76, 77]. We discuss here a very simple and locally limited case. The first restriction is characterized by the characteristic time constant $\tau = \omega^{-1}$ and transit time τ_{em} which is given as

$$\tau_{\mathrm{em}} = \frac{l}{c} \tag{2.26}$$

where l, c are the characteristic length of the problem and speed of light respectively. For the quasi-static approximations, it is supposed that the characteristic time constant is much greater than the transit time,

$$\left(\frac{\tau_{\mathrm{em}}}{\tau}\right)^2 \ll 1, \tag{2.27}$$

i.e. the wave propagation is no longer considered. And the second restrictions are characterized by the time constants of dielectric relaxation τ_{e} and magnetic diffusion τ_{m} which

are defined as

$$\tau_{\mathrm{e}} = \frac{\epsilon}{\sigma}, \tag{2.28}$$

$$\tau_{\mathrm{m}} = \mu\sigma l^2. \tag{2.29}$$

2.4.1 EQS approximation

For the EQS approximation, it is supposed that

$$\tau_{\mathrm{m}} \ll \tau. \tag{2.30}$$

It means that magnetic induction $\partial \boldsymbol{B}/\partial t$ in Faraday's law (2.2) can be neglected in Maxwell's equations. Therefore, we obtain

$$\nabla \times \boldsymbol{H} = \boldsymbol{J} + \frac{\partial \boldsymbol{D}}{\partial t}, \tag{2.31}$$

$$\nabla \times \boldsymbol{E} = \boldsymbol{0}, \tag{2.32}$$

$$\nabla \cdot \boldsymbol{B} = 0, \tag{2.33}$$

$$\nabla \cdot \boldsymbol{D} = \rho. \tag{2.34}$$

The electric field is obtained by solving (2.32), (2.34). Ampère's law (2.31) is no longer needed to obtain the electric field, and the magnetic field can be obtained from (2.31) by post-processing.

2.4.2 MQS approximation

The MQS approximation is widely used in the eddy current analysis of the low-frequency electromagnetic apparatuses because the displacement current can usually be ignored in the good conductor which has high conductivity. This situation represent the characteristic time constant is much larger than the relaxation,

$$\tau_{\mathrm{e}} \ll \tau. \tag{2.35}$$

It means that $\partial \boldsymbol{D}/\partial t$ in Ampère's law (2.1) can be neglected in Maxwell's equations. Thus, we obtain

$$\nabla \times \boldsymbol{H} = \boldsymbol{J}, \tag{2.36}$$

$$\nabla \times \boldsymbol{E} = -\frac{\partial \boldsymbol{B}}{\partial t}, \tag{2.37}$$

$$\nabla \cdot \boldsymbol{B} = 0, \tag{2.38}$$

$$\nabla \cdot \boldsymbol{D} = \rho. \tag{2.39}$$

Just like the EQS approximation, the magnetic field can be obtained by solving (2.36), (2.38), and the electric field can be obtained from (2.37) in post-processing.

2.4.3 EMQS approximation (Darwin model)

The EMQS approximation encompasses both the EQS and MQS approximations and is valid if the following holds

$$\tau_{\mathrm{e}}, \tau_{\mathrm{m}} \sim \tau. \tag{2.40}$$

In the EMQS approximation of Maxwell's equations, not all of $\partial \boldsymbol{D}/\partial t$ but the rotational part is neglected to consider the capacitive and inductive effects in the quasi-static approximation. In general, the vector fields $\boldsymbol{E}$ can be decomposed into two parts (*Helmholtz decomposition, Hodge decomposition*) [78]: divergence-free (transverse) $\boldsymbol{E}_{\mathrm{T}}$ and irrotational (longitudinal) $\boldsymbol{E}_{\mathrm{L}}$ which are defined as

$$\nabla \cdot \boldsymbol{E}_{\mathrm{T}} = 0, \tag{2.41}$$
$$\nabla \times \boldsymbol{E}_{\mathrm{L}} = \boldsymbol{0} \tag{2.42}$$

where $\boldsymbol{E} = \boldsymbol{E}_{\mathrm{T}} + \boldsymbol{E}_{\mathrm{L}}$. Neglecting the transversal component of the displacement currents, we obtain

$$\nabla \times \boldsymbol{H} = \boldsymbol{J} + \frac{\partial \boldsymbol{D}_{\mathrm{L}}}{\partial t}, \tag{2.43}$$
$$\nabla \times \boldsymbol{E} = -\frac{\partial \boldsymbol{B}}{\partial t}, \tag{2.44}$$
$$\nabla \cdot \boldsymbol{B} = 0, \tag{2.45}$$
$$\nabla \cdot \boldsymbol{D}_{\mathrm{L}} = \rho. \tag{2.46}$$

2.5 Potential form of Maxwell's equations

It is well known that Maxwell's equations can be expressed in terms of magnetic vector potentials (MVP) and electric scalar potentials (ESP). Also, the term "vector potential" or "scalar potential" is sometimes used. We start by describing the electric and magnetic fields in terms of potentials,

$$\boldsymbol{B} = \nabla \times \boldsymbol{A}, \tag{2.47}$$
$$\boldsymbol{E} = -\frac{\partial \boldsymbol{A}}{\partial t} - \nabla \phi \tag{2.48}$$

which can be derived from (2.3), (2.2). Substituting these relations into (2.1), (2.4) result in

$$\nabla \times \nu \nabla \times \boldsymbol{A} = \sigma \left(-\frac{\partial \boldsymbol{A}}{\partial t} - \nabla \phi \right) + \frac{\partial}{\partial t} \epsilon \left(-\frac{\partial \boldsymbol{A}}{\partial t} - \nabla \phi \right), \tag{2.49}$$
$$\nabla \cdot \epsilon \left(-\frac{\partial \boldsymbol{A}}{\partial t} - \nabla \phi \right) = \rho \tag{2.50}$$

where ν is the magnetic resistivity defined by the reciprocal of the magnetic permeability. Similarly, we can derive the potential forms of the quasi-static approximations of Maxwell's equations.

2.5.1 EQS approximation

From (2.32), the electric field can be written only by the scalar potential ϕ as follows:

$$\boldsymbol{E} = \nabla\phi. \tag{2.51}$$

Taking the divergences of the both side of (2.31) reads the governing equations of the EQS approximation of Maxwell's equations as follows:

$$\nabla \cdot \sigma\nabla\phi + \frac{\partial}{\partial t}\nabla \cdot \epsilon\nabla\phi = 0. \tag{2.52}$$

2.5.2 MQS approximation

From (2.36), the potential form of the MQS approximation can be written as

$$\nabla \times \nu\nabla \times \boldsymbol{A} = \boldsymbol{J}_0 + \sigma\left(-\frac{\partial \boldsymbol{A}}{\partial t} - \nabla\phi\right) \tag{2.53}$$

where ν is the magnetic resistivity defined by the reciprocal of the permeability μ^{-1}. In this equations, we assume that the source current density $\boldsymbol{J}_0$ which satisfies $\nabla\boldsymbol{J}_0 = 0$ is given in the domain. Note that the scalar potential ϕ is only defined in the conductor domain $\sigma > 0$ because there is no need to consider the electric field outside the conductor. Equation (2.53) has more unknowns than the number of equations, so they cannot be solved alone. In terms of numerical computation, it is often coupled with a dependent equation obtained by taking the divergences of both sides. Hence, we obtain

$$\nabla \cdot \sigma\left(-\frac{\partial \boldsymbol{A}}{\partial t} - \nabla\phi\right) = 0 \tag{2.54}$$

which is equal to the current continuity. Since these equations are dependent, the coupled equation has multiple solutions for the vector and scalar potentials whereas the electric and magnetic fields are determined uniquely. It is well known that the multiple solutions are converted to each other by a gauge transformation.

In the above formulation, both vector and scalar potentials are used despite the fact that the electric field can only be represented by the vector potential. Such formulation is referred to as the A-ϕ method whereas the method that only use the vector potential is referred to the A method. A method can be derived simply by eliminating ϕ from the governing equations. The equation of the A method is given as

$$\nabla \times \nu\nabla \times \boldsymbol{A} + \sigma\frac{\partial \boldsymbol{A}}{\partial t} = \boldsymbol{J}_0. \tag{2.55}$$

Since the scalar potential is not appeared in the governing equation, the number of the unknowns is less than that of the A-ϕ method . However, it has been also pointed out that the elimination of the scalar potential can deteriorate the convergence of ICCG of the FE equations [74], so the A-ϕ method is usually used in the eddy current analysis.

2.5.3 EMQS approximation (Darwin model)

By a similar procedure, potential forms of the EMQS approximation of Maxwell's equations are obtained as follows:

$$\nabla \times \nu \nabla \times \boldsymbol{A} = \sigma\left(-\frac{\partial \boldsymbol{A}}{\partial t} - \nabla\phi\right) - \frac{\partial}{\partial t}\epsilon\nabla\phi, \tag{2.56}$$

$$0 = \nabla \cdot \sigma\left(-\frac{\partial \boldsymbol{A}}{\partial t} - \nabla\phi\right) - \nabla \cdot \frac{\partial}{\partial t}\epsilon\nabla\phi. \tag{2.57}$$

In contrast to the MQS approximation, the EMQS approximation of Maxwell's equation does not have gauge invariance [79], so it is necessary to determine a physical solution from multiple solutions. This is caused by the redundancy of the gradient component of the vector potential. In fact, in the EMQS approximation, we ignore the displacement current due to the vector potential $\boldsymbol{A}_{\mathrm{T}} + \boldsymbol{A}_{\mathrm{L}}$ in (2.1) although it has also the longitudinal component. Therefore, we have to eliminate the longitudinal component of the vector potential $\boldsymbol{A}_{\mathrm{L}} = \nabla\chi$ where χ is the arbitrary scalar potential. To do this, the Coulomb gauge can be used to fix $\boldsymbol{A}_{\mathrm{L}} = \boldsymbol{0}$. The alternative way is to use Gauss's law explicitly, which can be found in [80].

2.6 Weak formulation

The mathematical background of FEM depends on the theory of the partial differential equations which uses the Sobolev spaces and weak formulation [81]. However, since a rigorous treatment of mathematical theory requires some prior knowledge, we only describe here the procedure for deriving weak formulation from Maxwell's equations, especially from the MQS approximation of Maxwell's equations.

Let Ω the open bounded subset in $\mathbb{R}^3$. It is assumed that the boundary $\Gamma = \partial\Omega$ is composed of non-overlapping boundaries $\Gamma_{\mathrm{D}}, \Gamma_{\mathrm{N}}$ which are the Dirichlet and homogeneous Neumann boundaries. Let $\Omega_{\mathrm{c}} \subset \Omega$ be a conductor domain which has the positive conductivity. In $\Omega_{\mathrm{e}} = \Omega \setminus \overline{\Omega}_{\mathrm{c}}$, we assume the conductivity is zero. On the boundaries, it holds that

$$\boldsymbol{n} \times \boldsymbol{H} = \boldsymbol{0} \quad \text{on } \Gamma_{\mathrm{N}}, \tag{2.58}$$

$$\boldsymbol{n} \cdot \boldsymbol{B} = 0 \quad \text{on } \Gamma_{\mathrm{D}}. \tag{2.59}$$

We first derive the variational form of the MQS approximation of Maxwell's equations.

To do this, we multiply both sides of (2.53), (2.54) by the vector and scalar test functions $\boldsymbol{w}, w$, and integrate it over the whole domain.

$$\int_\Omega \boldsymbol{w} \cdot \nabla \times \nu \nabla \times \boldsymbol{A} d\Omega + \int_{\Omega_c} \boldsymbol{w} \cdot \sigma \left(\frac{\partial \boldsymbol{A}}{\partial t} + \nabla \phi \right) d\Omega = \int_\Omega \boldsymbol{w} \cdot \boldsymbol{J}_0 d\Omega, \tag{2.60}$$

$$\int_{\Omega_c} w \nabla \cdot \sigma \left(\frac{\partial \boldsymbol{A}}{\partial t} + \nabla \phi \right) d\Omega = 0. \tag{2.61}$$

Integrating by parts results in

$$\int_\Omega \nabla \times \boldsymbol{w} \cdot \nu \nabla \times \boldsymbol{A} d\Omega - \int_{\Gamma_N} \boldsymbol{w} \cdot (\boldsymbol{H} \times \boldsymbol{n}) dS + \int_{\Omega_c} \boldsymbol{w} \cdot \sigma \left(\frac{\partial \boldsymbol{A}}{\partial t} + \nabla \phi \right) d\Omega = \int_\Omega \boldsymbol{w} \cdot \boldsymbol{J}_0 d\Omega, \tag{2.62}$$

$$\int_{\Omega_c} \nabla w \cdot \sigma \left(\frac{\partial \boldsymbol{A}}{\partial t} + \nabla \phi \right) d\Omega - \int_{\partial \Omega_c} w (\boldsymbol{E} \cdot \boldsymbol{n}) dS = 0. \tag{2.63}$$

Note that we assume that the test functions $\boldsymbol{w}, w$ vanish on the Dirichlet boundary Γ_D. Therefore, the boundary integral term vanishes on Γ_D. In the first equation, the boundary integral term vanishes due to the Neumann boundary condition, and in the second equation, it vanishes because of the condition that the eddy current does not go outside the conductor domain. Therefore, we obtain the weak formulation of the MQS approximation of Maxwell's equation as follows:

$$\int_\Omega \nabla \times \boldsymbol{w} \cdot \nu \nabla \times \boldsymbol{A} d\Omega + \int_{\Omega_c} \boldsymbol{w} \cdot \sigma \left(\frac{\partial \boldsymbol{A}}{\partial t} + \nabla \phi \right) d\Omega = \int_\Omega \boldsymbol{w} \cdot \boldsymbol{J}_0 d\Omega, \tag{2.64}$$

$$\int_{\Omega_c} \nabla w \cdot \sigma \left(\frac{\partial \boldsymbol{A}}{\partial t} + \nabla \phi \right) d\Omega = 0. \tag{2.65}$$

The solutions of the weak formulation lies on the Sobolev subspaces, and is called "weak solutions" of the original equations.

2.7 Galerkin finite element discretization

To obtain the weak solution numerically, we have to discretize the equation. To do this, the domain Ω is partitioned into finite number of sub-domains which are called finite elements. Then, the vector and scalar potentials are discretized by the edge elements [82, 83] and node interpolation function defined on the finite elements:

$$\boldsymbol{A} \approx \sum_{i \in E(\Omega)} a_i \boldsymbol{w}_i^e, \tag{2.66}$$

$$\phi \approx \sum_{i \in V(\Omega_c)} \phi_i w_i^n \tag{2.67}$$

where $E(\Omega), V(\Omega)$ represent the set of indices of the edge and node in Ω. Note that the a_i is defined by the line integral of the vector potential along the i-th edge, and ϕ_i is the value of the scalar potential on the i-th node. In the Galerkin finite element discretization, one can obtain finite element equations by replacing the test function spaces with the finite dimensional subspaces $\mathrm{span}\{\boldsymbol{w}_1^e, \ldots, \boldsymbol{w}_{N_e}^e\}$, $\mathrm{span}\{w_1^n, \ldots, w_{N_n}^n\}$. Therefore, we obtain the finite element equations as follows:

$$\sum_{j\in E(\Omega)} a_j \int_\Omega \nabla\times\boldsymbol{w}_i^e\cdot\nu\nabla\times\boldsymbol{w}_j^e d\Omega + \sum_{j\in E(\Omega)} \frac{da_j}{dt}\int_{\Omega_c} \boldsymbol{w}_i^e\cdot\sigma\boldsymbol{w}_j^e d\Omega + \sum_{k\in V(\Omega_c)} \phi_k \int_{\Omega_c} \boldsymbol{w}_i^e\cdot\sigma\cdot\nabla w_k^n d\Omega = \int_\Omega \boldsymbol{w}_i^e\cdot\boldsymbol{J}_0 d\Omega, \tag{2.68}$$

$$\sum_{j\in V(\Omega_c)} \frac{da_j}{dt}\int_{\Omega_c} \nabla w_i^n\cdot\sigma\boldsymbol{w}_j^n d\Omega + \sum_{k\in V(\Omega_c)} \phi_k\int_{\Omega_c}\nabla w_i^n\cdot\sigma\nabla w_k^n d\Omega = 0. \tag{2.69}$$

The equation can be written in the matrix form as follows:

$$\left(\begin{bmatrix} K & L \\ 0 & M\end{bmatrix} + \frac{d}{dt}\begin{bmatrix} N & 0 \\ L^\top & 0\end{bmatrix}\right)\begin{bmatrix}\boldsymbol{a}\\ \boldsymbol{\phi}\end{bmatrix} = \begin{bmatrix}\boldsymbol{b}\\ 0\end{bmatrix} \tag{2.70}$$

where

$$K = \left[k_{ij}\right], \quad k_{ij} = \int_\Omega \nabla\times\boldsymbol{w}_i^e\cdot\nu\nabla\times\boldsymbol{w}_j^e d\Omega, \tag{2.71}$$

$$N = \left[n_{ij}\right], \quad n_{ij} = \int_{\Omega_c} \boldsymbol{w}_i^e\cdot\sigma\boldsymbol{w}_j^e d\Omega, \tag{2.72}$$

$$L = \left[l_{ik}\right], \quad l_{ik} = \int_{\Omega_c} \boldsymbol{w}_i^e\cdot\sigma\cdot\nabla w_k^n d\Omega, \tag{2.73}$$

$$M = \left[m_{kl}\right], \quad m_{kl} = \int_{\Omega_c} \nabla w_i^n\cdot\sigma\nabla w_k^n d\Omega, \tag{2.74}$$

$$\boldsymbol{b} = \left[b_i\right], \quad b_i = \int_\Omega \boldsymbol{w}_i^e\cdot\boldsymbol{J}_0 d\Omega. \tag{2.75}$$

Using the finite-difference method, we can obtain the equation which can be used in the step-by-step analysis,

$$\left(\begin{bmatrix}0 & 0\\ 0 & \Delta t M\end{bmatrix} + \begin{bmatrix}K & L\\ L^\top & 0\end{bmatrix} + \begin{bmatrix}\frac{1}{\Delta t}N & 0\\ 0 & 0\end{bmatrix}\right)\begin{bmatrix}\boldsymbol{a}^n\\ \boldsymbol{\phi}^n\end{bmatrix} = \begin{bmatrix}\boldsymbol{b}^n\\ 0\end{bmatrix} + \begin{bmatrix}\frac{1}{\Delta t}N & 0\\ L^\top & 0\end{bmatrix}\begin{bmatrix}\boldsymbol{a}^{n-1}\\ \boldsymbol{\phi}^{n-1}\end{bmatrix} \tag{2.76}$$

Note that the second equation is multiplied by Δt to make the matrix symmetric. Due to the nature of the edge elements, the coefficient matrix K is singular, but it can be solved by the iterative methods such as the ICCG method. The resultant vector potential has an indefinite gradient component whereas the resultant magnetic field is determined

uniquely. Although we can make the matrix non-singular by imposing gauge constraints such as the Coulomb gauge and tree-cotree gauge [84], it has been pointed out that we can solve the equation faster when we do not impose the gauge constraint [85].

Thanks to the local nature of the edge elements and the nodal interpolation function, the resulting finite element matrix is sparse. Therefore, it is possible to solve the problem even if the dimensions of the problem are large.

2.8 Treatment of Dirichlet boundary conditions

The Dirichlet boundary conditions have not yet been applied to the FE equations derived above. Therefore, to solve the equations, the unknowns on the Dirichlet boundary must be enforced according to the Dirichlet conditions. We need to change the coefficient matrices to preserve the symmetry of the equation, and we will briefly discuss it here.

On the Dirichlet boundary, it holds that

$$\boldsymbol{E} \times \boldsymbol{n} = \boldsymbol{0} \quad \text{on } \Gamma_{\mathrm{D}}, \tag{2.77}$$
$$\boldsymbol{B} \cdot \boldsymbol{n} = 0 \quad \text{on } \Gamma_{\mathrm{D}}. \tag{2.78}$$

In potential form, they are the equivalent of the following conditions:

$$\left(\frac{\partial \boldsymbol{A}}{\partial t} + \nabla\phi\right) \times \boldsymbol{n} = \boldsymbol{0}, \tag{2.79}$$
$$(\nabla \times \boldsymbol{A}) \cdot \boldsymbol{n} = 0. \tag{2.80}$$

One way to achieve these are

$$\boldsymbol{A} = 0 \quad \text{on } \Gamma_{\mathrm{D}}, \tag{2.81}$$
$$\phi = \text{const.} \quad \text{on } \Gamma_{\mathrm{D}}. \tag{2.82}$$

Let us consider the situation where we have to make the i-th unknown $x_i = x_0$ of equation $K\boldsymbol{x} = \boldsymbol{b}$. To do this, the non-diagonal term in the i-th row must be zero and the diagonal term must be 1. The i-th component of the left hand side is fixed at x_0. Since this deformation makes the coefficient matrix asymmetric, it is necessary to move the i-th column to the right-hand side to maintain symmetry. This can be expressed in the

following equation.

$$
\begin{aligned}
K = \begin{bmatrix} & & k_{1i} & & \\ & & \vdots & & \\ k_{i1} & \cdots & k_{ii} & \cdots & k_{iN} \\ & & \vdots & & \\ & & k_{Ni} & & \end{bmatrix} &\rightarrow \begin{bmatrix} & & k_{1i} & & & & \\ & & \vdots & & & & \\ & & k_{i-1,i} & & & & \\ 0 & \cdots & 0 \;\; 1 \;\; 0 & & \cdots & & 0 \\ & & k_{i+1,i} & & & & \\ & & \vdots & & & & \\ & & k_{Ni} & & & & \end{bmatrix} \\
&\rightarrow \begin{bmatrix} & & 0 & & & & \\ & & \vdots & & & & \\ & & 0 & & & & \\ 0 & \cdots & 0 \;\; 1 \;\; 0 & & \cdots & & 0 \\ & & 0 & & & & \\ & & \vdots & & & & \\ & & 0 & & & & \end{bmatrix}
\end{aligned}
\tag{2.83}
$$

$$
\begin{aligned}
\boldsymbol{b} = \begin{bmatrix} b_1 \\ \vdots \\ b_{i-1} \\ b_i \\ b_{i+1} \\ \vdots \\ b_N \end{bmatrix} &\rightarrow \begin{bmatrix} b_1 \\ \vdots \\ b_{i-1} \\ x_0 \\ b_{i+1} \\ \vdots \\ b_N \end{bmatrix} \\
&\rightarrow \begin{bmatrix} b_1 \\ \vdots \\ b_{i-1} \\ x_0 \\ b_{i+1} \\ \vdots \\ b_N \end{bmatrix} - \begin{bmatrix} k_{1i} \\ \vdots \\ k_{i-1,i} \\ 0 \\ k_{i+1,i} \\ \vdots \\ k_{N,i} \end{bmatrix} x_0
\end{aligned}
\tag{2.84}
$$

Thus, given all the Dirichlet conditions, it is possible to solve the equations by the iterative solvers for the symmetric matrices.

Chapter 3.

Cauer circuit via Lanczos algorithm

3.1 Krylov subspace methods

3.1.1 Krylov subspace

The problem of solving differential equations numerically usually results in the problem of solving large sparse matrices. Large-scale sparse matrices cannot be solved by the direct methods anymore, so the iterative methods are often used. Among them, the Krylov subspace methods such as the conjugate gradient (CG) method [86] are currently the most widely used. Given the matrix $A \in \mathbb{F}^{N\times N}$ and vector $\boldsymbol{v} \in \mathbb{F}^N$, the sequence of Krylov subspaces are defined by

$$\mathcal{K}_n(A, \boldsymbol{v}) = \mathrm{span}\{\boldsymbol{v}, A\boldsymbol{v}, A^2\boldsymbol{v}, \ldots, A^{n-1}\boldsymbol{v}\}, \quad \text{for } n = 1, 2, \ldots. \tag{3.1}$$

Since the Krylov subspaces can be generated only by the matrix-vector product, it is compatible with the numerical computation in terms of the memory resource and computational time.

The vectors

$$\boldsymbol{v}, A\boldsymbol{v}, A^2\boldsymbol{v}, \ldots \tag{3.2}$$

are called Krylov sequence generated by A and $\boldsymbol{v}$. There exists a uniquely defined integer $d = d(A, \boldsymbol{v})$ where $\boldsymbol{v}, A\boldsymbol{v}, \ldots, A^{d-1}\boldsymbol{v}$ are linearly independent and $\boldsymbol{v}, A\boldsymbol{v}, \ldots, A^d\boldsymbol{v}$ are linearly dependent. d is called the grade of $\boldsymbol{v}$ with respect to A. Since the $N + 1$ vectors $\boldsymbol{v}, A\boldsymbol{v}, \ldots, A^N\boldsymbol{v}$ must be linearly dependent, it always holds that $1 \le d \le N$. By construction, any vector $\boldsymbol{x} \in \mathcal{K}_n(A, \boldsymbol{v})$ can be written as

$$\begin{aligned} \boldsymbol{x} &= \sum_{j=0}^{n-1} \gamma_j A^j \boldsymbol{v} \\ &= P_{n-1}(A)\boldsymbol{v} \end{aligned} \tag{3.3}$$

where $P_{n-1}(\lambda) = \gamma_0 + \gamma_1\lambda + \cdots + \gamma_{n-1}\lambda^{n-1}$ is the polynomial degree of $n - 1$. This kind of notation will be used throughout this thesis.

3.1.2 Arnoldi and Lanczos algorithms

As well known as the classical power method, the Krylov sequence $\boldsymbol{v}, A\boldsymbol{v}, A^2\boldsymbol{v}, \dots$ rapidly converges to the dominant eigenvector of A. As a result, the vectors in the Krylov sequence become nearly dependent even though there is no numerical error. This leads to a loss of information. To avoid this, and to extract as much information as possible from the original linear system, we need to construct the orthogonal Krylov subspace bases. The Arnoldi algorithm is the basic algorithm to construct the orthogonal Krylov subspace bases which are related to the orthogonal transformations of the matrix A. The algorithm is equivalent to the Gram-Schmidt orthogonalization implemented in the Krylov sequence. Algorithm 1 shows the pseudo-code of the implementation of the Arnoldi algorithm.

Algorithm 1 Arnoldi algorithm, Gram-Schmidt implementation

Input: matrix $A \in \mathbb{F}^{N\times N}$, nonzero vector $\boldsymbol{v} \in \mathbb{F}^{N\times N}$, Let d be grade of $\boldsymbol{v}$ with respect to A.

Output: orthonormal vectors $\boldsymbol{v}_1, \dots, \boldsymbol{v}_d$ with $\mathrm{span}\{\boldsymbol{v}_1, \dots, \boldsymbol{v}_n\} = \mathcal{K}_n(A, \boldsymbol{v})$ for $n = 1, 2, \dots, d$.

Initialisation :$\boldsymbol{v}_1 = \boldsymbol{v}/|\boldsymbol{v}|$.

1: **for** $i = 1$ to d **do**
2: $\quad\hat{\boldsymbol{v}}_{i+1} = A\boldsymbol{v}_i - \sum_{j=1}^{i} h_{j,i}\boldsymbol{v}_j$ where $h_{j,i} = (A\boldsymbol{v}_i, \boldsymbol{v}_j)$,
3: $\quad h_{i+1,i} = |\hat{\boldsymbol{v}}_{i+1}|$,
4: $\quad$**if** $h_{i+1,i} \neq 0$ **then**
5: $\quad\quad\boldsymbol{v}_{i+1} = \hat{\boldsymbol{v}}_{i+1}/h_{i+1,i}$,
6: $\quad$**else**
7: $\quad\quad$**return** $\boldsymbol{v}_1, \dots, \boldsymbol{v}_i$.
8: $\quad$**end if**
9: **end for**
10: **return** $\boldsymbol{v}_1, \dots, \boldsymbol{v}_d$.

Next, we write the Arnoldi algorithm in matrix form. Let $V_n = [\boldsymbol{v}_1, \boldsymbol{v}_2, \dots, \boldsymbol{v}_n]$ be the matrix whose column is the orthonormal Krylov subspace bases, and

$$H_{n,n} = \begin{bmatrix} h_{1,1} & h_{1,2} & \cdots & h_{1,n} \\ h_{2,1} & h_{2,2} & \cdots & h_{2,n} \\ & \ddots & \ddots & \vdots \\ \Large 0 & & h_{n,n-1} & h_{n,n} \end{bmatrix} \tag{3.4}$$

be the $n\times n$ upper Hessenberg matrix whose entries are obtained by the Arnoldi algorithm.

After the n-th iteration, it holds that

$$AV_n = V_n H_{n,n} + h_{n,n+1}\boldsymbol{v}_{n+1}\boldsymbol{e}_n^\top, \quad n = 1, 2, \ldots \tag{3.5}$$

where $\boldsymbol{v}_{n+1}, \boldsymbol{e}_n$ are the $(n+1)$-th orthonormal vector and n-th column of the identity matrix I_n, $V_n^* V_n = I_n$ and $V_n^* \boldsymbol{v}_{n+1} = 0$. At the d-th iteration, we have $h_{d+1,d} = 0$ since d is the grade of $\boldsymbol{v}$ with respect to A i.e., $\boldsymbol{v}_1, \ldots, \boldsymbol{v}_{d+1}$ are linearly dependent.

As a special case, we suppose that A is the Hermitian matrix. Since $V_n^* A V_n = H_{n,n}$ must be Hermitian, it concluded that $H_{n,n}$ is tridiagonal matrix. The algorithm is known as the Hermitian Lanczos algorithm which is proposed by Lanczos [87]. In the Hermitian Lanczos algorithm, the orthogonal vector $\boldsymbol{v}_{i+1}$ can be represented only by $\boldsymbol{v}_i, \boldsymbol{v}_{i-1}$ because it holds $h_{j,i} = 0, j \leq i-2$. Therefore, the three-term recurrence relation is obtained as follows:

$$\hat{\boldsymbol{v}}_{n+1} = A\boldsymbol{v}_n - h_{n,n}\boldsymbol{v}_n - h_{n-1,n}\boldsymbol{v}_{n-1}, \quad n = 1, 2, \ldots. \tag{3.6}$$

The Hermitian Lanczos algorithm is shown in Algorithm 2. The matrix form becomes

$$AV_n = V_n T_n + \delta_{n+1}\boldsymbol{v}_{n+1}\boldsymbol{e}_n^\top, \quad n = 1, 2, \ldots \tag{3.7}$$

where

$$T_n = \begin{bmatrix} \gamma_1 & \delta_2 & & & 0 \\ \delta_2 & \gamma_2 & \delta_3 & & \\ & \ddots & \ddots & \ddots & \\ & & \delta_{n-1} & \gamma_{n-1} & \delta_n \\ 0 & & & \delta_n & \gamma_n \end{bmatrix}. \tag{3.8}$$

Note that the matrix T_n is a real symmetric tridiagonal matrix even if A is not a real matrix since it holds that $\delta_j = |\hat{\boldsymbol{v}}_j| > 0, j = 1, 2, \ldots, d$.

The three-term recurrence relation plays important role in CG and other iterative methods because we do not have to store all the bases to generate a new basis. It is a favorable characteristic when we deal with large sparse linear equations. It is also important that we can prove that the three-term recurrence relation holds for non-Hermitian and self-adjoint matrices.

3.1.3 Non-Hermitian Lanczos algorithm

Although it is not possible to apply the Lanczos algorithm to the non-Hermitian matrices, it is possible to relax and change the definition of orthogonality to establish a three-term recurrence relation. In the Hermitian Lanczos algorithm, What is important for $h_{j,i} = 0, j \leq i-2$ to hold is the symmetry of the inner product of the matrix A. Now look at the algebraic proof.

Algorithm 2 Hermitian Lanczos algorithm

Input: matrix $A \in \mathbb{F}^{N\times N}$, nonzero vector $\boldsymbol{v} \in \mathbb{F}^{N\times N}$. Let d be the grade of $\boldsymbol{v}$ with respect to A.

Output: orthonormal vectors $\boldsymbol{v}_1, \ldots, \boldsymbol{v}_d$ with $\mathrm{span}\{\boldsymbol{v}_1, \ldots, \boldsymbol{v}_n\} = \mathcal{K}_n(A, \boldsymbol{v})$ for $n = 1, 2, \ldots, d$.

Initialisation :$\boldsymbol{v}_0 = \boldsymbol{0}$, $\delta_1 = 0$, $\boldsymbol{v}_1 = \boldsymbol{v}/|\boldsymbol{v}|$.

1: **for** $i = 1$ to d **do**
2: $\quad \boldsymbol{u}_i = A\boldsymbol{v}_i - \delta_i \boldsymbol{v}_{i-1}$,
3: $\quad \hat{\boldsymbol{v}}_{i+1} = \boldsymbol{u}_i - \gamma_n \boldsymbol{v}_i$, where $\gamma_i = (\boldsymbol{u}_i, \boldsymbol{v}_i)$,
4: $\quad \delta_{i+1} = |\hat{\boldsymbol{v}}_{i+1}|$
5: $\quad$ **if** $\delta_{i+1} \neq 0$ **then**
6: $\quad\quad \boldsymbol{v}_{i+1} = \hat{\boldsymbol{v}}_{i+1}/\delta_{i+1}$,
7: $\quad$ **else**
8: $\quad\quad$ **return** $\boldsymbol{v}_1, \ldots, \boldsymbol{v}_i$.
9: $\quad$ **end if**
10: **end for**
11: **return** $\boldsymbol{v}_1, \ldots, \boldsymbol{v}_d$.

Proposition 1. In the Arnoldi algorithm 1, it holds that $h_{j,i} = 0, j \leq i-2$ when the matrix A is symmetric.

Proof. In the Arnoldi algorithm, $h_{j,i}$ can be obtained by

$$h_{j,i} = (A\boldsymbol{v}_i, \boldsymbol{v}_j). \tag{3.9}$$

Due to the symmetry of the matrix A, it can be written as

$$h_{j,i} = (\boldsymbol{v}_i, A\boldsymbol{v}_j). \tag{3.10}$$

Using the polynomial form, we find that $A\boldsymbol{v}_j = AV_{j-1}(A)\boldsymbol{v} \in \mathcal{K}_{j+1}(A, \boldsymbol{v}) \subset \mathcal{K}_{i-1}(A, \boldsymbol{v})$ since $\lambda V_{j-1}(\lambda)$ is at most a polynomial of degree $i-1$. Because $\boldsymbol{v}_i$ is orthogonal to the Krylov subspace $\mathcal{K}_{i-1}(A, \boldsymbol{v})$, in other words, it holds that $\boldsymbol{v}_i \perp \mathcal{K}_{i-1}(A, \boldsymbol{v})$, we have

$$h_{j,i} = (\boldsymbol{v}_i, A\boldsymbol{v}_j) = 0, \quad j \leq i-2. \tag{3.11}$$

□

The important part of the proof is the symmetry of A. When A is non-Hermitian, it holds that $(A\boldsymbol{v}_i, \boldsymbol{v}_j) = (\boldsymbol{v}_i, A^*\boldsymbol{v}_j)$. Thus, the vector $A^*\boldsymbol{v}_j$ is not included in the Krylov subspace $\mathcal{K}_{j+1}(A, \boldsymbol{v})$. One approach to obtain the three-term recurrence relation is to generate two sets of biorthogonal basis vectors using the non-Hermitian Lanczos algorithm

[87]. In the non-Hermitian Lanczos algorithm, we start from two initial vectors $\boldsymbol{v}, \boldsymbol{w} \in \mathbb{F}^N$ and consider two Krylov subspaces $\mathcal{K}_n(A, \boldsymbol{v}), \mathcal{K}_n(A^*, \boldsymbol{v})$. The vectors $\boldsymbol{v}_n = V_{n-1}(A)\boldsymbol{v} \in \mathcal{K}_n(A, \boldsymbol{v}), \boldsymbol{w}_n = W_{n-1}(A^*)\boldsymbol{w} \in \mathcal{K}_n(A^*, \boldsymbol{w})$ are constructed to satisfy the biorthogonal condition $(\boldsymbol{v}_i, \boldsymbol{w}_j) = \delta_{ij}$ where δ_{ij} is Kronecker's delta.

Let us consider the i-th step Gram-Schmidt biorthogonalization,

$$\hat{\boldsymbol{v}}_{i+1} = A\boldsymbol{v}_i - \sum_{j=1}^{i} h_{j,i}\boldsymbol{v}_j, \quad \text{where } h_{j,i} = (A\boldsymbol{v}_i, \boldsymbol{w}_j), \tag{3.12}$$

$$\hat{\boldsymbol{w}}_{i+1} = A^*\boldsymbol{w}_i - \sum_{j=1}^{i} k_{j,i}\boldsymbol{w}_j, \quad \text{where } k_{j,i} = (\boldsymbol{v}_i, A^*\boldsymbol{w}_j). \tag{3.13}$$

Then, we can prove the following proposition.

Proposition 2. In the above Gram-Schmidt biorthogonalization, it holds that $h_{j,i} = k_{j,i} = 0, j \leq i-2$.

Proof. Note that we already have the biorthogonal conditions

$$\boldsymbol{v}_i \perp \mathcal{K}_{i-1}(A^*, \boldsymbol{w}), \tag{3.14}$$

$$\boldsymbol{w}_i \perp \mathcal{K}_{i-1}(A, \boldsymbol{v}). \tag{3.15}$$

The coefficient $h_{j,i}$ can be written as

$$h_{j,i} = (A\boldsymbol{v}_i, \boldsymbol{w}_j) = (\boldsymbol{v}_i, A^*\boldsymbol{w}_j) \tag{3.16}$$

where $A^*\boldsymbol{w}_j \in \mathcal{K}_{j+1}(A^*, \boldsymbol{w}) \subset \mathcal{K}_{i-1}(A^*, \boldsymbol{w})$. Using the biorthogonal condition, we have $h_{j,i} = 0, j \leq i-2$. In the same way, we obtain $k_{j,i} = 0, j \leq i-2$. □

Therefore, we find that the three-term recurrence relation holds in the case of non-Hermitian matrices as follows:

$$\hat{\boldsymbol{v}}_{n+1} = A\boldsymbol{v}_n - h_{n,n}\boldsymbol{v}_n - h_{n-1,n}\boldsymbol{v}_{n-1}, \tag{3.17}$$

$$\hat{\boldsymbol{w}}_{n+1} = A^*\boldsymbol{w}_n - k_{n,n}\boldsymbol{w}_n - k_{n-1,n}\boldsymbol{w}_{n-1}, \quad n = 1, 2, \ldots. \tag{3.18}$$

The algorithm to obtain the biorthonormal bases is shown in Algorithm 3. Suppose that the non-Hermitian Lanczos algorithm does not stop until n step iteration. Then, we have biorthogonal system $\boldsymbol{v}_1, \ldots, \boldsymbol{v}_{n+1}, \boldsymbol{w}_1, \ldots, \boldsymbol{w}_{n+1}$ where $(\boldsymbol{v}_i, \boldsymbol{w}_j) = \delta_{ij}$ for $i, j = 1, \ldots, n+1$. In addition, it holds that

$$\mathrm{span}\{\boldsymbol{v}_1, \ldots \boldsymbol{v}_{n+1}\} = \mathcal{K}_{n+1}(A, \boldsymbol{v}), \quad \mathrm{span}\{\boldsymbol{w}_1, \ldots \boldsymbol{w}_{n+1}\} = \mathcal{K}_{n+1}(A^*, \boldsymbol{w}), \tag{3.19}$$

and

$$\boldsymbol{v}_i = V_{i-1}(A)\boldsymbol{v}, \quad \boldsymbol{w}_i = W_{i-1}(A^*)\boldsymbol{w}, \quad i = 1, \ldots, n+1, \tag{3.20}$$

Algorithm 3 non-Hermitian Lanczos algorithm

Input: matrix $A \in \mathbb{F}^{N\times N}$, nonzero vector $\boldsymbol{v} \in \mathbb{F}^{N\times N}$, iteration step n.

Output: biorthonormal vectors $\boldsymbol{v}_1, \ldots, \boldsymbol{v}_n$ with $\mathrm{span}\{\boldsymbol{v}_1, \ldots, \boldsymbol{v}_n\} = \mathcal{K}_n(A, \boldsymbol{v})$ and $\boldsymbol{w}_1, \ldots, \boldsymbol{w}_n$ with $\mathrm{span}\{\boldsymbol{w}_1, \ldots, \boldsymbol{w}_n\} = \mathcal{K}_n(A^*, \boldsymbol{w})$, so that $(\boldsymbol{v}_i, \boldsymbol{w}_j) = \delta_{ij}$ for $i, j = 1, 2, \ldots, n$.

Initialisation :$\boldsymbol{v}_0 = \boldsymbol{w}_0 = \boldsymbol{0}$, $\beta_1 = \delta_1 = 0$, $\boldsymbol{v}_1 = \boldsymbol{v}/|\boldsymbol{v}|$, $\boldsymbol{w}_1 = \boldsymbol{w}/\overline{(\boldsymbol{v}_1, \boldsymbol{w})}$.

for $i = 1$ to d **do**
  $\hat{\boldsymbol{v}}_{i+1} = A\boldsymbol{v}_i - \gamma_i \boldsymbol{v}_i - \beta_i \boldsymbol{v}_{i-1}$, where $\gamma_i = (A\boldsymbol{v}_i, \boldsymbol{w}_i)$,
  $\hat{\boldsymbol{w}}_{i+1} = A^*\boldsymbol{w}_i - \overline{\gamma}_i \boldsymbol{w}_i - \delta_i \boldsymbol{w}_{i-1}$,
  $\delta_{i+1} = |\hat{\boldsymbol{v}}_{i+1}|$,
  if $\delta_{i+1} \neq 0$ **then**
    $\boldsymbol{v}_{i+1} = \hat{\boldsymbol{v}}_{i+1}/\delta_{i+1}$,
    $\beta_{i+1} = (\boldsymbol{v}_{n+1}, \hat{\boldsymbol{w}}_{i+1})$,
    if $\beta_{i+1} \neq 0$ **then**
      $\boldsymbol{w}_{i+1} = \hat{\boldsymbol{w}}_{i+1}/\overline{\beta}_{i+1}$,
    else
      return $\boldsymbol{v}_1, \ldots, \boldsymbol{v}_i$, and $\boldsymbol{w}_1, \ldots, \boldsymbol{w}_i$,
    end if
  else
    return $\boldsymbol{v}_1, \ldots, \boldsymbol{v}_i$, and $\boldsymbol{w}_1, \ldots, \boldsymbol{w}_i$.
  end if
end for
return $\boldsymbol{v}_1, \ldots, \boldsymbol{v}_i$, and $\boldsymbol{w}_1, \ldots, \boldsymbol{w}_d$.

where $V_{i-1}(\lambda)$ and $W_{i-1}(\lambda)$ are the polynomials of exact degree $i-1$. The matrix form of the non-Hermitian Lanczos algorithm becomes

$$AV_n = V_n T_n + \delta_{n+1}\boldsymbol{v}_{n+1}\boldsymbol{e}_n^\top, \tag{3.21}$$

$$A^*W_n = W_n T_n^* + \beta_{n+1}^*\boldsymbol{w}_{n+1}\boldsymbol{e}_n^\top, \tag{3.22}$$

$$W_n^* A V_n = T_n, \tag{3.23}$$

$$W_{n+1}^* V_{n+1} = I_{n+1}, \quad |\boldsymbol{v}_1| = |\boldsymbol{v}_2| = \cdots = |\boldsymbol{v}_{n+1}| = 1 \tag{3.24}$$

where $V_n = [\boldsymbol{v}_1, \boldsymbol{v}_2, \ldots, \boldsymbol{v}_n], W_n = [\boldsymbol{w}_1, \boldsymbol{w}_2, \ldots, \boldsymbol{w}_n]$ are the matrix whose column is the

biorthonormal Krylov subspace bases, I_n is the n-th identity matrix, and

$$T_n = \begin{bmatrix} \gamma_1 & \beta_2 & & & 0 \\ \delta_2 & \gamma_2 & \beta_3 & & \\ & \ddots & \ddots & \ddots & \\ & & \delta_{n-1} & \gamma_{n-1} & \beta_n \\ 0 & & & \delta_n & \gamma_n \end{bmatrix}. \tag{3.25}$$

The non-Hermitian Lanczos algorithm can unexpectedly stop when it becomes $\delta_{i+1} = 0$ or $\beta_{i+1} = 0$. This situation may occur if it holds $\hat{\boldsymbol{v}}_{i+1} = \boldsymbol{0}$, $\hat{\boldsymbol{w}}_{i+1} = \boldsymbol{0}$, or $\boldsymbol{v}_{i+1} \perp \hat{\boldsymbol{w}}_{i+1}$. When $\hat{\boldsymbol{v}}_{i+1} = \boldsymbol{0}$ or $\hat{\boldsymbol{w}}_{i+1} = \boldsymbol{0}$, this means that the algorithm has found an invariant space. If $\hat{\boldsymbol{v}}_{i+1} = \boldsymbol{0}$, $\mathrm{span}\{\boldsymbol{v}_1, \dots \boldsymbol{v}_i\}$ is then A-invariant space while if $\hat{\boldsymbol{w}}_{i+1} = \boldsymbol{0}$, $\mathrm{span}\{\boldsymbol{w}_1, \dots \boldsymbol{w}_i\}$ is A^*-invariant space. This situation is very desirable because the vectors contain all the information about the matrix A. This is often called "luckly breakdown" [88]. When $\beta_{i+1} = (\boldsymbol{v}_{i+1}, \hat{\boldsymbol{w}}_{i+1}) = 0$, the algorithm has computed no invariant subspace of A or A^*. This sometimes happen and it is often called "serious breakdown" since it is not desirable situation. There are several attempts to avoid the problem of breakdowns in the Lanczos algorithm. A look-ahead versions of the Lanczos algorithm can often be very useful choice [89, 90].

3.1.4 Self-adjoint Lanczos algortihm

The other generalization of the Hermitian Lanczos algorithm is to change the definition of the symmetry. Let us consider the bilinear form $B : V \times V \to \mathbb{F}$ which satisfy,

$$B(\boldsymbol{u} + \boldsymbol{v}, \boldsymbol{w}) = B(\boldsymbol{u}, \boldsymbol{w}) + B(\boldsymbol{v}, \boldsymbol{w}), \quad \text{where } \boldsymbol{u}, \boldsymbol{v}, \boldsymbol{w} \in V \tag{3.26a}$$

$$B(\boldsymbol{u}, \boldsymbol{v} + \boldsymbol{w}) = B(\boldsymbol{u}, \boldsymbol{v}) + B(\boldsymbol{u}, \boldsymbol{v}), \tag{3.26b}$$

$$B(\lambda \boldsymbol{u}, \boldsymbol{v}) = B(\boldsymbol{u}, \overline{\lambda}\boldsymbol{v}) = \lambda B(\boldsymbol{u}, \boldsymbol{v}), \quad \text{where } \lambda \in \mathbb{F}. \tag{3.26c}$$

If the bilinear form $H : V \times V \to \mathbb{C}$ satisfies the following properties

$$\text{Hermitian symmetry :} \quad H(\boldsymbol{x}, \boldsymbol{y}) = \overline{H(\boldsymbol{y}, \boldsymbol{x})}, \tag{3.27a}$$

$$\text{Positive definite :} \quad H(\boldsymbol{x}, \boldsymbol{x}) > 0, \quad \text{if } \boldsymbol{x} \neq \boldsymbol{0}, \tag{3.27b}$$

$$\text{non-degenerate :} \quad H(\boldsymbol{x}, \boldsymbol{x}) = 0, \quad \text{iff } \boldsymbol{x} = \boldsymbol{0}, \tag{3.27c}$$

H is called Hermitian form which satisfies the definition of the inner product. The following is the examples of the Hermitian form.

Euclidean space

Let $\boldsymbol{x}, \boldsymbol{y} \in \mathbb{R}^N$, then the Euclidean inner product

$$(\boldsymbol{x}, \boldsymbol{y}) = \sum_{i=1}^{N} x_i y_i \tag{3.28}$$

is the Hermitian form.

Complex coordinate system

Let $\boldsymbol{x}, \boldsymbol{y} \in \mathbb{C}^N$, $G \in \mathbb{C}^{N\times N}$ be a positive-definite symmetric matrix, then

$$(\boldsymbol{x}, \boldsymbol{y})_G = \boldsymbol{y}^\dagger G \boldsymbol{x} \tag{3.29}$$

is the Hermitian form. If $(\boldsymbol{x}, \boldsymbol{y})_G = 0$ holds for the nonzero vectors $\boldsymbol{x}, \boldsymbol{y}$, the vectors $\boldsymbol{x}, \boldsymbol{y}$ are called G-orthogonal. For the generalization, the condition of the matrix G can be relaxed to the positive-semidefinite symmetric matrix or simply symmetric matrix.

Lebesgue space

Let f, g are the functions in the Lebesgue space $L^2(\Omega)$ in which the functions are square integrable. Then, the following integral

$$\langle f, g\rangle = \int_\Omega f(x)\overline{g}(x)dx \tag{3.30}$$

is the Hermitian form. Now, we define the symmetric operator A with respect to the Hermitian form. For example, if we consider the complex coordinate system, we can find the symmetric operator which satisfies

$$(A\boldsymbol{x}, \boldsymbol{y})_G = (\boldsymbol{x}, A\boldsymbol{y})_G. \tag{3.31}$$

The necessary condition to the symmetric operator here is to hold

$$AG = GA^*. \tag{3.32}$$

To distinguish it from the case of the Euclid inner product, we call such a "symmetric" matrix A self-adjoint matrix with respect to G. If we find the self-adjoint matrices, we can readily extend the Hermitian Lanczos algorithm only by changing the definition of the inner product as shown in Algorithm 4. Note that $|\cdot|_G = \sqrt{(\cdot,\cdot)_G}$ denotes the norm which is sometimes called a energy norm in the finite element analysis. The matrix form of the self-adjoint Lanczos algorithm has the same form as that in the Hermitian Lanczos algorithm.

The self-adjoint Lanczos algorithm plays important role in the discussion in the following section to relate PVL and CLN.

3.1.5 Padé approximation via Lanczos

As mentioned in Chapter 1, PVL [25] is mathematically equivalent to AWE [22] but numerically more stable. It utilizes the non-Hermitian Lancozs algorithm to compute the moments. In this section, we describe a method for calculating the moments in PVL using the non-Hermitian Lanczos method.

Algorithm 4 self-adjoint Lanczos algorithm

Input: symmetric positive-definite matrix $G \in \mathbb{C}^{N\times N}$, self-adjoint matrix $A \in \mathbb{F}^{N\times N}$ with respect to G, nonzero vector $\boldsymbol{v} \in \mathbb{F}^{N\times N}$, Let d be the grade of $\boldsymbol{v}$ with respect to A.

Output: orthonormal vectors $\boldsymbol{v}_1, \ldots, \boldsymbol{v}_d$ with $\mathrm{span}\{\boldsymbol{v}_1, \ldots, \boldsymbol{v}_n\} = \mathcal{K}_n(A, \boldsymbol{v})$ for $n = 1, 2, \ldots, d$.

Initialisation :$\boldsymbol{v}_0 = \boldsymbol{0}$, $\delta_1 = 0$, $\boldsymbol{v}_1 = \boldsymbol{v}/|\boldsymbol{v}|_G$.

1: **for** $i = 1$ to d **do**
2: $\quad \boldsymbol{u}_i = A\boldsymbol{v}_i - \delta_i \boldsymbol{v}_{i-1}$,
3: $\quad \hat{\boldsymbol{v}}_{i+1} = \boldsymbol{u}_i - \gamma_n \boldsymbol{v}_i$, where $\gamma_i = (\boldsymbol{u}_i, \boldsymbol{v}_i)_G$,
4: $\quad \delta_{i+1} = |\hat{\boldsymbol{v}}_{i+1}|_G$
5: $\quad$ **if** $\delta_{i+1} \neq 0$ **then**
6: $\quad\quad \boldsymbol{v}_{i+1} = \hat{\boldsymbol{v}}_{i+1}/\delta_{i+1}$,
7: $\quad$ **else**
8: $\quad\quad$ **return** $\boldsymbol{v}_1, \ldots, \boldsymbol{v}_i$.
9: $\quad$ **end if**
10: **end for**
11: **return** $\boldsymbol{v}_1, \ldots, \boldsymbol{v}_d$.

Let us consider the time-invariant single-input-single-output (SISO) system:

$$G\boldsymbol{x} + C\frac{d\boldsymbol{x}}{dt} = \boldsymbol{b}u, \tag{3.33a}$$

$$y = \boldsymbol{l}^\top \boldsymbol{x} \tag{3.33b}$$

where $G, C \in \mathbb{R}^{N\times N}$, $\boldsymbol{x}, \boldsymbol{b}, \boldsymbol{l} \in \mathbb{R}^N$. $u, y \in \mathbb{R}$ are the input and output of the system. Since PVL was proposed in the community of the electric circuit analysis, the representation of the coefficient matrix G, C is from the conductance and capacitance matrix in the node-voltage equations. By using the Laplace transform, the system is represented in the frequency domain as follows:

$$G\boldsymbol{x} + sC\boldsymbol{x} = \boldsymbol{b}U(s), \tag{3.34a}$$

$$Y(s) = \boldsymbol{l}^\top \boldsymbol{x} \tag{3.34b}$$

where $Y(s), U(s)$ are the Laplace transform of y, u, and s is the complex frequency. The impulse response, i.e. the transfer function of the system can be written as

$$\mathcal{H}(s) = \frac{Y}{U} = \boldsymbol{l}^\top (G + sC)^{-1}\boldsymbol{b}. \tag{3.35}$$

Let $s_0 \in \mathbb{C}$ be the arbitrary fixed expansion such that $G + s_0 C$ is non-singular, and

$$A = -(G + s_0 C)^{-1} C, \quad \boldsymbol{r} = (G + s_0 C)^{-1}\boldsymbol{b}. \tag{3.36}$$

Setting $\sigma = s - s_0$, we can rewrite the transfer function as follows:

$$\mathcal{H}(\sigma) = \boldsymbol{l}^\top (I - \sigma A)^{-1} \boldsymbol{r}. \tag{3.37}$$

Assuming that the matrix A is diagonalisable, we can find $A = S\Lambda S^{-1}$ where $\Lambda = \mathrm{diag}[\lambda_1, \ldots, \lambda_N]$ whose diagonal component is the eigenvalue of A, and S is composed of the eigenvectors of A. The transfer function can be computed by

$$\begin{aligned}
\mathcal{H}(\sigma) &= \boldsymbol{l}^\top (I - \sigma A)^{-1} \boldsymbol{r} \\
&= (\underbrace{S^\top \boldsymbol{l}}_{\boldsymbol{f}})^\top (I - \sigma\Lambda)^{-1} (\underbrace{S^{-1}\boldsymbol{r}}_{\boldsymbol{g}}) \\
&= \sum_{i=0}^{N} \frac{f_i g_i}{1 - \sigma\lambda_i}.
\end{aligned} \tag{3.38}$$

Note that the dimension of the system N that arises from FE analysis or circuit analysis would be usually large. Thus, it is almost impossible to compute all the eigenvalues and eigenvectors of A. Therefore, we have to depend on approximate methods. One method is partial realization. This is the idea of constructing an approximation of order n by strictly computing the first n terms of the Taylor expansion. To do this, we consider the Taylor expansion of the transfer function around $s = s_0$ as follows:

$$\begin{aligned}
\mathcal{H}(\sigma) = \boldsymbol{l}^\top (I - \sigma A)^{-1} \boldsymbol{r} &= \sum_{i=0}^{\infty} \boldsymbol{l}^\top A^i \boldsymbol{r} \sigma^i, \\
&= \sum_{i=0}^{\infty} m_i \sigma^i
\end{aligned} \tag{3.39}$$

where $m_i = \boldsymbol{l}^\top A^i \boldsymbol{r}$ is called moment. If we compute the first n moments, we can obtain the reduced-order system of the order n. In AWE, the moments are explicitly computed. After the computation of the moments, however, we have to solve an equation that has a very ill-conditioned coefficient matrix. To avoid the difficulty, the non-Hermitian Lanczos algorithm is used in PVL.

Setting the initial vectors $\boldsymbol{l}, \boldsymbol{r}$, we obtain the set of biorthogonal vectors in $\mathcal{K}_n(A, \boldsymbol{r})$ and $\mathcal{K}_n(A^\top, \boldsymbol{l})$ by the non-Hermitian Lanczos algorithm. Note that we assume that the breakdown does not occur in this case. From the matrix form of the non-Hermitian Lanczos algorithm, we obtain

$$AV_n = V_n T_n + \delta_{n+1} \boldsymbol{v}_{n+1} \boldsymbol{e}_n^\top, \tag{3.40}$$

$$A^\top W_n = W_n T_n^\top + \beta_{n+1} \boldsymbol{w}_{n+1} \boldsymbol{e}_n^\top. \tag{3.41}$$

where

$$T_n = \begin{bmatrix} \gamma_1 & \beta_2 & & & 0 \\ \delta_2 & \gamma_2 & \beta_3 & & \\ & \ddots & \ddots & \ddots & \\ & & \delta_{n-1} & \gamma_{n-1} & \beta_n \\ 0 & & & \delta_n & \gamma_n \end{bmatrix}. \tag{3.42}$$

Then, the $2i$-th moments ($i = 0, 1, \ldots, n-1$) can be computed as

$$\begin{aligned} m_{2i} &= \boldsymbol{l}^\top A^{2i} \boldsymbol{r} \\ &= ((A^\top)^i \boldsymbol{l})^\top (A^i \boldsymbol{r}) \\ &= \boldsymbol{w}^\top \boldsymbol{v} \cdot ((A^\top)^i W_n \boldsymbol{e}_1)^\top (A^i V_n \boldsymbol{e}_1) \\ &= \boldsymbol{w}^\top \boldsymbol{v} \cdot (W_n (T_n^\top)^i \boldsymbol{e}_1)^\top (V_n T_n^i \boldsymbol{e}_1) \\ &= \boldsymbol{w}^\top \boldsymbol{v} \cdot \boldsymbol{e}_1^\top T_n^{2i} \boldsymbol{e}_1. \end{aligned} \tag{3.43}$$

The $2i+1$-th moments ($i = 0, 1, \ldots, n-1$) can also be computed by the same procedure. Note that there is no approximation in the computation of the moments. If we truncate the non-Hermitian Lanczos algorithm at n step iteration, we obtain $2n$ moments. The partial realization of the transfer function becomes

$$\begin{aligned} \mathcal{H}(\sigma) &\approx \mathcal{H}_n(\sigma) \\ &= \sum_{i=0}^{2n} m_i s^i \\ &= \boldsymbol{w}^\top \boldsymbol{v} \sum_{i=0}^{2n} \boldsymbol{e}_1^\top T_n^{2i} \boldsymbol{e}_1 \sigma^i \\ &= \boldsymbol{w}^\top \boldsymbol{v} \cdot \boldsymbol{e}_1^\top (I - \sigma T_n)^{-1} \boldsymbol{e}_1. \end{aligned} \tag{3.44}$$

The reduced-order transfer function is the rational function whose denominator and numerator are polynomials of $n, n-1$ degree. Since the Taylor expansion of the reduced-order transfer function matches first $2n$ terms, the reduced-order transfer function is the n-th Padé approximation of the full-order transfer function. This kind of connection between the Lanczos algorithm and Padé approximation is called *Lanczos Padé connection* [25].

The size of the tridiagonal matrix T_n is quite small, so that eigendecomposition can be performed $T_n = S_n \Lambda_n S_n^{-1}$. Substituting it to the reduced-order transfer function, we

obtain pole/residue representation as follows:

$$\begin{aligned}\mathcal{H}_n(\sigma) &= \boldsymbol{w}^\top \boldsymbol{v} \cdot \boldsymbol{e}_1^\top (I - \sigma T_n)^{-1} \boldsymbol{e}_1 \\ &= \boldsymbol{w}^\top \boldsymbol{v} \cdot \underbrace{(S_n^\top \boldsymbol{e}_1)}_{\boldsymbol{\mu}}{}^\top (1 - \sigma \Lambda_n)^{-1} \underbrace{S_n^{-1} \boldsymbol{e}_1}_{\boldsymbol{\nu}} \\ &= \sum_{i=1}^{n} \frac{\boldsymbol{w}^\top \boldsymbol{v} \mu_i \nu_i}{1 - \sigma \lambda_i} \\ &= k_\infty - \sum_{i=1, \lambda_i \neq 0}^{n} \frac{\boldsymbol{w}^\top \boldsymbol{v} \mu_i \nu_i / \lambda_i}{\sigma - 1/\lambda_i}\end{aligned} \tag{3.45}$$

where λ_i is the approximate eigenvalues of the full-order transfer function. Note that k_∞ may exist when Λ_n has zero eigenvalues. It has been pointed out that the PVL method does not preserve the passivity of the original system [25] although the original full-order system is passive. Roughly speaking, the passivity is the property of whether the system generates energy or not. The system is called passive if it does not generate energy. This property is important for the reduced-order model since it may be a non-physical model when the reduced-order model is not passive. The sufficient condition of the passivity is given in [91, 29].

As a special case of the PVL method, Freund proposed a symmetric variant of PVL (SyPVL) [27] that requires only half the computational cost and storage. In this method, we assume a transfer function of the form

$$\mathcal{H}(s) = \boldsymbol{b}^\top (G + sC)^{-1} \boldsymbol{b} \tag{3.46}$$

where G, C are the symmetric matrices. Such transfer function arises from the circuit equation of RLC circuits. By exploiting the symmetry of the transfer function, we can simplify the non-Hermitian Lanczos algorithm and reduce the computational cost and storage. As a result, we obtain the Padé approximation of the transfer function as follows:

$$\mathcal{H}_q(s) = \boldsymbol{b}^\top G^{-1} \boldsymbol{b} \boldsymbol{e}_1^\top (I - sT_n)^{-1} \boldsymbol{e}_1 \tag{3.47}$$

It can be shown that the reduced-order model is always passive when G, C are positive definite.

3.2 Cauer circuit generation from Maxwell's equations

3.2.1 Network synthesis of a rational function

To realize a rational function by the lumped element network, the Foster and Cauer circuits have been widely used in the field of the system control [92], thermal simulation [93], electromagnetic simulation [94], and so on [95, 96]. The circuit topology of the Foster and Cauer circuits are illustrated in Fig. 3.1-3.4.

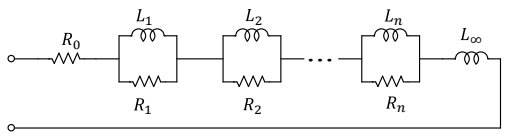

Figure3.1: Foster I form of $Z(s)$.

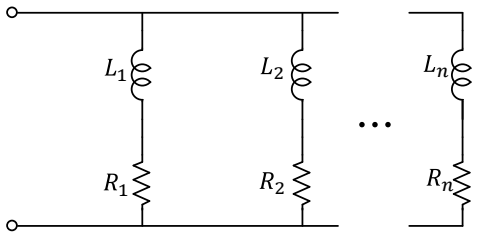

Figure3.2: Foster II form of $Y(s) = Z^{-1}(s)$.

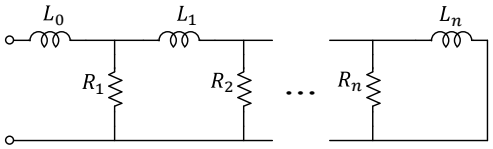

Figure3.3: Cauer I form of $Z(s)$.

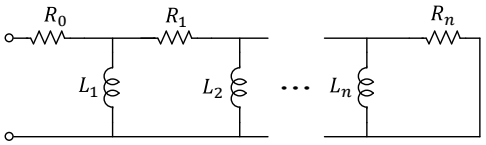

Figure3.4: Cauer II form of $Z(s)$.

The Foster [97] and Cauer circuits [98] are relevant to the partial fraction expansion and continued fraction expansions of a positive-real function (PRF) $Z_{n,n-1}(s) = Q_n(s)/P_{n-1}(s)$ where $P_{n-1}(s), Q_n(s)$ are polynomials of exact degree $n-1, n$. The complex function $Z(s)$ is PRF if it holds that

$$\mathrm{Re}[Z(s)] > 0, \quad \text{if } \mathrm{Re}[s] > 0, \tag{3.48}$$
$$\mathrm{Im}[Z(s)] = 0, \quad \text{if } \mathrm{Im}[s] = 0. \tag{3.49}$$

In general, PRF is a class of functions that can be realized by the two or three kinds element networks [99]. If the system is composed of the resistance and inductance, the impedance can be written as

$$Z_{n,n-1}(s) = \frac{a_n(s+\alpha_1)\cdots(s+\alpha_{2n-1})}{b_m(s+\alpha_2)\cdots(s+\alpha_{2n-2})}, \quad \text{where } \frac{a_n}{b_m} > 0, \quad 0 \le \alpha_1 \le \alpha_2 \le \cdots \le \alpha_{2n-2} \le \alpha_{2n-1}. \tag{3.50}$$

Note that $Z_{n,n-1}(s)$ has n real negative zeros and $n-1$ real negative poles, and $Z_{n,n-1}(s)$ is a PRF. $Z_{n+1,n}(s)$ can be expanded into a partial fraction such that

$$\begin{aligned} Z_{n,n-1}(s) &= h_0 + \sum_{k=1}^{n} \frac{sh_{2k}}{s+\alpha_{2k}} + sh_\infty \\ &= h_0 + \sum_{k=1}^{n} \frac{1}{\frac{1}{h_{2k}} + \frac{\alpha_{2k}}{sh_{2k}}} + sh_\infty \\ &= R_0 + \sum_{k=1}^{n} \frac{1}{\frac{1}{R_k} + \frac{1}{sL_k}} + sL_\infty \end{aligned} \tag{3.51}$$

This function can be seen as the series connection of the RL parallel circuits. The circuit representation is called Foster I form shown in Fig. 3.1. Similarly, if we expand the admittance $Y_{n,n+1}(s) = Z^{-1}_{n+1,n}(s)$ into a partial fraction, we get

$$\begin{aligned} Y_{n-1,n}(s) &= \sum_{k=1}^{n} \frac{h_{2k-1}}{s+\alpha_{2k-1}} \\ &= \sum_{k=1}^{n} \frac{1}{\frac{s}{h_{2k-1}} + \frac{\alpha_{2k-1}}{h_{2k-1}}} \\ &= \sum_{k=1}^{n} \frac{1}{sL_k + R_k} \end{aligned} \tag{3.52}$$

This function can be seen as the parallel connection of the RL series circuits. The circuit representation is called Foster II form shown in Fig. 3.2.

The other realization can be obtained by the continued fraction expansion of the rational function. Applying the Euclidean algorithm to the rational function $Z_{n,n-1}(s)$, we obtain

$$\begin{aligned} Z_{n,n-1}(s) &= \frac{a_n(s+\alpha_1)\cdots(s+\alpha_{2n-1})}{b_m(s+\alpha_2)\cdots(s+\alpha_{2n-2})} \\ &= \frac{a_n(s^n + q_{n-1}s^{n-1} + \cdots + q_1 s + q_0)}{b_m(s^{n-1} + p_{n-2}s^{n-2} + \cdots + p_1 s + p_0)} \\ &= \frac{a_n}{b_m}s + \frac{(a_n q_{n-1} - b_m)s^{n-1} + \cdots + (a_n q_1 - b_m p_1)s + (a_n q_0 - b_m p_0)}{b_m(s^{n-1} + p_{n-2}s^{n-2} + \cdots + p_1 s + p_0)} \\ &= \frac{a_n}{b_m}s + \cfrac{1}{\frac{b_m}{a_n q_{n-1} - b_m} + \cfrac{1}{\ddots}} \\ &= sL_0 + \cfrac{1}{\cfrac{1}{R_1} + \cfrac{1}{sL_1 + \cfrac{1}{\ddots + \cfrac{1}{\cfrac{1}{R_n} + \cfrac{1}{sL_n}}}}} \\ &= \left[sL_0; \tfrac{1}{R_1}, sL_1, \cdots, \tfrac{1}{R_n}, sL_n\right] \end{aligned} \tag{3.53}$$

As well known in the circuit theory, the continued fraction can be represented by the ladder circuit. The circuit representation is called Cauer I form shown in Fig. 3.3. Similarly, if

we start the Euclidean algorithm from the lowest order, we have

$$
\begin{aligned}
Z_{n,n-1}(s) &= \frac{a_n(s+\alpha_1)\cdots(s+\alpha_{2n-1})}{b_m(s+\alpha_2)\cdots(s+\alpha_{2n-2})} \\
&= \frac{a_n(s^n + q_{n-1}s^{n-1} + \cdots + q_1 s + q_0)}{b_m(s^{n-1} + p_{n-2}s^{n-2} + \cdots + p_1 s + p_0)} \\
&= \frac{a_n(1 + q_{n-1}t + \cdots + q_1 t^{n-1} + q_0 t^n)}{b_m(t + p_{n-2}t^2 + \cdots + p_1 t^{n-1} + p_0 t^n)} \\
&= \frac{a_n q_0}{b_m p_0} + \frac{a_n + (a_n q_{n-1} - b_m)t + \cdots + (a_n q_1 - b_m p_1)t^{n-1}}{b_m(t + p_{n-2}t^2 + \cdots + p_1 t^{n-1} + p_0 t^n)} \\
&= \frac{a_n q_0}{b_m p_0} + \cfrac{1}{\frac{tp_0}{a_n q_1 - b_m p_1} + \cfrac{1}{\ddots}} \\
&= R_0 + \cfrac{1}{\cfrac{1}{sL_1} + \cfrac{1}{R_1 + \cfrac{1}{\ddots + \cfrac{1}{\cfrac{1}{sL_n} + \cfrac{1}{R_n}}}}} \\
&= \left[R_0; \tfrac{1}{sL_1}, R_1, \cdots, \tfrac{1}{sL_n}, R_n\right]
\end{aligned}
\tag{3.54}
$$

where $t = s^{-1}$. The circuit realization is called Cauer II form shown in Fig. 3.4. Since the Foster and Cauer circuits are derived from the same function $Z_{n,n-1}(s)$, they have same zeros and poles and thus have same frequency characteristics although they are realized in different ways. So, there is no difference between these circuits mathematically. When we consider the eddy current problem, however, we can find the physical meaning in the Cauer II form which cannot be found in the Foster circuits. This fact can be effectively used when we consider the nonlinear properties of the electromagnetic apparatuses due to the saturation [21] and hysteresis [35].

3.2.2 Physical meaning of Cauer II form in eddy current problems

Let us consider the stationary limit ($\omega \to 0$) of the Cauer II form. In this limit, the current i_1 which flows in the primal inductor L_1 becomes dominant because $sL_1 \to 0$. When we consider the Cauer circuit as a circuit realization of the eddy current problems of the electromagnetic apparatuses, the primal inductor L_1 represents the direct current (DC) property of the magnetic field, and R_0 represents the DC resistance of the winding. The inductors $L_i, i \geq 2$ and resistors $R_i, i \geq 1$ in the higher stage of the ladder represent the diamagnetic properties of the eddy currents and resistances due to eddy current losses, respectively. These are consistent with the following physical description. In the electric apparatuses, the external electric field E_0 generates the DC magnetic field H_1. Then, from Faraday's law, the eddy currents E_1 are induced to prevent the time variation of H_1. The

eddy currents E_1 generate the diamagnetic field H_2. Then, the eddy currents $E_2, E_3, \ldots$ and diamagnetic fields $H_3, H_4, \ldots$ are generated in the similar way.

Using these physical meanings, the nonlinearity due to the saturation of the magnetic core can be introduced [21]. The magnetic field can be decomposed into the static and diamagnetic parts as follows

$$W(s) = \underbrace{\frac{\mathrm{j}\omega}{2} L_1 i_1^2}_{\text{static part}} + \underbrace{\frac{\mathrm{j}\omega}{2} L_2 i_2^2 + \frac{\mathrm{j}\omega}{2} L_3 i_3^2 + \ldots}_{\text{diamagnetic part}}. \tag{3.55}$$

This relation is also true when we consider the time domain analysis. Here, we introduce the assumption that the static part of the stored magnetic energy is dominant. From this assumption, we can consider the nonlinearity only depends on the primary current i_1. Since the stored magnetic energy can be obtained by the shaded area in Fig. 3.5, we can write it as

$$W_{\text{static}} = \int_0^{\Phi(i_1)} i d\Phi \tag{3.56}$$

where Φ denotes the interlinkage flux. By introducing $\Phi(i_1)$ to the primary inductor, we obtain the nonlinear Cauer circuit as shown in Fig. 3.6. The circuit equation of the first and second stage of the ladder can be written as

$$-\frac{d\Phi(i_1)}{dt} = e_0 - v, \tag{3.57}$$

$$\frac{d\Phi(i_1)}{dt} - L_2 \frac{di_2}{dt} = e_2. \tag{3.58}$$

The nonlinear equation can easily be solved by the Newton-Raphson method.

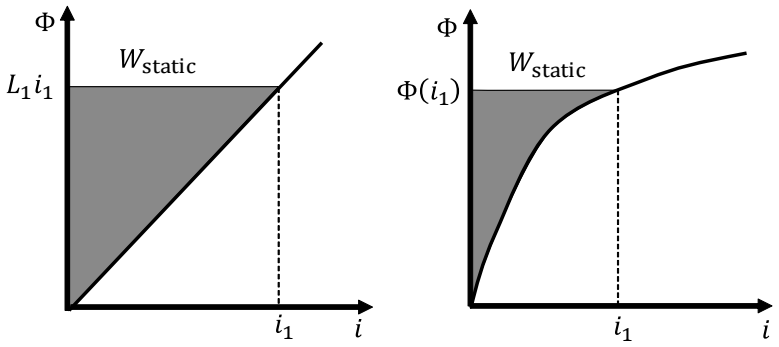

Figure3.5: Stored magnetic energy in the stationary limit. Left is linear case and right is nonlinear case.

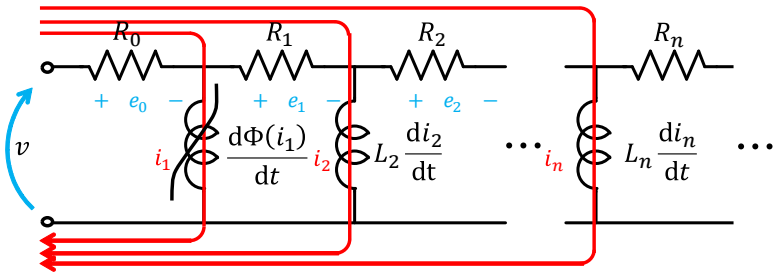

Figure3.6: Nonlinear Cauer circuit.

3.2.3 CLN method

There is an assumption that a Cauer II form has a relation to the orthogonal function expansion of the quasi-static electromagnetic fields. This assumption comes from the analysis of a one-dimensional magnetic steel sheet. The electromagnetic fields in a magnetic steel sheet can be represented by the linear combination of Legendre polynomials [100]. It has been pointed out that the norms of Legendre polynomials correspond to the circuit parameters in a Cauer circuit [34, 35]. In addition, the expansion coefficients of the magnetic and electric fields correspond to the currents and voltages in a Cauer circuit, respectively. Thus, the coefficients satisfy Kirchhoff's voltage law (KVL) and Kirchhoff's current law (KCL). Kameari et al. developed the CLN method [33] by assuming that this fact holds in three-dimensional (3D) quasi-static Maxwell's equations.

Let Ω be the open bounded domain in $\mathbb{R}^3$ whose boundary $\partial\Omega = \Gamma$ is composed of non-overlapping parts $\Gamma_{\mathrm{D}}, \Gamma_{\mathrm{N}}, \Gamma_{\mathrm{PEC}}$. The eddy current flows in the conductor domain Ω_{c} whose conductivity is $\sigma > 0$. $\Gamma_{\mathrm{PEC}} = \partial\Omega_{\mathrm{c}} \cap \Gamma$ is composed of $\Gamma_{\mathrm{in}}, \Gamma_{\mathrm{out}}$ which are located at a non-zero distance from each other. The domain is shown in Fig. 3.7. We consider the electromagnetic fields in Ω governed by MQS approximation of Maxwell's equations.

$$\nabla \times \boldsymbol{H}(t, \boldsymbol{x}) = \sigma \boldsymbol{E}(t, \boldsymbol{x}), \tag{3.59}$$

$$\nabla \times \boldsymbol{E}(t, \boldsymbol{x}) = -\frac{\partial \boldsymbol{B}(t, \boldsymbol{x})}{\partial t}. \tag{3.60}$$

The boundary conditions are given as

$$\boldsymbol{B}(t, \boldsymbol{x}) \cdot \boldsymbol{n} = 0, \quad \text{on } \Gamma_{\mathrm{D}} \cup \Gamma_{\mathrm{PEC}}, \tag{3.61}$$

$$\boldsymbol{H}(t, \boldsymbol{x}) \times \boldsymbol{n} = \boldsymbol{0}, \quad \text{on } \Gamma_{\mathrm{N}}, \tag{3.62}$$

$$\boldsymbol{E}(t, \boldsymbol{x}) \cdot \boldsymbol{n} = 0, \quad \text{on } \Gamma_{\mathrm{PEC}}. \tag{3.63}$$

The corresponding Cauer II form based on the previous assumption is illustrated in Fig.3.8.

The electromagnetic fields are supposed to be written as

$$\boldsymbol{H}(t,\boldsymbol{x}) = \sum_{n=1}^{\infty} h_n(t)\boldsymbol{H}_n(\boldsymbol{x}), \tag{3.64}$$

$$\boldsymbol{E}(t,\boldsymbol{x}) = \sum_{n=0}^{\infty} e_n(t)\boldsymbol{E}_n(\boldsymbol{x}) \tag{3.65}$$

where $h_n(t), e_e(t)$ and $\boldsymbol{H}_n(\boldsymbol{x}), \boldsymbol{E}_n(\boldsymbol{x})$ are the function of time t and position $\boldsymbol{x}$, respectively. It is assumed heuristically that $h_n(t), e_n(t)$ satisfy KVL and KCL of the Cauer circuit, which are given by

$$-L_1\frac{dh_1}{dt} = e_0 - v, \tag{3.66}$$

$$L_n\frac{dh_n}{dt} - L_{n+1}\frac{dh_{n+1}}{dt} = e_n, \quad n = 1, 2, \ldots, \tag{3.67}$$

$$\frac{e_0}{R_0} = i, \tag{3.68}$$

$$\frac{e_n}{R_n} - \frac{e_{n+1}}{R_{n+1}} = h_{n+1}, \quad n = 0, 1, \ldots \tag{3.69}$$

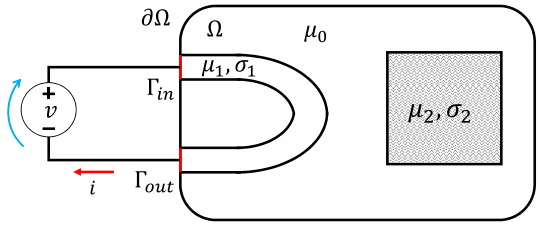

Figure3.7: Open bounded domain Ω and external power supply ©2020 IEEE.

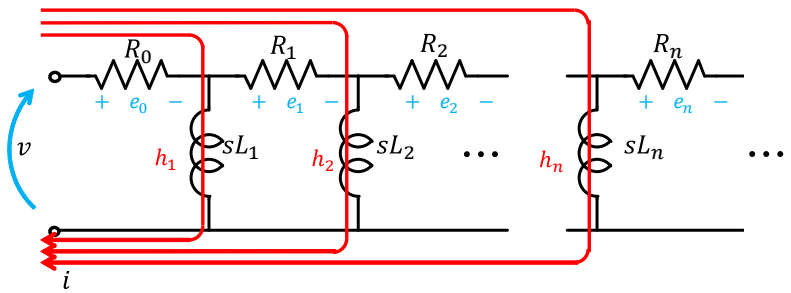

Figure3.8: Cauer II form corresponding to Ω.

For the reduced-order model, the instantaneous Joule losses $P(t)$ and the stored magnetic energy $W(t)$ between the full- and reduced-order model must be consistent. There-

fore, the following relation must be satisfied.

$$2W(t) = (\mu \boldsymbol{H}, \boldsymbol{H})_\Omega = \sum_{n=1}^{\infty} L_n h_n^2(t), \tag{3.70}$$

$$P(t) = (\sigma \boldsymbol{E}, \boldsymbol{E})_{\Omega_c} = \sum_{n=0}^{\infty} \frac{e_n^2(t)}{R_n} \tag{3.71}$$

where $(\cdot,\cdot)_\Omega$ is the inner product in the domain Ω. Substituting the space-time variable separation expression of the electromagnetic fields (3.64), (3.65) into the above equations and comparing coefficients of each $h_m(t)h_n(t)$ on both sides, we have

$$(\boldsymbol{H}_m, \mu \boldsymbol{H}_n)_\Omega = \int_\Omega \boldsymbol{H}_m \cdot \mu \boldsymbol{H}_n d\Omega = L_n \delta_{mn}, \quad m,n = 1,2,\ldots, \tag{3.72}$$

$$(\boldsymbol{E}_m, \sigma \boldsymbol{E}_n)_{\Omega_c} = \int_{\Omega_c} \boldsymbol{E}_m \cdot \sigma \boldsymbol{E}_n d\Omega = \frac{1}{R_n} \delta_{mn}, \quad m,n = 0,1,\ldots. \tag{3.73}$$

This means that the space relevant functions $\boldsymbol{H}_n(\boldsymbol{x}), \boldsymbol{E}_n(\boldsymbol{x})$ are orthogonal functions in the domain Ω. The orthogonal functions can be determined from the two-term recurrence relations obtained from Maxwell's equations. To do so, substituting (3.64), (3.65) into Maxwell's equations and considering (3.66)-(3.69), we obtain

$$\nabla \times (\boldsymbol{H}_n - \boldsymbol{H}_{n-1}) = \nabla \times \widetilde{\boldsymbol{H}}_n = R_{n-1} \sigma \boldsymbol{E}_{n-1}, \quad n = 1,2,\ldots, \tag{3.74}$$

$$\nabla \times (\boldsymbol{E}_n - \boldsymbol{E}_{n-1}) = \nabla \times \widetilde{\boldsymbol{E}}_n = -\frac{1}{L_n} \mu \boldsymbol{H}_n, \quad n = 1,2,\ldots, \tag{3.75}$$

where $\boldsymbol{E}_{-1} = \boldsymbol{0}$, $\boldsymbol{H}_0 = \boldsymbol{0}$. Iteratively solving the two-term recurrence relations, we obtain the orthogonal functions. Note that this procedure is equivalent to the Gram-Schmidt orthogonalization. The algorithm of the CLN is summarized in Algorithm 5. As a result, we obtain the Cauer circuit as a reduced-order model of the MQS approximation of Maxwell's equations.

3.2.4 CLN method with finite element discretization

In the previous part, we look at the algorithm of the CLN method which is formulated in the continuous space. To implement the algorithm numerically, we have to discretize the equations in the CLN method. In this part, we discretize the equations by FEM using the A method.

Firstly, the domain Ω is subdivided into appropriate finite elements. The vector potential discretized using the edge element $\boldsymbol{w}_i^e$ as follows:

$$\boldsymbol{A} \approx \sum_{i \in E(\Omega)} a_i \boldsymbol{w}_i^e \tag{3.76}$$

Algorithm 5 CLN method

Input: electric field $\boldsymbol{E}_0$ that satisfies $\nabla \times \boldsymbol{E}_0 = 0$ with 1 V power supply, iteration step n.

Output: orthogonal functions $\boldsymbol{E}_0, \ldots, \boldsymbol{E}_n$, $\boldsymbol{H}_1, \ldots, \boldsymbol{H}_n$ and circuit parameters $R_0, \ldots, R_n$, $L_1, \ldots, L_n$.

Initialisation :$R_0 = 1/(\boldsymbol{E}_0, \sigma \boldsymbol{E}_0)_\Omega$.

1: **for** $i = 1$ to n **do**
2: Solve $\nabla \times \widetilde{\boldsymbol{H}}_i = R_{n-1}\sigma \boldsymbol{E}_{n-1}$,
3: $\boldsymbol{H}_i = \boldsymbol{H}_{i-1} + \widetilde{\boldsymbol{H}}_i$,
4: $L_n = (\boldsymbol{H}_i, \mu \boldsymbol{H}_i)_\Omega$,
5: Solve $\nabla \times \widetilde{\boldsymbol{E}}_i = -\mu \boldsymbol{H}_i / L_n$,
6: $\boldsymbol{E}_i = \boldsymbol{E}_{i-1} + \widetilde{\boldsymbol{E}}_i$,
7: $R_i = 1/(\boldsymbol{E}_i, \sigma \boldsymbol{E}_i)_\Omega$,
8: **end for**
9: **return** $\boldsymbol{E}_0, \ldots, \boldsymbol{E}_n$, $\boldsymbol{H}_1, \ldots, \boldsymbol{H}_n$,$R_0, \ldots, R_n$, $L_1, \ldots, L_n$.

where $E(\Omega)$ is the set of the edge indices in Ω. From the Faraday's law (2.37), the electric field is obtained by

$$\begin{aligned} \boldsymbol{E} &= -\frac{\partial \boldsymbol{A}}{\partial t} \\ &\approx -\sum_{i \in E(\Omega)} \frac{\partial a_i}{\partial t} \boldsymbol{w}_i^e. \end{aligned} \tag{3.77}$$

Note that the scalar potential ϕ does not appear in the electric field because we use the A method here. Also orthogonal functions $\boldsymbol{H}_i = \mu \nabla \times \boldsymbol{A}_i$ and $\boldsymbol{E}_i$ are approximated using the edge element $\boldsymbol{w}_i^e$.

$$\boldsymbol{H}_n = \sum_{i \in E(\Omega)} a_{in} \nabla \times \boldsymbol{w}_i^e, \quad n = 1, 2, \ldots \tag{3.78}$$

$$\boldsymbol{E}_n = \sum_{i \in E(\Omega)} v_{in} \boldsymbol{w}_i^e, \quad n = 1, 2, \ldots \tag{3.79}$$

where a_{in}, v_{in} are the line integrals of the n-th functions $\boldsymbol{A}_n, \boldsymbol{E}_n$ along the edge i. Therefore, the orthogonal function expansion should be in the following form

$$\boldsymbol{H} \approx \mu \sum_{i \in E(\Omega)} \nabla \times \boldsymbol{w}_i^e \sum_{n=1}^{\infty} h_n(t) a_{in}, \tag{3.80}$$

$$\boldsymbol{E} \approx e_0(t) \boldsymbol{E}_0 + \sum_{i \in E(\Omega)} \boldsymbol{w}_i^e \sum_{n=1}^{\infty} e_n(t) v_{in} \tag{3.81}$$

where it holds that $\boldsymbol{E}_0 = -\nabla\phi_0$. Since the space spanned by edge elements contains the space spanned by node interpolation function, we can find $\boldsymbol{v}_0$ such that it holds $\sum v_{i0}\boldsymbol{w}_i^e = -\nabla\phi_0$. Therefore, we have

$$\boldsymbol{E} \approx \sum_{i\in E(\Omega)} \boldsymbol{w}_i^e \sum_{n=0}^{\infty} e_n(t) v_{in}. \tag{3.82}$$

The orthogonal functions must satisfy the following relation to make the Cauer circuit:

$$\begin{aligned}(\boldsymbol{H}_m, \mu\boldsymbol{H}_n)_\Omega &= \int_\Omega \boldsymbol{H}_m \cdot \mu\boldsymbol{H}_n d\Omega \\ &= \sum_{i,j\in E(\Omega)} \int_\Omega \nabla\times\boldsymbol{w}_i^e \cdot \mu\nabla\times\boldsymbol{w}_j^e d\Omega a_{im}a_{jn} \\ &= \boldsymbol{a}_m^\top K \boldsymbol{a}_n \\ &= L_n\delta_{mn}, \quad m,n = 1,2,\ldots,\end{aligned} \tag{3.83}$$

$$\begin{aligned}(\boldsymbol{E}_m, \sigma\boldsymbol{E}_n)_{\Omega_c} &= \int_{\Omega_c} \boldsymbol{E}_m \cdot \sigma\boldsymbol{E}_n d\Omega \\ &= \sum_{i,j\in E(\Omega_c)} \int_{\Omega_c} \boldsymbol{w}_i^e \cdot \sigma\boldsymbol{w}_j^e d\Omega v_{in}v_{jm} \\ &= \boldsymbol{v}_m^\top N \boldsymbol{v}_n \\ &= \frac{1}{R_n}\delta_{mn}, \quad m,n = 1,2,\ldots,\end{aligned} \tag{3.84}$$

where δ_{mn} is Kronecker's delta, $\boldsymbol{a}_n = [a_{1n}\ldots a_{Nn}]^\top, \boldsymbol{v}_n = [v_{1n}\ldots v_{Nn}]^\top$, and $K, N \in \mathbb{R}^{N\times N}$ correspond to the finite element matrices. Due to the nature of the edge elements, K, N are positive-semidefinite symmetric matrices and thus have zero eigenvalues. As already discussed in Section 3.1.4, the bilinear forms $\boldsymbol{x}^\top K\boldsymbol{y}, \boldsymbol{x}^\top N\boldsymbol{y}$ are the generalization of the inner products. Using these notations, all the equations in Algorithm 5 are discretized by FEM, shown in Algorithm 6. As a result, we obtain the K-orthogonal vectors $\boldsymbol{a}_1,\ldots,\boldsymbol{a}_n$ and N-orthogonal vectors $\boldsymbol{v}_0, \boldsymbol{v}_1, \ldots, \boldsymbol{v}_n$, and the circuit parameters of the Cauer circuit.

Algorithm 6 discrete CLN method

Input: electric field $\boldsymbol{E}_0 = \sum v_{i0}\boldsymbol{w}_i^e$ that satisfies $\nabla \times \boldsymbol{E}_0 = 0$ with 1 V power supply, iteration step n.

Output: orthogonal vectors $\boldsymbol{v}_0, \boldsymbol{v}_1, \ldots, \boldsymbol{v}_n$, $\boldsymbol{a}_1, \ldots, \boldsymbol{a}_n$ and circuit parameters $R_0, \ldots, R_n$, $L_1, \ldots, L_n$.

Initialisation :$R_0 = 1/\boldsymbol{v}_0^\top N \boldsymbol{v}_0, \boldsymbol{a}_0 = \boldsymbol{0}$.

1: **for** $i = 1$ to n **do**
2: Solve $K\widetilde{\boldsymbol{a}}_i = R_{i-1} N \boldsymbol{v}_{n-1}$,
3: $\boldsymbol{a}_i = \boldsymbol{a}_{i-1} + \widetilde{\boldsymbol{a}}_i$,
4: $L_i = \boldsymbol{a}_i^\top K \boldsymbol{a}_i$,
5: $\widetilde{\boldsymbol{v}}_i = -\boldsymbol{a}_i / L_i$
6: $\boldsymbol{v}_i = \boldsymbol{v}_{i-1} + \widetilde{\boldsymbol{v}}_i$,
7: $R_i = 1/\boldsymbol{v}_i^\top N \boldsymbol{v}_i$,
8: **end for**
9: **return** $\boldsymbol{v}_0, \boldsymbol{v}_1, \ldots, \boldsymbol{v}_n$, $\boldsymbol{a}_1, \ldots, \boldsymbol{a}_n$, $R_0, \ldots, R_n$, $L_1, \ldots, L_n$.

3.2.5 Relation to Padé approximation

We can express the impedance of the Cauer II form Z_d in the form of the continued fraction as follows:

$$\begin{aligned} Z_n &= \frac{I(s)}{V(s)} \\ &= R_0 + \cfrac{1}{\cfrac{1}{sL_1} + \cfrac{1}{R_1 + \cfrac{1}{\cfrac{1}{sL_2} + \cfrac{\ddots}{\cfrac{1}{sL_n} + \cfrac{1}{R_n}}}}} \\ &= \left[R_0; \tfrac{1}{sL_1}, R_1, \tfrac{1}{sL_2}, \cdots, \tfrac{1}{sL_n}, R_n\right]. \end{aligned} \tag{3.85}$$

Since the continued fraction is obtained by applying the Euclidean algorithm to a rational function, we deduce that the reduced-order model obtained by the CLN method is related to the Padé approximation. To clarify the relations between the CLN method and Padé approximation, we consider the the three-term recurrence relations obtained from the discrete CLN algorithm.

From the discrete CLN algorithm we immediately find the following recurrence rela-

tions.

$$\begin{aligned}\boldsymbol{a}_i &= \boldsymbol{a}_{i-1} - R_{i-1}A\boldsymbol{v}_{i-1}, \\ &= -\sum_{j=1}^{i} R_{j-1}A\boldsymbol{v}_{j-1} \quad i = 1, 2, \ldots, n, \end{aligned} \tag{3.86}$$

$$\begin{aligned}\boldsymbol{v}_i &= \boldsymbol{v}_{i-1} - \boldsymbol{a}_i/L_i, \\ &= \boldsymbol{v}_0 - \sum_{j=1}^{i} \boldsymbol{a}_j/L_j, \quad i = 1, 2, \ldots, n \end{aligned} \tag{3.87}$$

where $A = -K^{-1}N$. We find that the vectors $\boldsymbol{a}_i, \boldsymbol{v}_i$ are the elements of the Krylov subspace $\mathcal{K}_i(A, \boldsymbol{v}_0)$. This shows that the CLN method has relations to the Krylov subspace methods. We can examine the relationship in more detail by deriving the three-term recurrence relations. Dividing both sides of (3.86) by R_{i-1} and subtracting it for $i = n+1$ from that $i = n$ results in

$$\frac{1}{R_n}(\boldsymbol{a}_{n+1} - \boldsymbol{a}_n) - \frac{1}{R_{n-1}}(\boldsymbol{a}_n - \boldsymbol{a}_{n-1}) = -A(\boldsymbol{v}_n - \boldsymbol{v}_{n-1}). \tag{3.88}$$

Eliminating $\boldsymbol{v}_n - \boldsymbol{v}_{n-1}$ by substituting (3.87) into the right-hand side, we have

$$\begin{aligned}\frac{1}{R_n}(\boldsymbol{a}_{n+1} - \boldsymbol{a}_n) - \frac{1}{R_{n-1}}(\boldsymbol{a}_n - \boldsymbol{a}_{n-1}) &= \frac{1}{L_{2n-1}}A\boldsymbol{a}_n, \\ A\boldsymbol{a}_n = \frac{L_n}{R_n}\boldsymbol{a}_{n+1} - L_n\left(\frac{1}{R_n} + \frac{1}{R_{n-1}}\right)\boldsymbol{a}_n - \frac{L_n}{R_{n-1}}\boldsymbol{a}_{n-1}.& \end{aligned} \tag{3.89}$$

Similarly, we have

$$A\boldsymbol{v}_n = \frac{L_{n+1}}{R_n}\boldsymbol{v}_{n+1} - \frac{1}{R_n}(L_{n+1} + L_n)\boldsymbol{v}_n + \frac{L_n}{R_n}\boldsymbol{v}_{n-1}. \tag{3.90}$$

Recall that $\boldsymbol{a}_1, \ldots, \boldsymbol{a}_n$ and $\boldsymbol{e}_0, \ldots, \boldsymbol{e}_n$ are K- and N-orthogonal vectors which are not the Euclidean inner products. In addition $A = -K^{-1}N$ is non-Hermitian matrix. These are contrary to the requirements of the Hermitian or non-Hermitian Lanczos algorithms. The key to this is a property of the matrix A. In fact, A is a self-adjoint matrix with respect to

K and N inner products. Specifically, the following relation holds for A and $\forall \boldsymbol{x}, \boldsymbol{y} \in \mathbb{C}$.

$$\begin{aligned}(A\boldsymbol{x}, \boldsymbol{y})_K &= \boldsymbol{y}^\dagger K A \boldsymbol{x} \\ &= -\boldsymbol{y}^\dagger K K^{-1} N \boldsymbol{x} \\ &= -\boldsymbol{y}^\dagger N \boldsymbol{x} \\ &= -\boldsymbol{y}^\dagger N K^{-1} K \boldsymbol{x} \\ &= \boldsymbol{y}^\dagger A^* K \boldsymbol{x} \\ &= (\boldsymbol{x}, A\boldsymbol{y})_K, \end{aligned} \tag{3.91}$$

$$\begin{aligned}(A\boldsymbol{x}, \boldsymbol{y})_N &= \boldsymbol{y}^\dagger N A \boldsymbol{x} \\ &= -\boldsymbol{y}^\dagger N K^{-1} N \boldsymbol{x} \\ &= \boldsymbol{y}^\dagger A^* N \boldsymbol{x} \\ &= (\boldsymbol{x}, A\boldsymbol{y})_N. \end{aligned} \tag{3.92}$$

Note that K, N are the symmetric positive semi-definite matrices. What this shows is that the CLN method is based on the self-adjoint Lanczos algorithm. Therefore, we infer that the continued fraction is obtained by the Lanczos Padé connection. We will demonstrate in the next section how the continued fraction is obtained as a Padé approximation via self-adjoint Lanczos algorithm. The relation between the symmetric version of PVL (SyPVL) and the CVL method is discussed.

3.3 Cauer circuit via Lanczos algorithm

3.3.1 Cauer circuit via self-adjoint Lanczos algorithm

What are the differences between the discrete CLN and PVL? One of them is the use of different Lanczos algorithms: non-Hermitian Lanczos and self-adjoint Lanczos algorithms. There are other differences in the normalization conditions. As a result, the discrete CLN method generates the Cauer II form for the reduced-order model while the PVL method generates the Padé approximation. According to the author's knowledge, there has been no method that can directly obtain the Cauer II form as a reduced-order model from a given transfer function. Of course, we can obtain the Cauer circuit from the rational functions by using the Euclidean algorithm. Specifically, the Cauer II form can be obtained from the Padé approximation of a transfer function by using the similarity transformation [27]. But we would like to discuss why the CLN enables us to obtain the Cauer II form directly. The bottom line is that normalization conditions are significant for getting the Cauer circuit as a reduced-order model. In this part, we derive the Cauer circuit via Lanczos (CVL) algorithm to obtain the Cauer II form directly from a given transfer function.

Firstly, we derive the polynomial form of the three-term recurrence relations (3.89), (3.90). Let be $\boldsymbol{a}_n = U_{n-1}(A)\boldsymbol{v}_0, \boldsymbol{v}_{n-1} = V_{n-1}(A)\boldsymbol{v}_0$ where $U_{n-1}(\lambda), V_{n-1}(\lambda)$ are the

polynomials of exact degree $n-1$, we have

$$\lambda U_{n-1}(\lambda) = \frac{L_n}{R_n}U_n(\lambda) - L_n\left(\frac{1}{R_n}+\frac{1}{R_{n-1}}\right)U_{n-1}(\lambda) + \frac{L_n}{R_{n-1}}U_{n-2}(\lambda), \tag{3.93}$$

$$\lambda V_{n-1}(\lambda) = \frac{L_{n+1}}{R_n}V_n(\lambda) - \frac{1}{R_n}(L_{n+1}+L_n)V_{n-1}(\lambda) + \frac{L_n}{R_n}V_{n-2}(\lambda). \tag{3.94}$$

Recall that from (3.86), (3.87), we find that the normalization conditions are

$$V_n(0) = 1, \quad n = 0, 1, \ldots \tag{3.95a}$$

$$\left.\frac{U_n(\lambda)}{\lambda}\right|_{\lambda=0} = -\sum_{j=1}^{i} R_{j-1} \quad n = 1, 2, \ldots \tag{3.95b}$$

which are different from those in the PVL method. We emphasize that the this normalization conditions are essential to derive the continued fraction from a given transfer function. These kinds of normalization condition are sometimes used in the methods of iterative solvers such as CG method [86], but these have not been used in the context of the model order reductions. In the next, we derive a continued fraction from a given transfer function $H(s)$ only by using the normalization condition (3.95) and self-adjoint Lanczos algorithm.

Let us consider a linear time-invariant system:

$$(K + sN)\boldsymbol{x} = \boldsymbol{b}U(s), \tag{3.96a}$$

$$Y(s) = \boldsymbol{b}^\top \boldsymbol{x} \tag{3.96b}$$

where $K, N \in \mathbb{R}^{N\times N}$ are the symmetric positive definite matrices, and $\boldsymbol{b} \in \mathbb{R}^N, \boldsymbol{x} \in \mathbb{C}^N$. When the matrices are not positive definite, the algorithm may breakdown like non-Hermitian Lanczos. In this case, the look-ahead version of the Lanczos algorithm can effectively be used to avoid the breakdown. We assume that K is non-singular matrix. Note that we do not restrict ourself to the FE equations of the MQS approximation of Maxwell's equations but we consider more general equations. The transfer function is of the form

$$\begin{aligned}\mathcal{H}(s) &= \frac{Y(s)}{U(s)} \\ &= \boldsymbol{b}^\top (K+sN)^{-1}\boldsymbol{b} \\ &= \boldsymbol{b}^\top (I-sA)^{-1}K^{-1}\boldsymbol{b}\end{aligned} \tag{3.97}$$

where $A = -K^{-1}N$ is the self-adjoint matrix with respect to K and N. We consider the

Taylor expansion around $s = 0$ as follows:

$$\begin{aligned}\mathcal{H}(s) &= \sum_{i=0}^{\infty} \boldsymbol{b}^\top A^i K^{-1} \boldsymbol{b} s^i \\ &= \sum_{i=0}^{\infty} m_i s^i \end{aligned} \tag{3.98}$$

where $m_i = \boldsymbol{b}^\top A^i K^{-1} \boldsymbol{b}, i = 0, 1, \ldots$ are the moments.

Setting the initial vector $\boldsymbol{u} = K^{-1}\boldsymbol{b}$, we can construct the set of the orthogonal vectors $\boldsymbol{u}_1, \boldsymbol{u}_2, \ldots, \boldsymbol{u}_d$ in $\mathcal{K}_n(A, K^{-1}\boldsymbol{b})$ by the self-adjoint Lanczos algorithm with respect to K inner product, i.e., the orthogonal vectors are K-orthogonal each other. Note that the maximum number of the orthogonal vectors are determined by the grade of $\boldsymbol{u}$ with respect to $A = -K^{-1}N$. In Algorithm 4, the orthonormal condition ($|\boldsymbol{u}_i|_K = 1, i = 1, 2, \ldots, d$) is imposed on the orthogonal vectors. However, we here suppose the normalization condition $U_i(0) = 1, i = 0, 1, \ldots, d-1$ which is the essential to obtain the Cauer II form. The three term recurrence relation would be of the form

$$A\boldsymbol{u}_n = \xi_{n+1}\boldsymbol{u}_{n+1} - (\xi_{n+1} + \zeta_n)\boldsymbol{u}_n + \zeta_n \boldsymbol{u}_{n-1}, \quad n = 1, 2, \ldots, d. \tag{3.99}$$

where

$$(\boldsymbol{u}_i, \boldsymbol{u}_j)_K = \delta_{ij}\kappa_{2i-1}, \quad i, j = 1, 2, \ldots, d. \tag{3.100}$$

The matrix form would be

$$AU_n = U_n T_n + \xi_{n+1}\boldsymbol{u}_{n+1}\boldsymbol{e}_n^\top, \quad n = 1, 2, \ldots, d. \tag{3.101}$$

where $U_n = [\boldsymbol{u}_1, \boldsymbol{u}_2, \ldots, \boldsymbol{u}_n]$ and

$$T_n = \begin{bmatrix} -\xi_2 & \zeta_2 & & & & 0 \\ \xi_2 & -\xi_3 - \zeta_2 & \zeta_3 & & & \\ & \ddots & \ddots & \ddots & & \\ & & \xi_{n-1} & -\xi_n - \zeta_{n-1} & \zeta_n & \\ 0 & & & \xi_n & -\xi_{n+1} - \zeta_n \end{bmatrix}. \tag{3.102}$$

Note that $\xi_{d+1} = 0$. The coefficients ξ_n, ζ_n in the three-term recurrence relation (3.99) are computed as

$$(\boldsymbol{u}_{n+1}, A\boldsymbol{u}_n)_K = \xi_{n+1}\kappa_{2n+1}, \tag{3.103}$$

$$(\boldsymbol{u}_n, A\boldsymbol{u}_{n+1})_K = \zeta_{n+1}\kappa_{2n-1} \tag{3.104}$$

Due to the self-adjoint property of A with respect to K, the left-hand sides of these equations are equivalent. We can find coefficients $\kappa_{2n}, n = 1, 2, \ldots$ such that

$$\frac{\zeta_{n+1}}{\kappa_{2n+1}} = \frac{\xi_{n+1}}{\kappa_{2n-1}} = \kappa_{2n}, \quad n = 1, 2, \ldots, d. \tag{3.105}$$

Therefore, it holds that

$$A\boldsymbol{u}_n = \kappa_{2n}\kappa_{2n-1}\boldsymbol{u}_{n+1} - \kappa_{2n-1}(\kappa_{2n}+\kappa_{2n-2})\boldsymbol{u}_n + \kappa_{2n-1}\kappa_{2n-2}\boldsymbol{u}_{n-1}, \quad n = 1, 2, \ldots, d, \tag{3.106}$$

and

$$T_n = \begin{bmatrix} -\kappa_1\kappa_2 & \kappa_3\kappa_2 & & & 0 \\ \kappa_1\kappa_2 & -\kappa_3(\kappa_2+\kappa_4) & \ddots & & \\ & \ddots & \ddots & & \\ & & -\kappa_{2n-3}(\kappa_{2n-4}+\kappa_{2n-2}) & \kappa_{2n-1}\kappa_{2n-2} & \\ 0 & & \kappa_{2n-3}\kappa_{2n-2} & -\kappa_{2n-1}(\kappa_{2n-2}+\kappa_{2n}) & \end{bmatrix}. \tag{3.107}$$

Using the matrix form, we have

$$U_n^\top KAU_n = U_n^\top KU_nT_n = D_eT_n, \tag{3.108}$$

$$U_n^\top A^\top KU_n = U_n^\top KAU_n = T_n^\top U_n^\top KU_n = T_n^\top D_e \tag{3.109}$$

where $D_e = \mathrm{diag}[\kappa_1, \kappa_3, \cdots, \kappa_{2n-1}]$. Therefore, we obtain

$$D_eT_n = T_n^\top D_e. \tag{3.110}$$

Then, the $2i$-th moments ($i = 0, 1, \ldots, n-1$) can be computed as

$$\begin{aligned} m_{2i} &= \boldsymbol{b}^\top A^{2i}K^{-1}\boldsymbol{b} \\ &= \boldsymbol{u}_0^\top KA^{2i}\boldsymbol{u}_0 \\ &= \boldsymbol{e}_1^\top U_n^\top (A^\top)^i KA^iU_n\boldsymbol{e}_1 \\ &= (A^iU_n\boldsymbol{e}_1)^\top KA^iU_n\boldsymbol{e}_1 \\ &= (U_nT_n^i\boldsymbol{e}_1)^\top KU_nT_n^i\boldsymbol{e}_1 \\ &= \boldsymbol{e}_1^\top (T_n^\top)^i D_eT_n^i\boldsymbol{e}_1 \\ &= \boldsymbol{e}_1D_eT_n^{2i}\boldsymbol{e}_1 \\ &= \kappa_1\boldsymbol{e}_1^\top T_n^{2n}\boldsymbol{e}_1. \end{aligned}$$

The $2i+1$-th moments ($i = 0, 1, \ldots, n-1$) can also be computed by the same procedure. The partial realization of the transfer function becomes

$$\begin{aligned} \mathcal{H}(s) &\approx \mathcal{H}_n(s) \\ &= \sum_{i=0}^{2n} m_i s^i \\ &= \kappa_1 \sum_{i=0}^{2n} \boldsymbol{e}_1^\top T_n^{2i}\boldsymbol{e}_1 s^i \\ &= \kappa_1 \boldsymbol{e}_1^\top (I - sT_n)^{-1}\boldsymbol{e}_1. \end{aligned} \tag{3.111}$$

Using equation (3.107), we can express the Padé approximation $\mathcal{H}_n(s)$ as a continued fraction. For details on this calculation, see Appendix A. As a result, we have the continued fraction as the reduced-order model of the given transfer function.

$$\begin{aligned}\mathcal{H}_n(s) &= \cfrac{1}{\cfrac{1}{\kappa_1}+\cfrac{1}{\cfrac{1}{s\kappa_2}+\cfrac{1}{\cfrac{1}{\kappa_3}+\cfrac{\ddots}{\cfrac{1}{\kappa_{2n-1}}+\cfrac{1}{\cfrac{1}{s\kappa_{2n}}}}}}}} \\ &= \left[0; \tfrac{1}{\kappa_1}, \tfrac{1}{s\kappa_2}, \tfrac{1}{\kappa_3}, \cdots, \tfrac{1}{\kappa_{2n-1}}, \tfrac{1}{s\kappa_{2n}}\right]. \end{aligned} \tag{3.112}$$

As is well known, the impedance or admittance of a Cauer circuit can be expressed as a continued fractions. Equation (3.112) can be seen as the admittance of a Cauer circuit shown in Fig. 3.9. Therefore, we can interpret the reduce-order model represented by a continued fraction as a Cauer circuit. Multiplying (3.112) by s results in

$$\begin{aligned}s\mathcal{H}_n(s) &= \cfrac{1}{\cfrac{1}{s\kappa_1}+\cfrac{1}{\cfrac{1}{\kappa_2}+\cfrac{1}{\cfrac{1}{s\kappa_3}+\cfrac{\ddots}{\cfrac{1}{s\kappa_{2n-1}}+\cfrac{1}{\cfrac{1}{\kappa_{2n}}}}}}}} \\ &= \left[0; \tfrac{1}{s\kappa_1}, \tfrac{1}{\kappa_2}, \tfrac{1}{s\kappa_3}, \cdots, \tfrac{1}{s\kappa_{2n-1}}, \tfrac{1}{\kappa_{2n}}\right]. \end{aligned} \tag{3.113}$$

which is equivalent to (3.54). The transfer function $s\mathcal{H}_n(s)$ can be seen as the impedance of the Cauer circuit shown in Fig. 3.11.

As in the case of PVL, it is possible to introduce an expansion point s_0 for the Taylor expansion. In this case, the continuous fraction is of the form

$$\begin{aligned}\mathcal{H}_n(\sigma) &= \cfrac{1}{\cfrac{1}{\kappa_1}+\cfrac{1}{\cfrac{1}{\sigma\kappa_2}+\cfrac{1}{\cfrac{1}{\kappa_3}+\cfrac{\ddots}{\cfrac{1}{\kappa_{2n-1}}+\cfrac{1}{\cfrac{1}{\sigma\kappa_{2n}}}}}}}} \\ &= \left[0; \tfrac{1}{\kappa_1}, \tfrac{1}{\sigma\kappa_2}, \tfrac{1}{\kappa_3}, \cdots, \tfrac{1}{\kappa_{2n-1}}, \tfrac{1}{\sigma\kappa_{2n}}\right] \end{aligned} \tag{3.114}$$

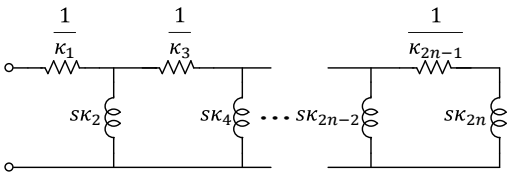

Figure3.9: Cauer II form corresponding to the continued fraction $Y = \mathcal{H}_n(s)$.

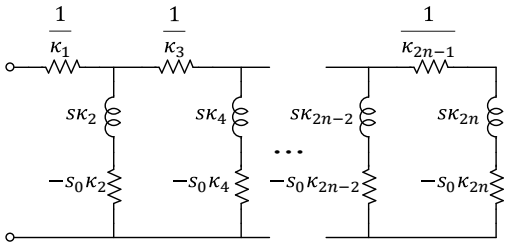

Figure3.10: Cauer II form corresponding to the continued fraction $Y = \mathcal{H}_n(\sigma)$.

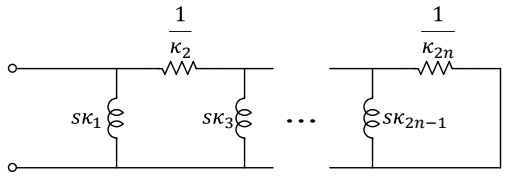

Figure3.11: Cauer II form corresponding to the continued fraction $Z = s\mathcal{H}_n(s)$.

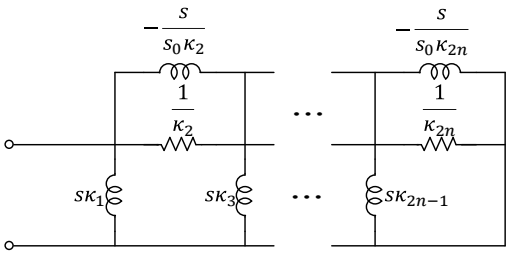

Figure3.12: Cauer II form corresponding to the continued fraction $Z = s\mathcal{H}_n(\sigma)$.

where $\sigma = s - s_0$. The Cauer circuit is shown in Fig. 3.10. In this case, the circuit includes the negative resistances. Multiplying (3.114) by s, we obtain

$$
\begin{aligned}
s\mathcal{H}_n(\sigma) &= \cfrac{1}{\cfrac{1}{s\kappa_1} + \cfrac{1}{\cfrac{s}{\sigma\kappa_2} + \cfrac{1}{\cfrac{1}{s\kappa_3} + \cfrac{\ddots}{\cfrac{1}{s\kappa_{2n-1}} + \cfrac{1}{\cfrac{s}{\sigma\kappa_{2n}}}}}}}} \\
&= \left[0; \tfrac{1}{s\kappa_1}, \tfrac{s}{\sigma\kappa_2}, \tfrac{1}{s\kappa_3}, \cdots, \tfrac{1}{s\kappa_{2n-1}}, \tfrac{s}{\sigma\kappa_{2n}}\right]. \qquad (3.115)
\end{aligned}
$$

The circuit representation is shown in Fig. 3.12 which includes the negative inductors. The negative resistances and inductors are non-physical elements so that we cannot find physical meanings in the obtained Cauer circuit. However, there is possibility of improving the accuracy of the Padé approximation by introducing the expansion point s_0.

In the above formulation, we do not derive the two-term recurrence relations which correspond to (3.86), (3.87). To derive the two-term recurrence relations, we now introduce

new vectors $\boldsymbol{v}_1, \boldsymbol{v}_2, \dots$ such that

$$\boldsymbol{v}_n = V_{n-1}(A)\boldsymbol{u}_1, \tag{3.116}$$

$$V_{n-1}(\lambda) = \kappa_{2n}\frac{U_n(\lambda) - U_{n-1}(\lambda)}{\lambda}, \quad n = 1, 2, \dots, d. \tag{3.117}$$

where $V_{n-1}(\lambda)$ is the polynomial of exact degree $n-1$. Note that we define $V_{-1}(\lambda) = 0$. Then, we can prove the following proposition.

Proposition 3. It holds that

$$(\boldsymbol{u}_m, \boldsymbol{v}_n)_K = \begin{cases} 1, & m \le n \\ 0, & m > n \end{cases}, \tag{3.118}$$

$$(\boldsymbol{v}_m, \boldsymbol{v}_n)_N = \kappa_{2n}\delta_{mn}, \quad \text{for } m, n = 1, 2, \dots, d. \tag{3.119}$$

Proof. By substituting the definition of $V_n(\lambda)$ into the three-term recurrence relation (3.106), we obtain

$$\begin{aligned} \frac{1}{\kappa_{2n-1}}U_{n-1}(\lambda) &= \kappa_{2n}\frac{U_n(\lambda) - U_{n-1}(\lambda)}{\lambda} - \kappa_{2n-2}\frac{U_{n-1}(\lambda) - U_{n-2}(\lambda)}{\lambda} \\ &= V_{n-1}(\lambda) - V_{n-2}(\lambda), \quad n = 1, 2, \dots, d. \end{aligned} \tag{3.120}$$

This can be represented by the vector form as follows:

$$\begin{aligned} \boldsymbol{v}_n &= \boldsymbol{v}_{n-1} + \frac{1}{\kappa_{2n-1}}\boldsymbol{u}_n \\ &= \sum_{j=1}^{n}\frac{1}{\kappa_{2j-1}}\boldsymbol{u}_j, \quad n = 1, 2, \dots, d. \end{aligned} \tag{3.121}$$

Due to the K-orthogonality of $\boldsymbol{u}_m$, we have

$$\begin{aligned} (\boldsymbol{u}_m, \boldsymbol{v}_n)_K &= \sum_{j=1}^{n}\frac{1}{\kappa_{2j-1}}(\boldsymbol{u}_m, \boldsymbol{u}_j) \\ &= \sum_{j=1}^{n}\delta_{mj}. \end{aligned} \tag{3.122}$$

Therefore, we obtain 3.118. From the definition of $\boldsymbol{v}_n$, we have

$$(A\boldsymbol{v}_m, \boldsymbol{v}_n)_K = (\kappa_{2m}(\boldsymbol{u}_{m+1} - \boldsymbol{u}_m), \boldsymbol{v}_n)_K. \tag{3.123}$$

Using (3.118), we can see

$$(\kappa_{2m}(\boldsymbol{u}_{m+1} - \boldsymbol{u}_m), \boldsymbol{v}_n)_K = -\kappa_{2n}\delta_{mn} \tag{3.124}$$

Recall that $A = -K^{-1}N$, we have

$$\begin{aligned} (A\boldsymbol{v}_m, \boldsymbol{v}_n)_K &= -\boldsymbol{v}_m^\top NK^{-1}K\boldsymbol{v}_n = -\boldsymbol{v}_m^\top N\boldsymbol{v}_n \\ &= -(\boldsymbol{v}_m, \boldsymbol{v}_n)_N = -\kappa_{2n}\delta_{mn} \end{aligned} \tag{3.125}$$

□

Using the vectors $\boldsymbol{v}_1, \ldots, \boldsymbol{v}_n$, we can derive the two-term recurrence relations as follows:

$$\boldsymbol{v}_n = \boldsymbol{v}_{n-1} + \frac{1}{\kappa_{2n-1}}\boldsymbol{u}_n, \quad \text{where } \kappa_{2n-1} = (\boldsymbol{u}_n, \boldsymbol{u}_n)_K \tag{3.126}$$

$$\boldsymbol{u}_{n+1} = \boldsymbol{u}_n + \frac{1}{\kappa_{2n}}A\boldsymbol{v}_n, \quad \text{where } \kappa_{2n} = (\boldsymbol{v}_n, \boldsymbol{v}_n)_N \tag{3.127}$$

The algorithm to obtain the Cauer circuit is shown in Algorithm 7. When K, N are the positive definite matrices, the circuit parameter has the positive values because it holds that

$$(\boldsymbol{u}_n, \boldsymbol{u}_n)_K = \boldsymbol{u}_n^\top K \boldsymbol{u}_n = \kappa_{2n-1} > 0 \tag{3.128}$$

$$(\boldsymbol{v}_n, \boldsymbol{v}_n)_N = \boldsymbol{v}_n^\top N \boldsymbol{v}_n = \kappa_{2n} > 0. \tag{3.129}$$

From the results of the classical circuit theory, we conclude that the obtained reduced-order model is always passive. This result is consistent with the sufficient condition for the passivity given in [27].

Algorithm 7 Cauer circuit via self-adjoint Lanczos algorithm

Input: expansion point s_0, symmetric (positive definite) matrices $K, N \in \mathbb{R}^{N\times N}$, vector $\boldsymbol{b} \in \mathbb{R}^N$, $A = -(K + s_0 N)^{-1}N$. Let d be the grade of $(K + s_0 N)^{-1}\boldsymbol{b}$ with respect to A.

Output: K and N orthogonal vectors $\boldsymbol{u}_1, \ldots, \boldsymbol{u}_d$, $\boldsymbol{v}_1, \ldots, \boldsymbol{v}_d$ and parameters in the continued fraction expansion $\kappa_1, \ldots, \kappa_{2d}$.

Initialisation :$\boldsymbol{u}_1 = (K + s_0 N)^{-1}\boldsymbol{b}$, $(\boldsymbol{u}_1, \boldsymbol{u}_1)_K = \kappa_1, \boldsymbol{v}_0 = \boldsymbol{0}$.

1: **for** $i = 1$ to d **do**
2: $\quad \boldsymbol{v}_i = \boldsymbol{v}_{i-1} + \frac{1}{\kappa_{2i-1}}\boldsymbol{u}_i$,
3: $\quad \kappa_{2i} = (\boldsymbol{v}_i, \boldsymbol{v}_i)_N$,
4: $\quad \boldsymbol{u}_{i+1} = \boldsymbol{u}_i + \frac{1}{\kappa_{2i}}A\boldsymbol{v}_i$,
5: $\quad \kappa_{2n+1} = (\boldsymbol{u}_{i+1}, \boldsymbol{u}_{i+1})_{(K+s_0N)}$,
6: **end for**
7: **return** $\boldsymbol{u}_1, \ldots, \boldsymbol{u}_d$, $\boldsymbol{v}_1, \ldots, \boldsymbol{v}_d$, $\kappa_1, \ldots, \kappa_{2d}$.

The orthogonal vectors $\boldsymbol{u}_1, \ldots, \boldsymbol{u}_n$ can be used to approximate the solution of the full-order system. In other words, the solution of the original equation is projected onto the orthogonal vectors $\boldsymbol{u}_1, \ldots, \boldsymbol{u}_n$. This is so-called the Galerkin projection. In the following, we will show that the circuit equation of the Cauer circuit can be obtained by the Galerkin projection. Using the Galerkin projection, we can express the vector $\boldsymbol{x}$ by the linear

combination of the orthogonal basis vectors as follows:

$$\begin{aligned} \boldsymbol{x} &= \sum_{j=1}^{n} y_j \boldsymbol{u}_j \\ &= U\boldsymbol{y} \end{aligned} \tag{3.130}$$

where $\boldsymbol{y} = [y_1, \ldots, y_n]^\top$. Substituting it into the full-order system (3.96a), we have

$$(K + sN)U\boldsymbol{y} = KK^{-1}\boldsymbol{b}I(s) = KU\boldsymbol{e}_1 I(s). \tag{3.131}$$

Multiplying $U^\top$ from left side results in

$$(I - sT_n)\boldsymbol{y} = \boldsymbol{e}_1 I(s) \tag{3.132}$$

Applying the change of the variables $\boldsymbol{y} = D_n^{-1}\boldsymbol{z}$ in the equation yields

$$(D_n^{-1} - sT_n D_n^{-1})\boldsymbol{z} = \boldsymbol{e}_1 I(s) \tag{3.133}$$

where

$$T_n D_n^{-1} = \begin{bmatrix} -\kappa_2 & \kappa_2 & & & 0 \\ \kappa_2 & -(\kappa_2+\kappa_4) & \ddots & & \\ & \ddots & \ddots & & \\ & & -(\kappa_{2n-4}+\kappa_{2n-2}) & \kappa_{2n-2} & \\ 0 & & \kappa_{2n-2} & -(\kappa_{2n-2}+\kappa_{2n}) \end{bmatrix}. \tag{3.134}$$

This is equivalent to the circuit equation of the Cauer circuit as shown in Fig. 3.13. We find that $y_i, i = 1, \ldots, n$ are the voltage drop by the resisters $1/\kappa_{2i-1}$, and $z_i, i = 1, \ldots, n$ are the loop current in the circuit.

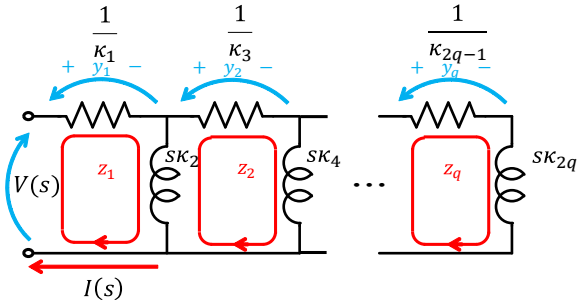

Figure3.13: Cauer circuit and unknown variables

3.3.2 Remark

In [27], the SyPVL algorithm has been proposed, which is the symmetric version of the PVL algorithm. The SyPVL algorithm reduces the computational cost by exploiting the

symmetry from the non-Hermitian Lanczos algorithm. Mathematically, the exploitation of the symmetry is equivalent to the use of the self-adjoint property of the matrix $A = -K^{-1}N$. Therefore, the CLN method and its discretized version are essentially same as the SyPVL nevertheless the algorithm looks different. It means that the CLN method and its discretized version does not contribute to the improvement of the accuracy than the SyPVL. Unlike the SyPVL method, however, the proposed method can generate the Cauer II form without the similarity transformation. Note again that the difference is due to the normalization condition of the orthogonal vectors in the Lanczos algorithm.

3.3.3 Application to Maxwell's equations

MQS approximation of Maxwell's equations with A method

Let us consider the eddy current problem in Section 3.2 again. The complex phasor notation of the MQS approximation of Maxwell's equations with A method is given by

$$\nabla \times \nu \nabla \times \boldsymbol{A} + s\sigma \boldsymbol{A} = \boldsymbol{j}_0 I(s). \tag{3.135}$$

where $s = \mathrm{j}\omega$, $I(s)$ is the input current and $\boldsymbol{j}_0$ is the current density when the unit current flow in the conductor. We consider the Dirichlet and homogeneous Neumann boundary conditions.

$$\boldsymbol{A} \times \boldsymbol{n} = \boldsymbol{0}, \quad \text{on } \Gamma_{\mathrm{D}} \cup \Gamma_{\mathrm{PEC}}, \tag{3.136}$$

$$(\nu \nabla \times \boldsymbol{A}) \times \boldsymbol{n} = \boldsymbol{0}, \quad \text{on } \Gamma_{\mathrm{N}}. \tag{3.137}$$

Since the terminal voltage $V(s)$ is obtained by the time differential of the interlinkage magnetic flux Φ, we can write it as

$$V(s) = s \int_{\Omega_{\mathrm{c}}} \boldsymbol{A} \cdot \boldsymbol{j}_0 I(s) d\Omega. \tag{3.138}$$

Using the FE discretization, we obtain the following FE equations.

$$(K + sN)\boldsymbol{x} = \boldsymbol{b} I(s), \tag{3.139}$$

$$V(s) = s\boldsymbol{b}^{\top} \boldsymbol{x} \tag{3.140}$$

where $K, N \in \mathbb{R}^{N \times N}$ are the non-singular symmetric positive semi-definite matrices, $\boldsymbol{b} \in \mathbb{R}^{N \times N}$. The Dirichlet boundary condition is already applied to the equations. As explained in Section 2.8, we can maintain the symmetry of the FE matrices even after applying the Dirichlet boundary condition. Therefore, the impedance of the system can be written as

$$Z(s) = R_0 + s\boldsymbol{b}^{\top}(K + sN)^{-1}\boldsymbol{b} \tag{3.141}$$

where R_0 is direct-current (DC) resistance of the conductor which can be obtained by

$$R_0 = \int_{\Omega_{\mathrm{c}}} \frac{|\boldsymbol{j}_0|^2}{\sigma} d\Omega. \tag{3.142}$$

Recall that K must be non-singular when applying Algorithm 7 in order to take the inverse of K. A problem arises when we use the edge elements to obtain the FE equations because K becomes a singular matrix. Although we can solve the equation $K\boldsymbol{x} = \boldsymbol{y}$ by the iterative methods, there remains undetermined gradient components such that $K\boldsymbol{z} = 0$ which correspond to the null-space of K. The component $\boldsymbol{z}$ would affect the computation of the circuit parameters $\kappa_{2i}, i = 1, 2, \ldots, d$ because $(\boldsymbol{v}_i, \boldsymbol{v}_i)_N = (\boldsymbol{x} + \boldsymbol{z}, \boldsymbol{x} + \boldsymbol{z})_N$ can not be determined uniquely. Note that $\boldsymbol{z}$ does not affect the computation of $\kappa_{2i-1}, i = 1, 2, , \ldots, d$ because it holds that $(\boldsymbol{u}_i, \boldsymbol{u}_i) = (\boldsymbol{x} + \boldsymbol{z}, \boldsymbol{x} + \boldsymbol{z})_K = (\boldsymbol{x}, \boldsymbol{x})_K$. It means that the Cauer circuit is not determined uniquely without the gauge conditions. To avoid the problem, we have impose a gauge condition such as the tree-cotree gauge [84] on the FE equations to make the curl-curl matrix K non-singular. As already mentioned in Section 2.7, this kind of treatment results in the deterioration of ICCG convergence [85]. The other choice is to employ the $A - \phi$ method which is explained in the next part.

Using Algorithm 7, we immediately obtain

$$\begin{aligned} Z(s) &= R_0 + s\left[0; \tfrac{1}{\kappa_1}, \tfrac{1}{\sigma\kappa_2}, \tfrac{1}{\kappa_3}, \cdots, \tfrac{1}{\kappa_{2d-1}}, \tfrac{1}{\sigma\kappa_{2d}}\right] \\ &= R_0 + \left[0; \tfrac{1}{s\kappa_1}, \tfrac{1}{\kappa_2}, \tfrac{1}{s\kappa_3}, \cdots, \tfrac{1}{s\kappa_{2d-1}}, \tfrac{1}{\kappa_{2d}}\right] \\ &= \left[R_0; \tfrac{1}{sL_1}, R_1, \tfrac{1}{sL_2}, \cdots, \tfrac{1}{sL_d}, R_d\right] \end{aligned} \tag{3.143}$$

where $L_n = \kappa_{2n-1}, R_n = 1/\kappa_{2n}, n = 1, 2, \ldots, d$. The Cauer circuit is exactly the same as the one obtained in the CLN method shown in Fig. 3.8 and obtained in the continued fraction expansion of PRF shown in Fig. 3.4. Since the FE matrices K, N are positive semi-definite, we can ensure the circuit parameters are always non-negative.

MQS approximation of Maxwell's equations with $A - \phi$ method

The eddy current problems can also be formulated with $A - \phi$ method. The complex phasor notation of the MQS approximation of Maxwell's equations with $A - \phi$ method is given by

$$\nabla \times \nu\nabla \times \boldsymbol{A} + \sigma(\mathrm{j}\omega\boldsymbol{A} + \nabla\phi) = \boldsymbol{j}_0 I(s) \tag{3.144}$$

$$\nabla \cdot \sigma(\mathrm{j}\omega\boldsymbol{A} + \nabla\phi) = 0. \tag{3.145}$$

The second equation is the current continuous equation. The following boundary conditions are imposed on the unknown variables.

$$\boldsymbol{A} \times \boldsymbol{n} = \boldsymbol{0}, \quad \text{on } \Gamma_{\mathrm{D}} \cup \Gamma_{\mathrm{PEC}}, \tag{3.146}$$

$$(\nu\nabla \times \boldsymbol{A}) \times \boldsymbol{n} = \boldsymbol{0}, \quad \text{on } \Gamma_{\mathrm{N}} \tag{3.147}$$

$$\phi = 0, \quad \text{on } \Gamma_{\mathrm{PEC}}. \tag{3.148}$$

The voltage is given by

$$V = s \int_{\Omega_c} \boldsymbol{A} \cdot \boldsymbol{j}_0 d\Omega I(s). \tag{3.149}$$

Using the FE discretization, we obtain the following FE equations.

$$\left(\begin{bmatrix} K & L \\ O & M \end{bmatrix} + s \begin{bmatrix} N & O \\ L^\top & O \end{bmatrix} \right) \begin{bmatrix} \boldsymbol{a} \\ \boldsymbol{\phi} \end{bmatrix} = \begin{bmatrix} \boldsymbol{b} \\ \boldsymbol{0} \end{bmatrix} I(s), \tag{3.150}$$

$$V(s) = s \begin{bmatrix} \boldsymbol{b}^\top & \boldsymbol{0} \end{bmatrix} \begin{bmatrix} \boldsymbol{a} \\ \boldsymbol{\phi} \end{bmatrix} \tag{3.151}$$

To make the coefficient matrices symmetry, we transform the second equation:

$$\boldsymbol{\phi} = -sM^{-1}L^\top \boldsymbol{a}. \tag{3.152}$$

We can eliminate $\boldsymbol{\phi}$ from the equations as follows:

$$(K + s(N - LM^{-1}L^\top))\boldsymbol{a} = \boldsymbol{b}I(s). \tag{3.153}$$

The impedance of the system can be written as

$$Z(s) = R_0 + s\boldsymbol{b}^\top (K + s(N - LM^{-1}L^\top))^{-1}\boldsymbol{b}. \tag{3.154}$$

In this case, we do not have to impose the gauge condition on the curl-curl matrix K because the circuit parameters are determined uniquely. Let us consider the i-th iteration of Algorithm 7. The vectors $\boldsymbol{v}_i, \boldsymbol{u}_{i+1}$ have the undermined gradient component $\boldsymbol{z}_1, \boldsymbol{z}_2$ such that $K\boldsymbol{z}_1 = K\boldsymbol{z}_2 = \boldsymbol{0}$. Then, we can show κ_{2i} can be obtained uniquely.

$$(\boldsymbol{x} + \boldsymbol{z}_1, \boldsymbol{x} + \boldsymbol{z}_1)_{(N - LM^{-1}L^\top)} = (\boldsymbol{x}, \boldsymbol{x})_{(N - LM^{-1}L^\top)} + (\boldsymbol{x} + \boldsymbol{z}_1)^\top (N - LM^{-1}L^\top)\boldsymbol{z}_1. \tag{3.155}$$

Using the discrete gradient operator $[G]$, the undetermined gradient component can always be written as $\boldsymbol{z}_1 = [G]\boldsymbol{\phi}_1$. The second term of (3.155) becomes

$$\begin{aligned} (\boldsymbol{x} + \boldsymbol{z}_1)^\top (N - LM^{-1}L^\top)\boldsymbol{z}_1 &= (\boldsymbol{x} + \boldsymbol{z}_1)^\top ([\sigma] - [\sigma][G]M^{-1}[G]^\top [\sigma])[G]\boldsymbol{\phi}_1 \\ &= (\boldsymbol{x} + \boldsymbol{z}_1)^\top ([\sigma][G] - [\sigma][G]M^{-1}M)\boldsymbol{\phi}_1 \\ &= 0 \end{aligned} \tag{3.156}$$

where $N = [\sigma], L = [\sigma][G], M = [G]^\top [\sigma][G]$. Thus, it holds that

$$(\boldsymbol{x} + \boldsymbol{z}_1, \boldsymbol{x} + \boldsymbol{z}_1)_{(N - LM^{-1}L^\top)} = (\boldsymbol{x}, \boldsymbol{x})_{(N - LM^{-1}L^\top)} = \kappa_{2i}, \tag{3.157}$$

From this result, we can determine κ_{2i} uniquely. The uniqueness of κ_{2i+1} obeys from

$$(\boldsymbol{x} + \boldsymbol{z}_2, \boldsymbol{x} + \boldsymbol{z}_2)_K = (\boldsymbol{x}, \boldsymbol{x})_K + (\boldsymbol{x} + \boldsymbol{z}_2)^\top K\boldsymbol{z}_2 = (\boldsymbol{x}, \boldsymbol{x})_K. \tag{3.158}$$

Therefore, all the parameters of the Cauer circuit can be uniquely determined without imposing a gauge condition on the curl-curl matrix K.

By applying Algorithm 7 to the second term of (3.154), we obtain

$$\begin{aligned} Z(s) &= R_0 + s\left[0; \tfrac{1}{\kappa_1}, \tfrac{1}{\sigma\kappa_2}, \tfrac{1}{\kappa_3}, \cdots, \tfrac{1}{\kappa_{2d-1}}, \tfrac{1}{\sigma\kappa_{2d}}\right] \\ &= R_0 + \left[0; \tfrac{1}{s\kappa_1}, \tfrac{1}{\kappa_2}, \tfrac{1}{s\kappa_3}, \cdots, \tfrac{1}{s\kappa_{2d-1}}, \tfrac{1}{\kappa_{2d}}\right] \\ &= \left[R_0; \tfrac{1}{sL_1}, R_1, \tfrac{1}{sL_2}, \cdots, \tfrac{1}{sL_d}, R_d\right] \end{aligned} \tag{3.159}$$

where $L_n = \kappa_{2n-1}, R_n = 1/\kappa_{2n}, n = 1, 2, \ldots, d$. The $A - \phi$ method is effective when we use the edge elements to discretize Maxwell's equations.

3.3.4 Cauer circuit via Non-Hermitian Lanczos algorithm

In the previous part, we derive the Cauer II form from a given transfer function by using the self-adjoint Lanczos algorithm. Thanks to the self-adjoint property of the matrix $A = -K^{-1}N$ with respect to K, N, the required computational cost and storage are as half as those in the non-Hermitian Lanczos algorithm. However, when we consider a system with the non-Hermite matrices or different input and output vectors, we can no longer apply Algorithm 7 to the system. This is important when we consider the homogenization of Maxwell's equations and Darwin model of Mawell's equations which are in the case of this thesis. So, we consider the non-Hermitian version of the CVL method in this part. We will prove that this can also be obtained by changing the orthonormal condition to $U_n(0) = 1$.

We can express the sets of biorthogonal basis vectors $\boldsymbol{v}_1, \ldots, \boldsymbol{v}_n$ and $\boldsymbol{w}_1, \ldots, \boldsymbol{w}_n$ obtained by the non-Hermitian Lanczos algorithms 3 in the polynomial form as follows:

$$\boldsymbol{v}_i = V_{i-1}(A)\boldsymbol{v} \tag{3.160}$$

$$\boldsymbol{w}_i = W_{i-1}(A)\boldsymbol{w} \tag{3.161}$$

where $V_{i-1}(\lambda), W_{i-1}(\lambda)$ are the polynomial of exact degree $i-1$. In Algorithm 3, the vectors are normalized to 1 i.e., $|\boldsymbol{v}_i| = 1, (\boldsymbol{w}_i, \boldsymbol{v}_i) = 1$. If we do not employ the orthonormal condition, we can compute the biorthogonal vectors from the same polynomials. This can be written as follows:

Proposition 4. Let be $A \in \mathbb{F}^{N\times N}, \boldsymbol{u}_1, \boldsymbol{u}_1^\bullet \in \mathbb{F}^N$. The set of the biorthogonal vectors can be generated from the following three term recurrence relation:

$$\xi_{n+1}U_n(\lambda) = \lambda U_{n-1}(\lambda) - \eta_n U_{n-1}(\lambda) - \zeta_n U_{n-2}(\lambda), \quad n = 1, 2, \ldots, \tag{3.162}$$

where $U_n(\lambda)$ is the polynomial of exact degree n, $U_0(\lambda) = 1, U_{-1}(\lambda) = 0$, and $\xi_{n+1}, \eta_n, \zeta_n \in \mathbb{F}$. The biorthogonal vectors are generated by $\boldsymbol{u}_n = U_{n-1}(A)\boldsymbol{u}$, $\boldsymbol{u}_n^\bullet = \overline{U}_{n-1}(A^*)\boldsymbol{u}^\bullet, n = 1, 2, \ldots$. The biorthogonal condition can be written as

$$(\boldsymbol{u}_m, \boldsymbol{u}_n^\bullet) = \delta_{mn}\alpha_n. \tag{3.163}$$

Proof. The proof is done by considering the Gram-Schmidt orthogonalization of $U_n(\lambda), n = 1, 2, \ldots$. Let us consider the i-th step of the Gram-Schmidt orthogonalization. In general, the polynomial $\widetilde{U}_i(\lambda)$ of exact degree i can be represented by

$$\widetilde{U}_i(\lambda) = \lambda U_{i-1}(\lambda) - \sum_{j=1}^{i} h_{j,i} U_{j-1}(\lambda) \tag{3.164}$$

where $h_{j,i} \in \mathbb{F}$. Note that the orthogonality means

$$(U_m(A)\boldsymbol{u}_1, U_n(A^*)\boldsymbol{u}_1^\bullet) = (U_n(A)\boldsymbol{u}_1, U_m(A^*)\boldsymbol{u}_1^\bullet) = \delta_{mn}\alpha_{n+1}, \quad m, n = 0, 1, \ldots, i.$$

Note that the term $U_n(A)U_m(A)$ is commutative. Using the orthogonality of $U_i(\lambda)$, we can compute the coefficients $h_{j,i}$ as follows:

$$0 = (AU_{i-1}(A)\boldsymbol{u}_1, U_{j-1}(A^*)\boldsymbol{u}_1^\bullet) - h_{j,i}\alpha_j$$

When $j = i, i-1$, it holds that

$$h_{i,i} = (A\boldsymbol{u}_i, \boldsymbol{u}_i^\bullet)/\alpha_i, \tag{3.165}$$
$$h_{i-1,i} = (A\boldsymbol{u}_i, \boldsymbol{u}_{i-1}^\bullet)/\alpha_{i-1} = (\boldsymbol{u}_{i-1}, A^*\boldsymbol{u}_i^\bullet)/\alpha_{i-1}. \tag{3.166}$$

When $j - 2 \leq i$, we have

$$\begin{aligned}(AU_{i-1}(A)\boldsymbol{u}_1, U_{j-1}(A^*)\boldsymbol{u}_1^\bullet) &= (U_{i-1}(A)\boldsymbol{u}_1, A^*U_{j-1}(A^*)\boldsymbol{u}_1^\bullet) \\ &= 0\end{aligned} \tag{3.167}$$

because $\boldsymbol{u}_i \perp A^*U_{j-1}(A^*)\boldsymbol{u}_1^\bullet \in \mathcal{K}_{j+1}(A^*, \boldsymbol{u}_1^\bullet) \subset \mathcal{K}_{i-1}(A^*, \boldsymbol{u}_1^\bullet)$. Therefore, we have

$$h_{j,i} = 0, \quad j \leq i - 2. \tag{3.168}$$

□

This means that the vectors $\boldsymbol{v}_i, \boldsymbol{w}_i$ are generated from the same polynomial in the non-Hermitian Lanczos algorithm. The reason they appear different is that each vector is normalized in a different way. If we employ the normalization condition $U_i(0) = 1, i = 0, 1, \ldots$, we can write the matrix form of the non-Hermitian Lanczos algorithm as follows:

$$AU_n = U_n T_n + \kappa_{2n}\kappa_{2n-1}\boldsymbol{u}_{n+1}\boldsymbol{e}_{n+1}^\top, \tag{3.169}$$
$$A^*U_n^\bullet = U_n^\bullet T_n^* + \kappa_{2n}^*\kappa_{2n-1}^*\boldsymbol{u}_{n+1}^\bullet\boldsymbol{e}_n^\top, \tag{3.170}$$
$$U_n^{\bullet *}AU_n = T_n, \tag{3.171}$$
$$U_{n+1}^{\bullet *}U_{n+1} = D_{n+1} \tag{3.172}$$

where $U_n = [\boldsymbol{u}_1, \boldsymbol{u}_2, \ldots, \boldsymbol{u}_n], U_n^\bullet = [\boldsymbol{u}_1^\bullet, \boldsymbol{u}_2^\bullet, \ldots, \boldsymbol{u}_n^\bullet]$ are the matrix whose column is the biorthonormal Krylov subspace bases, $D_n = [\kappa_1, \kappa_3, \ldots, \kappa_{2n-1}]$, and

$$T_n = \begin{bmatrix} -\kappa_1\kappa_2 & \kappa_3\kappa_2 & & & 0 \\ \kappa_1\kappa_2 & -\kappa_3(\kappa_2+\kappa_4) & \ddots & & \\ & \ddots & \ddots & & \\ & & -\kappa_{2n-3}(\kappa_{2n-4}+\kappa_{2n-2}) & \kappa_{2n-1}\kappa_{2n-2} & \\ 0 & & \kappa_{2n-3}\kappa_{2n-2} & -\kappa_{2n-1}(\kappa_{2n-2}+\kappa_{2n}) & \end{bmatrix}. \tag{3.173}$$

Let us consider the transfer function given as

$$\begin{aligned} \mathcal{H}(s) &= \boldsymbol{c}^\top (K+sN)^{-1}\boldsymbol{b} \\ &= \boldsymbol{u}_1^{\bullet\top}(I-\sigma A)^{-1}\boldsymbol{u}_1 \end{aligned} \tag{3.174}$$

where $\sigma = s - s_0$, $A = -(K+s_0N)^{-1}N$, $\boldsymbol{u}_1 = (K+s_0N)^{-1}\boldsymbol{b}$, $\boldsymbol{u}_1^\bullet = \boldsymbol{c}$. By changing the orthonormal condition in the PVL method to $U_i(0) = 1, i = 0, 1, \ldots,$ we obtain the reduced-order model in the form of the continued fraction.

$$\begin{aligned} \mathcal{H}_n(\sigma) &= \boldsymbol{u}_1^{\bullet\top}\boldsymbol{u}_1 \cdot \boldsymbol{e}_1^\top (I-\sigma T_n)^{-1}\boldsymbol{e}_1 \\ &= \cfrac{1}{\cfrac{1}{\kappa_1} + \cfrac{1}{\cfrac{1}{\sigma\kappa_2} + \cfrac{1}{\cfrac{1}{\kappa_3} + \cfrac{\ddots}{\cfrac{1}{\kappa_{2n-1}} + \cfrac{1}{\cfrac{1}{\sigma\kappa_{2n}}}}}}}} \\ &= \left[0; \tfrac{1}{\kappa_1}, \tfrac{1}{\sigma\kappa_2}, \tfrac{1}{\kappa_3}, \cdots, \tfrac{1}{\kappa_{2n-1}}, \tfrac{1}{\sigma\kappa_{2n}}\right] \end{aligned} \tag{3.175}$$

The non-Hermitian version of CVL is shown in Algorithm 8. Here, we assume that there is no breakdown in the iteration. Using the algorithm, we obtain the Cauer circuit Fig. 3.9 - 3.12.

3.3.5 Cauer circuit via transposition free non-Hermitian Lanczos

In Algorithm 8, we have to compute the inverse matrices K^{-1} and $K^{-\top}$. In the generation of reduced-order model of the Darwin model of Maxwell's equations, we cannot take the inverse of $K^{-\top}$. This is explained in Chapter 5. In this part, we discuss the numerically equivalent but transposition free CVL algorithm.

In the context of the iterative methods for asymmetric matrices, there are techniques for stabilizing the BCG algorithm which is based on the non-Hermitian Lanczos algorithm. The conjugate gradient squared (CGS) algorithm [75] is one of them. The CGS

Algorithm 8 Cauer circuit via non-Hermitian Lanczos algorithm

Input: expansion point s_0, non-Hermitian matrices $K, N \in \mathbb{R}^{N\times N}$, vectors $\boldsymbol{b}, \boldsymbol{c} \in \mathbb{R}^N$, $A = -(K + s_0N)^{-1}N$, iteration step n.

Output: set of biorthogonal vectors $\boldsymbol{u}_1, \ldots, \boldsymbol{u}_n$, $\boldsymbol{u}_1^\bullet, \ldots, \boldsymbol{u}_n^\bullet$, $\boldsymbol{v}_1, \ldots, \boldsymbol{v}_n$, $\boldsymbol{v}_1^\bullet, \ldots, \boldsymbol{v}_n^\bullet$ and parameters in the continued fraction expansion $\kappa_1, \ldots, \kappa_{2n}$.

Initialisation :$\boldsymbol{u}_1 = (K + s_0N)^{-1}\boldsymbol{b}$, $\boldsymbol{u}_1^\bullet = \boldsymbol{c}$, $(\boldsymbol{u}_1, \boldsymbol{u}_1^\bullet) = \kappa_1, \boldsymbol{v}_0 = \boldsymbol{0}, \boldsymbol{v}_0^\bullet = \boldsymbol{0}$.

1: **for** $i = 1$ to d **do**
2: $\quad \boldsymbol{v}_i = \boldsymbol{v}_{i-1} + \frac{1}{\kappa_{2i-1}}\boldsymbol{u}_i, \boldsymbol{v}_i^\bullet = \boldsymbol{v}_{i-1}^\bullet + \frac{1}{\kappa_{2i-1}}\boldsymbol{u}_i^\bullet$,
3: $\quad \kappa_{2i} = -(A\boldsymbol{v}_i, \boldsymbol{v}_i^\bullet)$,
4: $\quad \boldsymbol{u}_{i+1} = \boldsymbol{u}_i + \frac{1}{\kappa_{2i}}A\boldsymbol{v}_i, \boldsymbol{u}_{i+1}^\bullet = \boldsymbol{u}_i^\bullet + \frac{1}{\kappa_{2i}}A^\top\boldsymbol{v}_i^\bullet$,
5: $\quad \kappa_{2i+1} = (\boldsymbol{u}_{i+1}, \boldsymbol{u}_{i+1}^\bullet)$,
6: **end for**
7: **return** $\boldsymbol{u}_1, \ldots, \boldsymbol{u}_n$, $\boldsymbol{u}_1^\bullet, \ldots, \boldsymbol{u}_n^\bullet$, $\boldsymbol{v}_1, \ldots, \boldsymbol{v}_n$, $\boldsymbol{v}_1^\bullet, \ldots, \boldsymbol{v}_n^\bullet$, $\kappa_1, \ldots, \kappa_{2n}$.

method does not require matrix transposition, but it is an equivalent algorithm to the BCG method. Using the same principle, we consider that we can derive the transposition free CVL algorithm.

Let us consider the i-th step of the CVL algorithm. We find the circuit parameters are determined by

$$\kappa_{2i} = -(AV_{i-1}(A)\boldsymbol{u}_1, V_{i-1}(A^*)\boldsymbol{u}_1^\bullet), \tag{3.176}$$
$$\kappa_{2i+1} = (U_{i-1}(A)\boldsymbol{u}_1, U_{i-1}(A^*)\boldsymbol{u}_1^\bullet). \tag{3.177}$$

These are equivalent to

$$\kappa_{2i} = -(AV_{i-1}^2(A)\boldsymbol{u}_1, \boldsymbol{u}_1^\bullet), \tag{3.178}$$
$$\kappa_{2i+1} = (U_{i-1}^2(A)\boldsymbol{u}_1, \boldsymbol{u}_1^\bullet). \tag{3.179}$$

If we obtain the new vectors $\widetilde{\boldsymbol{u}}_i = U_{i-1}^2(A)\boldsymbol{u}_1, \widetilde{\boldsymbol{v}}_i = V_{i-1}^2(A)\boldsymbol{u}_1$, we do not need the computation of the transposition of A. Indeed, we obtain the two-term recurrence relations for $V_{i-1}^2(\lambda)$ and $U_i^2(\lambda)$ by taking the square of both side of the two term recurrence relations as follows:

$$\begin{aligned} V_{i-1}^2(\lambda) &= (V_{i-2}^2(\lambda) + \frac{1}{\kappa_{2i-1}}U_{i-1}(\lambda))^2 \\ &= V_{i-2}^2(\lambda) + \frac{2}{\kappa_{2i-1}}U_{i-1}(\lambda)V_{i-2}(\lambda) + \frac{1}{\kappa_{2i-1}^2}U_{i-1}^2(\lambda) \end{aligned} \tag{3.180}$$

$$\begin{aligned} U_i^2(\lambda) &= (U_{i-1}^2(\lambda) + \frac{\lambda}{\kappa_{2i}}V_{i-1}(\lambda))^2 \\ &= U_{i-1}^2(\lambda) + \frac{\lambda}{\kappa_{2i}}(2U_{i-1}(\lambda)V_{i-1}(\lambda) + \frac{\lambda}{\kappa_{2i}}V_{i-1}^2(\lambda)) \end{aligned} \tag{3.181}$$

These recurrence relations are not closed due to the terms $U_{i-1}(\lambda)V_{i-2}(\lambda), U_{i-1}(\lambda)V_{i-1}(\lambda)$. To make the recurrence relations closed, we add the following relations:

$$U_{i-1}(\lambda)V_{i-2}(\lambda) = U_{i-2}(\lambda)V_{i-2}(\lambda) + \frac{\lambda}{\kappa_{2i-2}}V_{i-2}^2(\lambda), \tag{3.182}$$

$$U_{i-1}(\lambda)V_{i-1}(\lambda) = U_{i-1}(\lambda)V_{i-2}(\lambda) + \frac{1}{\kappa_{2i-1}}U_{i-1}^2(\lambda) \tag{3.183}$$

which can be derived from the two-term recurrence relations. Setting the auxiliary vectors $\boldsymbol{s}_{i-1} = U_{i-1}(A)V_{i-2}(A)\boldsymbol{u}_1, \boldsymbol{t}_i = U_{i-1}(A)V_{i-1}(A)\boldsymbol{u}_1$, we obtain the transposition free version of the CVL algorithm shown in Algorithm 9. In this algorithm, we have to compute the matrix-vector product of A and $\boldsymbol{p}$ twice per iteration instead of computing the transposition.

Algorithm 9 transposition free version of Cauer circuit via non-Hermitian Lanczos algorithm

Input: expansion point s_0, non-Hermitian matrices $K, N \in \mathbb{R}^{N\times N}$, vectors $\boldsymbol{b}, \boldsymbol{c} \in \mathbb{R}^N$, $A = -(K + s_0N)^{-1}N$, iteration step n.

Output: set of biorthogonal vectors $\widetilde{\boldsymbol{u}}_1, \ldots, \widetilde{\boldsymbol{u}}_n$, $\widetilde{\boldsymbol{v}}_1, \ldots, \widetilde{\boldsymbol{v}}_n$, and parameters in the continued fraction expansion $\kappa_1, \ldots, \kappa_{2n}$.

Initialisation :$\widetilde{\boldsymbol{u}}_1 = (K + s_0N)^{-1}\boldsymbol{b}$, $\boldsymbol{u}_1^\bullet = \boldsymbol{c}$, $(\boldsymbol{u}_1, \boldsymbol{u}_1^\bullet) = \kappa_1, \widetilde{\boldsymbol{v}}_0 = \boldsymbol{0}, \boldsymbol{s}_0 = \boldsymbol{0}$.

1: **for** $i = 1$ to d **do**
2: $\quad\widetilde{\boldsymbol{v}}_i = (\frac{1}{\kappa_{2i-1}})^2\widetilde{\boldsymbol{u}}_i + \frac{2}{\kappa_{2i-1}}\boldsymbol{s}_{i-1} + \widetilde{\boldsymbol{v}}_{n-1}$,
3: $\quad\kappa_{2i} = -(A\widetilde{\boldsymbol{v}}_i, \boldsymbol{u}_1^\bullet)$,
4: $\quad\boldsymbol{t}_i = \boldsymbol{s}_{i-1} + \frac{1}{\kappa_{2i-1}}\widetilde{\boldsymbol{u}}_i$,
5: $\quad\boldsymbol{s}_i = \boldsymbol{t}_i + \frac{1}{\kappa_{2i}}A\widetilde{\boldsymbol{v}}_n$,
6: $\quad\widetilde{\boldsymbol{u}}_{i+1} = \widetilde{\boldsymbol{u}}_i + \frac{1}{\kappa_{2i}}A(\boldsymbol{s}_i + \boldsymbol{t}_i)$,
7: $\quad\kappa_{2i+1} = (\widetilde{\boldsymbol{u}}_{i+1}, \boldsymbol{u}_1^\bullet)$,
8: **end for**
9: **return** $\widetilde{\boldsymbol{u}}_1, \ldots, \widetilde{\boldsymbol{u}}_n, \widetilde{\boldsymbol{v}}_1, \ldots, \widetilde{\boldsymbol{v}}_n, \kappa_1, \ldots, \kappa_{2n}$.

3.3.6 Numerical result

Toy model

First, we consider a simple system governed by

$$(G + sC)\boldsymbol{x} = \boldsymbol{b}u \tag{3.184a}$$

$$y = \boldsymbol{b}^\top\boldsymbol{x} \tag{3.184b}$$

where u and y are the input and output, respectively, and

$$G = \begin{bmatrix} 2 & 0 \\ 0 & 1 \end{bmatrix}, \quad C = \begin{bmatrix} 8 & 2 \\ 2 & 5 \end{bmatrix},$$
$$\boldsymbol{b} = \begin{bmatrix} 1 \\ 2 \end{bmatrix}.$$

$A = -G^{-1}C$ is given by

$$A = \begin{bmatrix} -4 & -1 \\ -2 & -5 \end{bmatrix}. \tag{3.185}$$

Note that A is not symmetric, whereas G and C are self-adjoint matrices. The transfer function is analytically given by

$$\begin{aligned} \mathcal{H}(s) &= \boldsymbol{b}^\top (G + sC)^{-1} \boldsymbol{b} \\ &= \begin{bmatrix} 1 & 2 \end{bmatrix} \begin{bmatrix} 2+8s & 2s \\ 2s & 1+5s \end{bmatrix}^{-1} \begin{bmatrix} 1 \\ 2 \end{bmatrix} \\ &= \frac{1}{36s^2 + 18s + 2} \begin{bmatrix} 1 & 2 \end{bmatrix} \begin{bmatrix} 1+5s & -2s \\ -2s & 2+8s \end{bmatrix} \begin{bmatrix} 1 \\ 2 \end{bmatrix} \\ &= \frac{29s + 9}{10s^2 + 12s + 2} \\ &= \left[0; \tfrac{2}{9}, \tfrac{81}{104s}, \tfrac{2704}{225}, \tfrac{25}{936s}\right]. \end{aligned} \tag{3.186}$$

The continued fraction in the last line is obtained using the Euclidean algorithm. By applying Algorithm 7 to (3.184), the orthogonal basis and constants κ_n are obtained as follows:

$$\boldsymbol{u}_1 = G^{-1}\boldsymbol{b} = \begin{bmatrix} \frac{1}{2} & 0 \\ 0 & 1 \end{bmatrix} \begin{bmatrix} 1 \\ 2 \end{bmatrix} = \begin{bmatrix} \frac{1}{2} \\ 2 \end{bmatrix}$$
$$\kappa_1 = (\boldsymbol{u}_0, \boldsymbol{u}_0)_G = \begin{bmatrix} \frac{1}{2} & 2 \end{bmatrix} \begin{bmatrix} 2 & 0 \\ 0 & 1 \end{bmatrix} \begin{bmatrix} \frac{1}{2} \\ 2 \end{bmatrix} = \frac{9}{2}$$
$$\boldsymbol{v}_1 = -\frac{1}{\kappa_0}\boldsymbol{u}_0 = -\frac{2}{9} \begin{bmatrix} \frac{1}{2} \\ 2 \end{bmatrix} = \begin{bmatrix} -\frac{1}{9} \\ -\frac{4}{9} \end{bmatrix}$$
$$\kappa_2 = (\boldsymbol{v}_1, \boldsymbol{v}_1)_C = \begin{bmatrix} -\frac{1}{9} & -\frac{4}{9} \end{bmatrix} \begin{bmatrix} 8 & 2 \\ 2 & 5 \end{bmatrix} \begin{bmatrix} -\frac{1}{9} \\ -\frac{4}{9} \end{bmatrix} = \frac{104}{81}$$
$$\boldsymbol{u}_2 = \boldsymbol{u}_0 - \frac{1}{\kappa_1} A\boldsymbol{v}_1 = \begin{bmatrix} \frac{1}{2} \\ 2 \end{bmatrix} - \frac{104}{81} \begin{bmatrix} -4 & -1 \\ -2 & -5 \end{bmatrix} \begin{bmatrix} -\frac{1}{9} \\ -\frac{4}{9} \end{bmatrix} = \begin{bmatrix} -\frac{5}{26} \\ -\frac{5}{52} \end{bmatrix}$$
$$\kappa_3 = (\boldsymbol{u}_1, \boldsymbol{u}_1)_G = \begin{bmatrix} -\frac{5}{26} & -\frac{5}{52} \end{bmatrix} \begin{bmatrix} 2 & 0 \\ 0 & 1 \end{bmatrix} \begin{bmatrix} -\frac{5}{26} \\ -\frac{5}{52} \end{bmatrix} = \frac{225}{2704}$$
$$\boldsymbol{v}_2 = \boldsymbol{v}_1 - \frac{1}{\kappa_2}\boldsymbol{u}_1 = \begin{bmatrix} -\frac{1}{9} \\ -\frac{4}{9} \end{bmatrix} - \frac{2704}{225} \begin{bmatrix} -\frac{5}{26} \\ -\frac{5}{52} \end{bmatrix} = \begin{bmatrix} \frac{11}{5} \\ -\frac{8}{5} \end{bmatrix}$$
$$\kappa_4 = (\boldsymbol{v}_2, \boldsymbol{v}_2)_C = \begin{bmatrix} \frac{11}{5} & -\frac{8}{5} \end{bmatrix} \begin{bmatrix} 8 & 2 \\ 2 & 5 \end{bmatrix} \begin{bmatrix} \frac{11}{5} \\ -\frac{8}{5} \end{bmatrix} = \frac{936}{25}$$

From this result, we confirm that each term in the continued fraction expansion of the transfer function is obtained by the proposed algorithm.

Axisymmetric reactor

As the second numerical example, we consider a magnetic reactor widely used in power electric circuits. For simplicity, the magnetic reactor is assumed to be axisymmetric, as shown Fig. 3.14, whereas the proposed method can be applied to three-dimensional problems in principle. When using a mesh with 166681 elements and 83491 nodes, the FE analysis of the time response of this magnetic reactor excited by a pulse width modulation (PWM) requires approximately 30 h with Intel(R) Core i7-7700 CPU @ 3.60 GHz, RAM 8.00 GB. Values κ_n in the Cauer circuit obtained by the proposed method are summarized

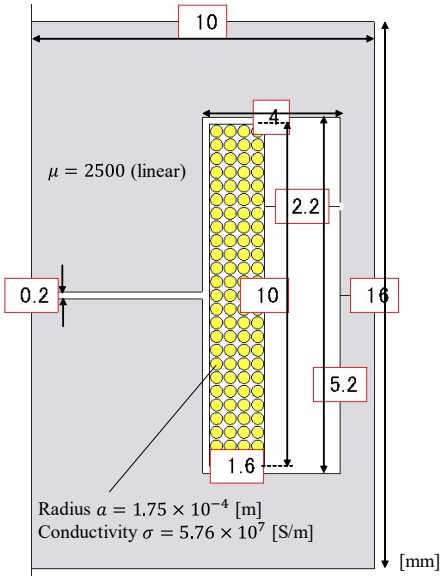

Figure3.14: Axisymmetric reactor.

in Table. 3.1. The frequency characteristics of the reactor are computed by FEM and the obtained equivalent circuit, as shown in Fig. 3.15. To evaluate the dependence on the number of stages, stage number n is increased from 1 to 5. The left figure is the characteristic of the real part of the impedance, which represents the AC resistance, whereas the right is the imaginary part, which represents the stored magnetic energy. The results obtained by using the equivalent circuit are in good agreement with those yielded by FEM, particularly when $n = 5$ where the skin effect is significant.

It takes 49 s to construct a five-stage Cauer circuit that is obtained by truncating Algorithm 7 at $n = 5$ whereas it takes 140 s to get the impedance at each of 27 frequencies by using FEA . While the conventional FEM needs solving the FE equation numerous times to obtain the time response, we rapidly obtain the time response to solve the circuit equation of the obtained Cauer circuit because the dimension of the circuit equation is much smaller than that of the FE equation.

Table3.1: Values in the continued fraction obtained by the proposed method

n	κ_{2n-1}	κ_{2n}
1	5.015×10^{-3}	2.270×10^{-6}
2	1.965×10^{-1}	1.018×10^{-7}
3	1.821×10^{0}	8.433×10^{-8}
4	2.013×10^{0}	3.041×10^{-8}
5	7.055×10^{0}	1.839×10^{-8}

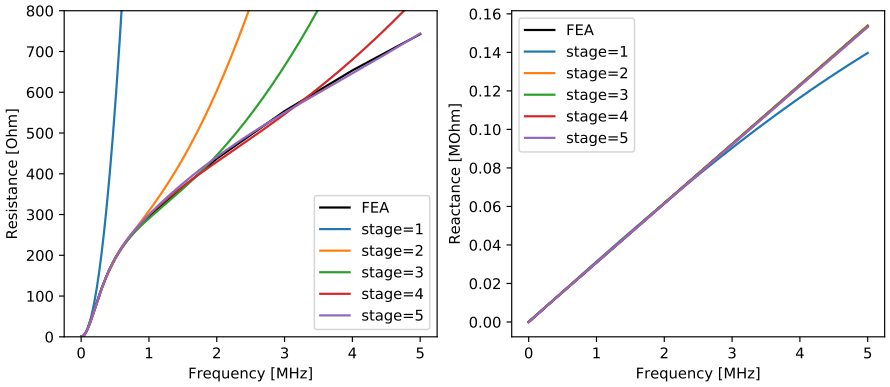

Figure3.15: Frequency characteristic of the obtained continued fraction and the results from FEA.

Then, we performed the time domain analysis of the obtained Cauer circuit excited by a 200 kHz PWM, which is shown in Fig. 3.16. In the time domain analysis, the stage number is fixed to $n = 5$. The waveforms of the Joule losses are plotted in Fig. 3.16. The results obtained from FEM and the DC model which is consisted of the DC resistance and DC inductance are also plotted in the figure. The Joule losses obtained by the DC model is different from the others because of the eddy current effects. We observe that the waveform of the Joule losses obtained by the Cauer circuit is in good agreement with that obtained by FEM. We conclude that the eddy current effects are accurately evaluated by the Cauer circuit.

Note that it takes approximately 2.2 s to obtain the time response by the Cauer circuit, whereas it takes approximately 30 h to do so by FEM. In addition, the Cauer circuit can simulate eddy current losses comparable to those obtained by FEM.

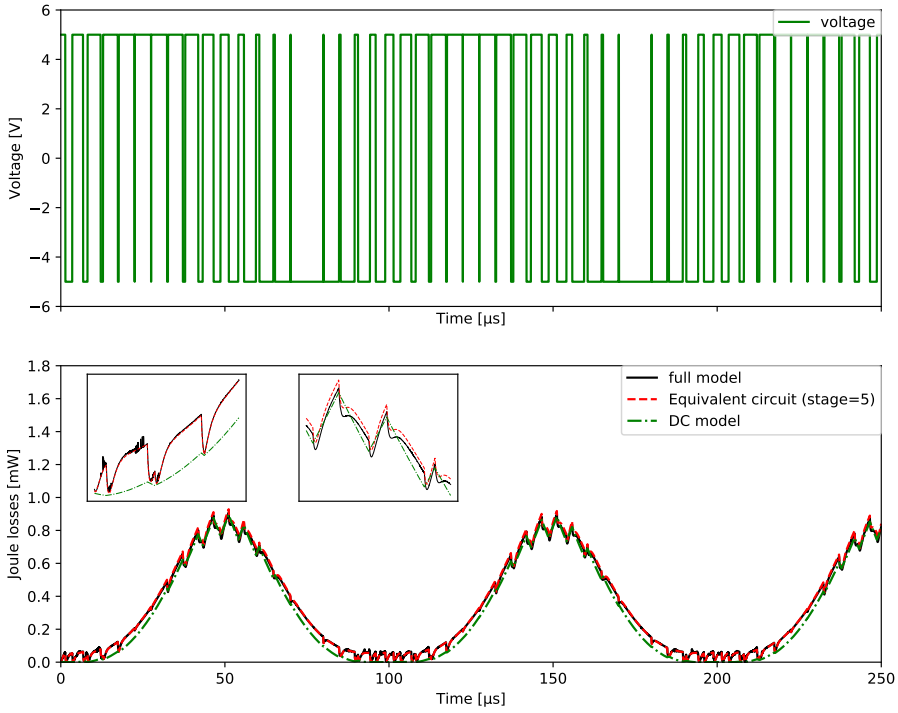

Figure3.16: Temporal changes in voltage and Joule losses obtained by the simple series circuit of DC resistance and inductance (DC model), and proposed linear equivalent circuit and FEM excited by PWM with 200kHz, 5V carrier.

Chapter 4.

Homogenization and model order reduction

4.1 Homogenization method

4.1.1 What is homogenization?

In electromagnetic apparatuses, magnetic composite which consists of the conductors and air is often used to prevent globally flowing eddy currents. For example, consider an iron core used in a transformer. Excitation generates a magnetic flux in the iron core. Since the iron core is conductive, eddy currents are generated to prevent the time variation of the magnetic flux. When the iron core is not divided, large eddy currents are generated globally, as shown in Fig. 4.1 (a). On the other hand, if the iron core is divided and insulated as shown in Fig. 4.1 (b), the loss can be greatly reduced by only allowing eddy currents to flow in each insulating part. Thus, the iron core used in transformers and rotating machines is made of numerous layers of thin steel sheets, i.e., magnetic steel sheets. The Litz wire, which is made by twisting fine wires, and the soft magnetic

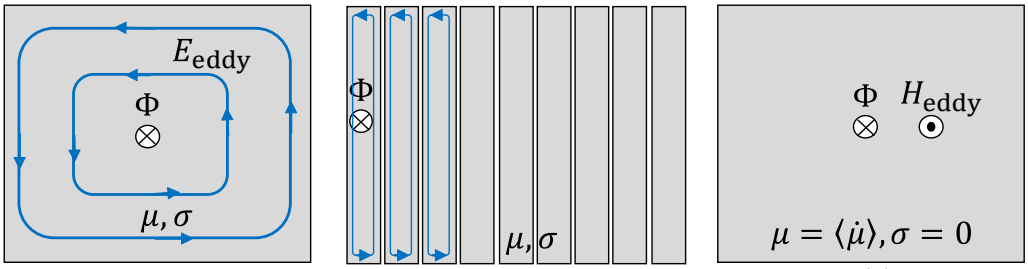

Figure4.1: Eddy currents in the (a) bulk core, (b) divided iron core, and (c) bulk core with complex permeability. In (c), the eddy currents are expressed by the equivalent diamagnetic field H_{eddy}.

composite (SMC), which is made by sintering fine insulated iron powder, are also widely used for the same reason.

Since the electromagnetic apparatus is made of the magnetic composite, it is necessary to divide the conductors into finite elements considering the skin depth in order to calculate the eddy current losses accurately. However, modeling the microstructure and finite element discretization result in a large number of unknowns, which increase the computational cost. The homogenization method is one way to avoid this problem. In the homogenization method, the microstructure is replaced by a homogeneous material which has equivalent macroscopic property to the magnetic composite. The macroscopic properties are expressed by complex permeability $\dot{\mu}$ or $\langle\dot{\mu}\rangle$. In this thesis, $\dot{\mu}$ denotes the complex permeability of a single material and $\langle\dot{\mu}\rangle$ denotes the complex permeability of magnetic composite. Let us consider the magnetic steel sheets illustrated in Fig. 4.1 again. Using the homogenization method, the magnetic steel sheets are replaced by a homogeneous core whose permeability is $\langle\dot{\mu}\rangle$ as shown in Fig. 4.1 (c). Since the conductivity of the homogeneous material is zero, the governing equation can be written by the static Maxwell equations. We do not have to consider the skin depth when we discretize the homogeneous material into the finite elements. Therefore, the overall unknown numbers can be reduced.

4.1.2 Homogenization of plate, cylinder, sphere

In this part, we will give the explicit expression of the complex permeability $\dot{\mu}$ of elementary-shaped conductors such as plates, cylinders, and spheres. It is significant to consider the elementary-shaped conductors because they are widely used in the electromagnetic apparatuses. In addition, using the Ollendorff formula, we can obtain the complex permeability $\langle\dot{\mu}\rangle$ of the composite materials including elementary-shaped conductors.

The complex permeability $\dot{\mu}$ is defined by the average reaction $\overline{B}$ to the uniform magnetic field H_0. It can be written as

$$\dot{\mu} = \frac{\overline{B}}{H_0}. \tag{4.1}$$

If we consider the elementary-shaped conductors such as plates, cylinders, and spheres, we can obtain the average reaction $\overline{B}$ by analytically solving Maxwell's equations.

Plate

Let us consider an isolated infinitely wide flat plate applied to a uniform time-harmonic magnetic field $\boldsymbol{H}_0$ as shown in Fig. 4.2. The thickness of the plate, the conductivity, and the permeability are d, σ and μ, respectively. The coordinate system (x, y, z) is introduced

where y and z-axes are defined parallel to $\boldsymbol{H}_0$ and plate. We consider only $H_y(x), E_z(x)$ as the eddy currents flow in z direction. From the MQS approximation of Maxwell's equations, we have

$$-\frac{\partial H_y}{\partial x} = \sigma E_z, \tag{4.2}$$

$$\frac{\partial E_z}{\partial x} = -\mathrm{j}\omega\mu H_y, \tag{4.3}$$

where ω is the angular frequency. Eliminating E_z from the equations, we obtain

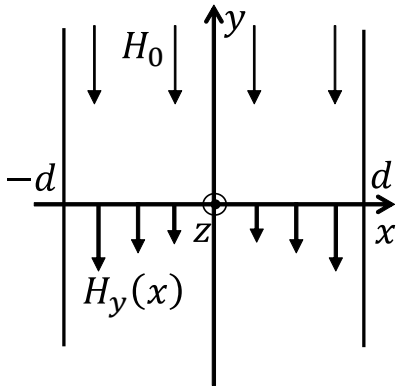

Figure4.2: Cross-section of a plate immersed in a uniform time-harmonic magnetic field.

$$\frac{d^2 H_y}{dx^2} + k^2 H_y = 0 \tag{4.4}$$

where $k^2 = -\mathrm{j}\omega\sigma\mu$. The general solution of the ordinary differential equation is written as

$$H_y = A\cos kx + B\sin kx \tag{4.5}$$

From the boundary conditions

$$H_y(d) = H_0, \tag{4.6}$$

$$E_z(0) = 0, \tag{4.7}$$

we have

$$H_y = H_0 \frac{\cos kx}{\cos kd}. \tag{4.8}$$

The average response can be calculated as

$$\overline{B}_y = \frac{1}{2d}\int_{-d}^{d} \mu H_y dy = \frac{\mu H_0}{2d\cos kd}\left[\frac{1}{k}\sin kx\right]_{-d}^{d} = \mu H_0 \frac{\tan kd}{kd}. \tag{4.9}$$

From the definition, we obtain

$$\dot{\mu} = \frac{\overline{B}_y}{H_0} = \mu \frac{\tan z}{z} = \cfrac{\mu}{1 - \cfrac{z^2}{3 - \cfrac{z^2}{5 - \cfrac{z^2}{\ddots}}}} \tag{4.10}$$

where $z = kd$. The loss density in the plate can be written as

$$w_e = \mathrm{j}\omega\dot{\mu}|H_0|^2. \tag{4.11}$$

By analogy with electric circuits, we can consider $\mathrm{j}\omega\dot{\mu}$ to be equivalent to an impedance.

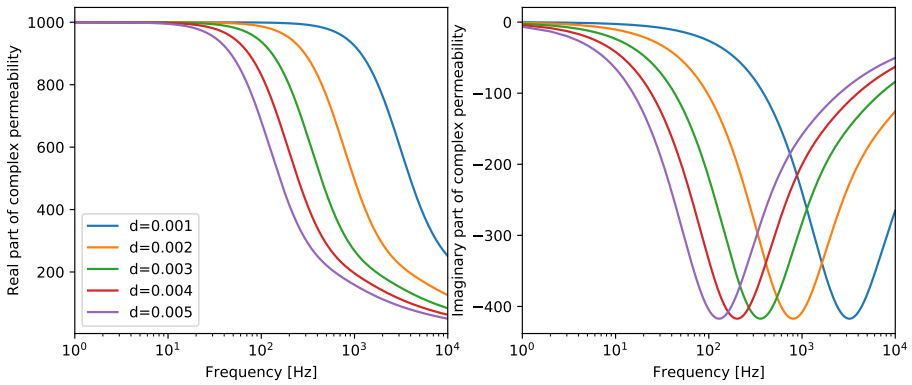

Figure4.3: Frequency dependence of relative complex permeability $\dot{\mu}_r = \mu_r \frac{\tan z}{z}$.

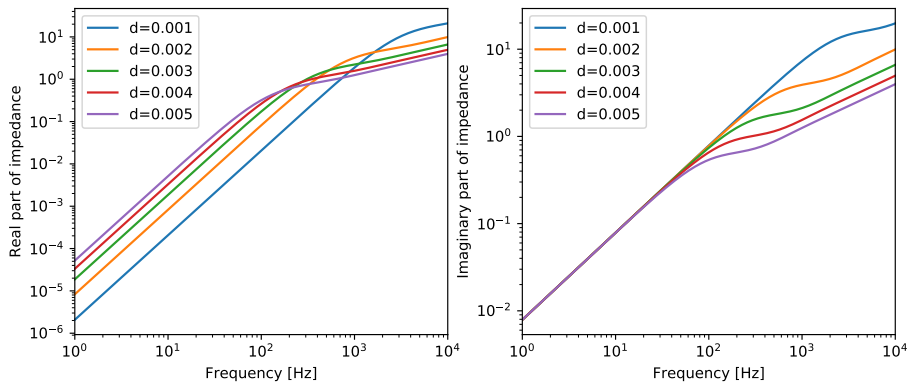

Figure4.4: Frequency dependence of impedance $\mathrm{j}\omega\dot{\mu} = \mathrm{j}\omega\mu\frac{\tan z}{z}$.

In fact, we have

$$\begin{aligned} \mathrm{j}\omega\dot{\mu} &= \cfrac{1}{\cfrac{1}{\mathrm{j}\omega\mu} + \cfrac{1}{\cfrac{3}{\sigma d^2} + \cfrac{1}{\cfrac{5}{\mathrm{j}\omega\mu} + \cfrac{1}{\ddots}}}} \\ &= \left[0; \tfrac{1}{\mathrm{j}\omega\mu}, \tfrac{3}{\sigma d^2}, \tfrac{5}{\mathrm{j}\omega\mu}, \tfrac{7}{\sigma d^2}, \cdots\right] \end{aligned} \tag{4.12}$$

which can be interpreted as the impedance of the Cauer circuit. In Fig. 4.3, the real and imaginary parts of the complex permeability are plotted against the frequency where $\sigma = 1.0^5$ Sm^{-1}, $\mu_r = 1000$. The real and imaginary parts represent the permeability considering the diamagnetic effect of the eddy currents and the eddy current losses. We observe that the real part of the complex decreases monotonically due to the diamagnetic effect of the eddy currents. In Fig. 4.4, the real and imaginary parts of the impedance $\mathrm{j}\omega\dot{\mu}$ are plotted against the frequency. In this case, the real part of the impedance represents the eddy current losses which increases monotonically.

Cylinder

Let us consider an isolated cylinder applied to a uniform time-harmonic magnetic field $\boldsymbol{H}_0$ as shown in Fig. 4.5. The radius of the cylinder, the conductivity, and the permeability are a, σ, and μ, respectively. The coordinate systems (x, y, z) and (r, θ, z) are introduced where y and z-axes are defined parallel to $\boldsymbol{H}_0$ and the longitudinal of the cylinder. We consider only $H_r(r,\theta), H_\theta(r,\theta), E_z(r,\theta)$ as the eddy currents flow in z direction. From the MQS approximation of Maxwell's equations, we have

$$\frac{1}{r}\frac{\partial}{\partial r}(rH_\theta) - \frac{1}{r}\frac{\partial H_r}{\partial \theta} = \sigma E_z, \tag{4.13}$$

$$\frac{1}{r}\frac{\partial E_z}{\partial \theta} = -\mathrm{j}\omega\mu H_r, \tag{4.14}$$

$$-\frac{\partial E_z}{\partial r} = -\mathrm{j}\omega\mu H_\theta. \tag{4.15}$$

Eliminating H_r, H_θ, we have

$$\frac{\partial^2 E_z}{\partial r^2} + \frac{1}{r}\frac{\partial E_z}{\partial r} + \frac{1}{r^2}\frac{\partial^2 E_z}{\partial \theta^2} + k^2 E_z = 0 \tag{4.16}$$

where $k^2 = -\mathrm{j}\omega\sigma\mu$. Applying the variable separation $E_z(r,\theta) = R(r)\Theta(\theta)$, we obtain

$$r^2\frac{d^2R}{dr^2} + r\frac{dR}{dr} + (k^2r^2 - \beta^2)R = 0, \tag{4.17}$$

$$\frac{d^2\Theta}{d\theta^2} + \beta^2\Theta = 0 \tag{4.18}$$

where β is a constant. Due to the periodicity of $E_z(r,\theta)$ for the θ-direction, β must be integer numbers n. Since (4.17) is the Bessel's differential equation, we can write the general solution as follows:

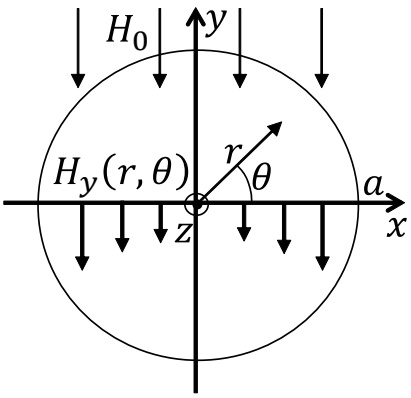

Figure4.5: Cross-section of a cylinder immersed in a uniform time-harmonic magnetic field.

$$E_z(r,\theta) = \sum_{n=0}^{\infty} J_n(kr)(A_n \cos n\theta + B_n \sin n\theta) \tag{4.19}$$

where $J_n(\zeta)$ is the n-th order Bessel function of the first kind. From the boundary conditions

$$H_\theta(a,\theta) = H_0 \cos\theta, \tag{4.20}$$
$$E_z(r,\pi/2) = 0, \tag{4.21}$$

we have

$$E_z(r,\theta) = \frac{\mathrm{j}\omega\mu H_0 J_1(kr)}{kJ_1'(ka)} \cos\theta, \tag{4.22}$$
$$H_\theta(r,\theta) = \frac{H_0 J_1'(kr)}{J_1'(ka)} \cos\theta, \tag{4.23}$$
$$H_r(r,\theta) = \frac{H_0 J_1(kr)}{krJ_1'(ka)} \sin\theta. \tag{4.24}$$

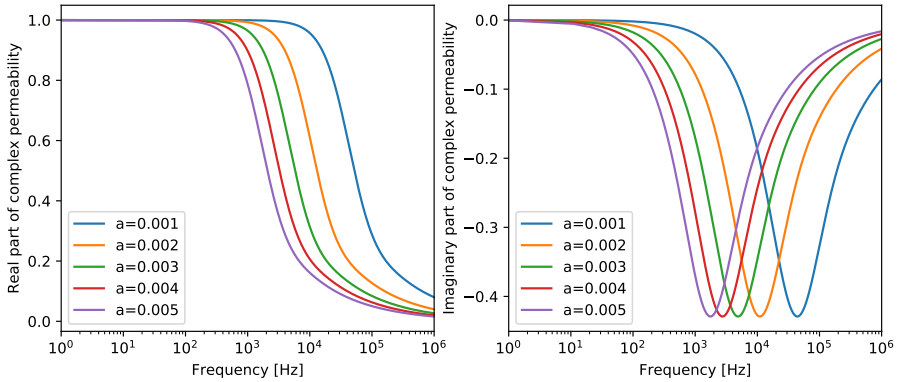

Figure4.6: Frequency dependence of relative complex permeability $\dot{\mu}_r = \mu_r \frac{J_1(z)}{zJ_1'(z)}$.

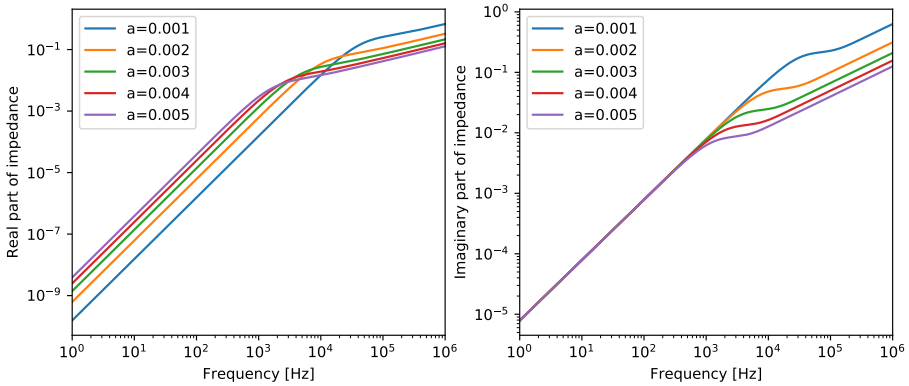

Figure4.7: Frequency dependence of impedance $\mathrm{j}\omega\dot{\mu} = \mathrm{j}\omega\mu\frac{J_1(z)}{zJ_1'(z)}$.

The average response can be calculated as follows:

$$\begin{aligned}
\overline{B}_y &= \frac{\mu}{\pi a^2}\int_0^a rdr\int_0^{2\pi} d\theta(H_\theta\cos\theta + H_r\sin\theta) \\
&= \frac{\mu}{\pi a^2}\frac{H_0\pi}{kJ_1'(ka)}\int_0^a (krJ_1'(kr) + J_1(kr))dr \\
&= \frac{\mu}{\pi a^2}\frac{H_0\pi}{kJ_1'(ka)}\Big[rJ_1(kr)\Big]_0^a \\
&= \mu\frac{J_1(ka)}{kaJ_1'(ka)}H_0
\end{aligned} \tag{4.25}$$

From the definition, we obtain

$$\dot{\mu} = \frac{\overline{B}_y}{H_0} = \mu\frac{J_1(ka)}{kaJ_1'(ka)}. \tag{4.26}$$

This can be also expressed as

$$\dot{\mu} = \mu \frac{J_1(z)}{zJ_1'(z)} = \mu \frac{1}{\frac{zJ_0(z)}{J_1(z)} - 1} = \cfrac{\mu}{1 - \cfrac{z^2}{4 - \cfrac{z^2}{6 - \cfrac{z^2}{\ddots}}}} \tag{4.27}$$

$$\mathrm{j}\omega\dot{\mu} = \left[0; \tfrac{1}{\mathrm{j}\omega\mu}, \tfrac{4}{\sigma a^2}, \tfrac{6}{\mathrm{j}\omega\mu}, \tfrac{8}{\sigma a^2}, \cdots\right] \tag{4.28}$$

where $z = ka$. The derivation using the equivalent dipole moment is given in [53]. In Fig. 4.6, the profile of the complex permeability is plotted as the frequency where $\sigma = 1.0^7$ Sm^{-1}, $\mu_r = 1.0$. In Fig. 4.7, the profile of the impedance $\mathrm{j}\omega\dot{\mu}$ is plotted as the frequency.

Sphere

Let us consider an isolated sphere applied to a uniform time-harmonic magnetic field $\boldsymbol{H}_0$ as shown in Fig. 4.8. The radius of the sphere, the conductivity, and the permeability are a, σ, and μ, respectively. The coordinate systems (x, y, z) and (r, θ, φ) are introduced where y are defined parallel to $\boldsymbol{H}_0$. We consider only $H_r(r,\theta), H_\theta(r,\theta), E_\varphi(r,\theta)$ as the eddy currents flow in φ-direction. From the MQS approximation of Maxwell's equations, we have

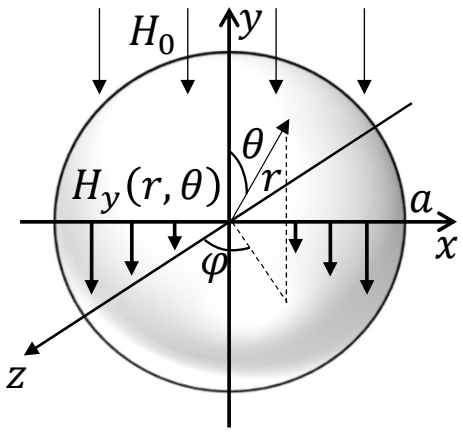

Figure4.8: A sphere immersed in a uniform time-harmonic magnetic field.

$$\frac{1}{r}\left[\frac{\partial}{\partial r}(rH_\theta) - \frac{\partial H_r}{\partial \theta}\right] = \sigma E_\varphi, \tag{4.29}$$

$$\frac{1}{r\sin\theta}\frac{\partial}{\partial\theta}(E_\varphi \sin\theta) = -\mathrm{j}\omega\mu H_r, \tag{4.30}$$

$$-\frac{1}{r}\frac{\partial}{\partial r}(rE_\varphi) = -\mathrm{j}\omega\mu H_\theta \tag{4.31}$$

Eliminating H_r, H_θ, we have

$$\frac{1}{r}\left[\frac{\partial^2}{\partial r^2}(rE_\varphi)+\frac{\partial}{\partial\theta}\left(\frac{1}{r\sin\theta}\frac{\partial}{\partial\theta}(E_\varphi\sin\theta)\right)\right]+k^2E_\varphi=0 \tag{4.32}$$

where $k^2=-\mathrm{j}\omega\sigma\mu$. Applying the variable separation $E_\varphi(r,\theta)=R(r)\Theta(\theta)$, we obtain

$$r\frac{d^2}{dr^2}(rR)+(k^2r^2-\beta^2)R=0, \tag{4.33}$$

$$\frac{d}{d\theta}\left(\frac{1}{\sin\theta}\frac{d}{d\theta}(\Theta\sin\theta)\right)+\beta^2\Theta=0. \tag{4.34}$$

The second equation can be written as

$$\frac{1}{\sin\theta}\frac{d}{d\theta}\left(\sin\theta\frac{d\Theta}{d\theta}\right)+\left(\beta^2-\frac{1}{\sin\theta^2}\right)\Theta=0. \tag{4.35}$$

Applying the change of variable $t=\cos\theta$, we obtain

$$\frac{d}{dt}\left(\frac{1}{1-t^2}\frac{d\Theta}{dt}\right)+\left(\beta^2-\frac{1}{1-t^2}\right)\Theta=0. \tag{4.36}$$

This is the associated Lengendre differential equation. We can find the bounded solutions if and only if $\beta^2=l(l+1)$ where l is a integer number. The solutions $P_l^1(t), Q_l^1(t)$ are called the l-th order associated Legendre polynomials and l-th order Legendre functions of the second kind.

Then, equation (4.33) can be written as

$$\frac{d^2R}{dr^2}+\frac{2}{r}\frac{dR}{dr}+\left(k^2-\frac{l(l+1)}{r^2}\right)R=0. \tag{4.37}$$

This is the spherical Bessel differential equation. The solutions $j_l(kr), n_l(kr)$ are called the spherical Bessel function and spherical Neumann function. Since the spherical Neumann function diverges at the origin, the general solution of our interest can be written as

$$E_\varphi(r,\theta)=\sum_{l=0}^{\infty}j_l(kr)(A_{l1}P_l^1(\cos\theta)+B_{l1}Q_l^1(\cos\theta)). \tag{4.38}$$

From the boundary conditions

$$H_\theta(a,\theta)=H_0\sin\theta, \tag{4.39}$$

$$E_\varphi(r,0)=0, \tag{4.40}$$

we have

$$E_\varphi(r,\theta)=A_{11}j_1(kr)P_1^1(\cos\theta)=-A_{11}j_1(kr)\sin\theta \tag{4.41}$$

$$H_\theta(r,\theta)=-\frac{A_{11}}{\mathrm{j}\omega\mu r}\frac{d}{dr}(rj_1(kr))\sin\theta \tag{4.42}$$

$$H_r(r,\theta)=\frac{A_{11}}{\mathrm{j}\omega\mu r}j_1(kr)2\cos\theta \tag{4.43}$$

where

$$A_{11} = \frac{\mathrm{j}\omega\mu a H_0}{j_1(ka) + kaj_1'(ka)}. \tag{4.44}$$

The average response can be calculated as

$$\begin{aligned}
\overline{B}_y &= \frac{\mu}{\frac{4\pi a^3}{3}} \int_0^a r^2 dr \int_0^\pi \sin\theta d\theta \int_0^{2\pi} d\varphi (H_r \cos\theta - H_\theta \sin\theta) \\
&= \frac{3\mu}{4\pi a^3} \frac{2\pi A_{11}}{\mathrm{j}\omega\mu} \int_0^a r dr \int_0^\pi \left(j_1(kr) 2\cos\theta^2 \sin\theta + \frac{d}{dr}(r j_1(kr)) \sin\theta^3 \right) d\theta \\
&= \frac{3\mu}{4\pi a^3} \frac{2\pi A_{11}}{\mathrm{j}\omega\mu} \frac{4}{3} \int_0^a \left(r j_1(kr) + r \frac{d}{dr}(r j_1(kr)) \right) dr \\
&= \frac{\mu}{a^3} \frac{2A_{11}}{\mathrm{j}\omega\mu} \left[r^2 j_1(kr) \right]_0^a \\
&= \frac{\mu}{a^3} \frac{2A_{11}}{\mathrm{j}\omega\mu} a^2 j_1(ka) \\
&= \frac{2\mu j_1(ka)}{j_1(ka) + kaj_1'(ka)} H_0.
\end{aligned} \tag{4.45}$$

From the definition, we obtain

$$\begin{aligned}
\dot{\mu} = \frac{\overline{B}_y}{H_0} &= \mu \frac{2j_1(z)}{j_1(z) + zj_1'(z)} = \mu \frac{2(z - \tan z)}{(1 - z^2)\tan z - z} \\
&= \cfrac{2\mu}{2 - \cfrac{z^2}{5 - \cfrac{z^2}{7 - \cfrac{z^2}{\ddots}}}}
\end{aligned} \tag{4.46}$$

$$\mathrm{j}\omega\dot{\mu} = \left[0; \tfrac{1}{\mathrm{j}\omega\mu}, \tfrac{10}{\sigma a^2}, \tfrac{7}{2\mathrm{j}\omega\mu}, \tfrac{18}{\sigma a^2}, \tfrac{11}{2\mathrm{j}\omega\mu}, \cdots \right] \tag{4.47}$$

where $z = ka$. This result is consistent with that given in [101]. In Fig. 4.9, the profile of the complex permeability is plotted as the frequency where $\sigma = 1.0^6$ Sm^{-1}, $\mu_r = 10.0$. In Fig. 4.10, the profile of the impedance $\mathrm{j}\omega\dot{\mu}$ is plotted against the frequency.

Once we obtain the complex permeability $\dot{\mu}$, we can use it in FEA. It has been shown the eddy current losses P_{eddy} due to the uniform magnetic field H_0 can correctly be computed by using the complex permeability. The complex power can be written as

$$P = \frac{\mathrm{j}\omega}{2} \int_\Omega \mu |\boldsymbol{H}|^2 d\Omega \tag{4.48}$$

where μ is set to $\dot{\mu}$ in the homogenized material. The real and imaginary parts represent the sum of P_{eddy} and time variation in the stored magnetic energy. Note here that the homogenized materials can be subdivided into the finite elements without considering the skin depth. Thus the number of unknowns can be reduced.

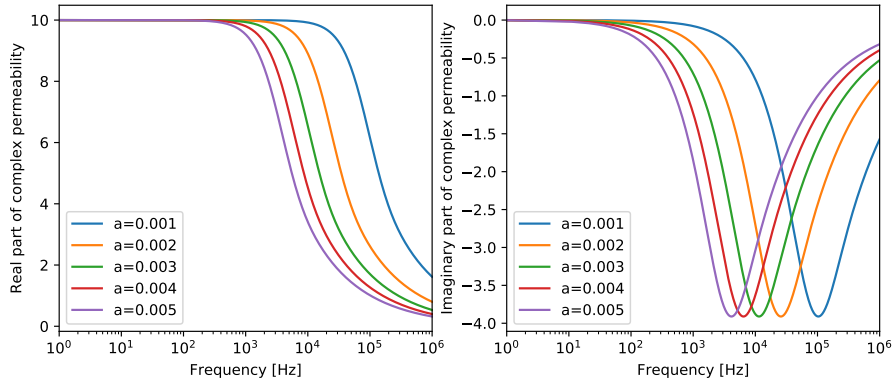

Figure4.9: Frequency dependence of relative complex permeability $\dot{\mu}_r = \mu_r \frac{2(z-\tan z)}{(1-z^2)\tan z - z}$.

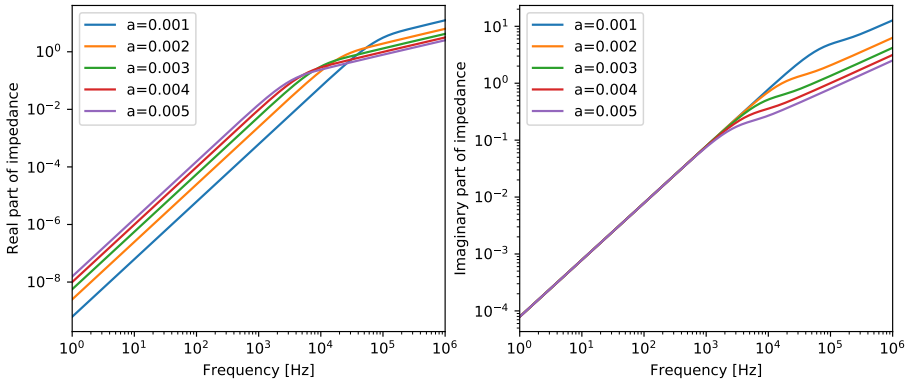

Figure4.10: Frequency dependence of impedance $\mathrm{j}\omega\dot{\mu} = \mathrm{j}\omega\mu \frac{2(z-\tan z)}{(1-z^2)\tan z - z}$.

However, the FE discretization of each homogenization would still result in a large equation when the number of the elementary-shaped conductors is large. To overcome this problem, homogenization of magnetic composite is effective. In the next part, we introduce the two kinds of homogenization approach: Ollendorff formula and unit cell approach.

4.1.3 Ollendorff formula and unit cell approach

Ollendorff formula

Since the complex permeability represents the average response to the uniform magnetic fields, we no longer have to consider the eddy currents inside the conductor. However, the microstructure consists of the conductors and air. To deal with such magnetic composite, the Ollendorff formula [54, 53] can be effectively used. The Ollendorff formula is given as

$$\langle \mu_r \rangle = 1 + \frac{\eta(\mu_r - 1)}{1 + N(1-\eta)(\mu_r - 1)} \tag{4.49}$$

where η, N are the volume fraction and diamagnetic constant of the elementary-shaped conductor. This formula is essentially equivalent to the Maxwell-Garnett formula [102], which is widely used in microwave engineering, and the Clausius-Mossotti formula [101], which is widely used to evaluate the macroscopic permittivity of nonpolar molecules. Igarashi [53] has proposed the extension of the Ollendorff formula to the evaluation of the frequency response of the magnetic composite. The extended Ollendorff formula is given as

$$\langle \dot{\mu}_r \rangle = 1 + \frac{\eta(\dot{\mu}_r - 1)}{1 + N(1-\eta)(\dot{\mu}_r - 1)} \tag{4.50}$$

If we consider the magnetic composite of the round wire, the diamagnetic constant becomes $N = 1/2$.

The frequency characteristics of the complex permeability $\langle \dot{\mu} \rangle$ of the magnetic composite including cylinders are plotted in Fig. 4.11 where $a = 0.005$ m, $\sigma = 1.0^7$ Sm^{-1}, $\mu_r = 1.0$. The curves for eta=1 are plotted as a limited case which cannot be realized by cylinders. In Fig. 4.12, the profile of the impedance $\mathrm{j}\omega\langle \dot{\mu} \rangle$ is plotted as the frequency.

It is possible to treat the magnetic composite including the elementary-shaped conductors as a homogeneous material whose permeability is $\langle \dot{\mu} \rangle$. Note that the homogeneous materials can be subdivided into finite elements without considering the magnetic composite such as conductors and air. Therefore, the number of unknowns can be reduced when the number of the conductors is large.

Unit cell approach

The Ollendorff formula is effective when we consider the magnetic composite including the elementary-shaped conductors whose complex permeability $\dot{\mu}$ and diamagnetic constant N are obtained analytically. For more general cases such as the magnetic composite including the rectangular or multiple conductors, it is difficult to obtain $\langle \dot{\mu} \rangle$ because $\dot{\mu}, N$ are not obtained analytically. To deal with the problems, the unit cell approach can be effectively used [55, 56, 57]. In this approach, the homogenized complex permeability $\langle \dot{\mu} \rangle$ is evaluated by performing FE analysis in a elementary cell under appropriate boundary conditions.

Let us consider the magnetic composite as shown in Fig. 4.13. We assume that the elementary cell Ω_{u}, which is so-called unit cell, spans periodically. The unit cell consists of a conductor whose conductivity and permeability are σ, μ and air. The coordinate system (x, y, z) is introduced where the uniform magnetic field $H_0 = B_0/\mu_0$ is parallel to y-axis shown in Fig. 4.14. The boundary conditions are given as follows:

$$\boldsymbol{A} \times \boldsymbol{n} = \boldsymbol{0}, \quad \text{on } \Gamma_{\mathrm{N}}, \tag{4.51}$$

$$\boldsymbol{A} = \pm B_0 w \boldsymbol{e}_z, \quad \text{on } \Gamma_{\mathrm{D}}. \tag{4.52}$$

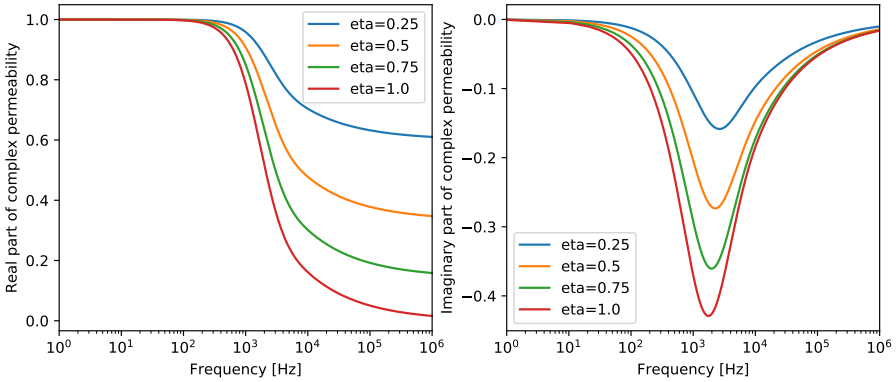

Figure4.11: Frequency dependence of relative complex permeability $\langle \dot{\mu}_r \rangle$.

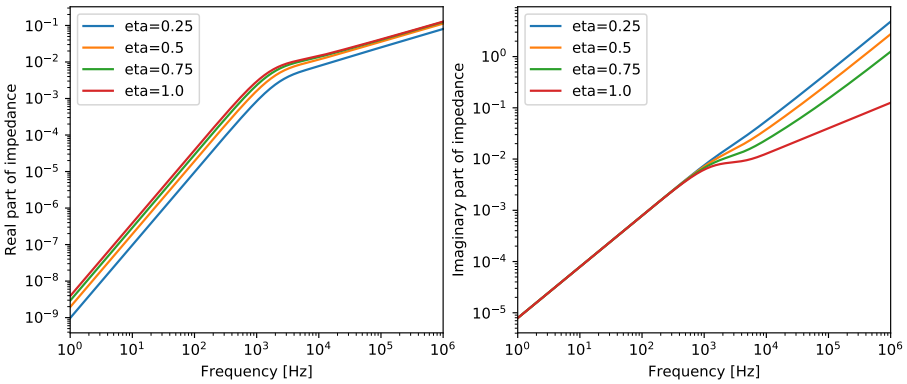

Figure4.12: Frequency dependence of impedance $j\omega\langle \dot{\mu} \rangle$.

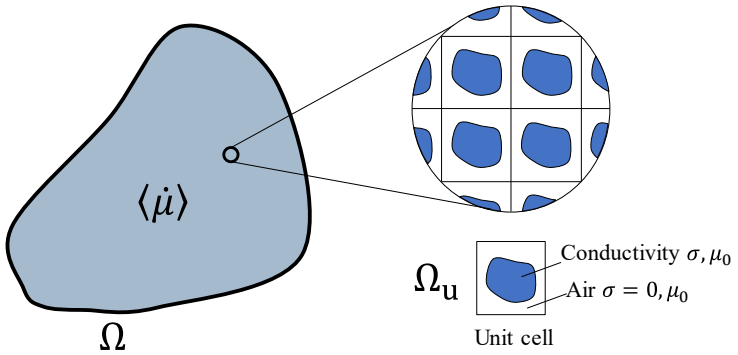

Figure4.13: Magnetic composite consisted of conductors and air

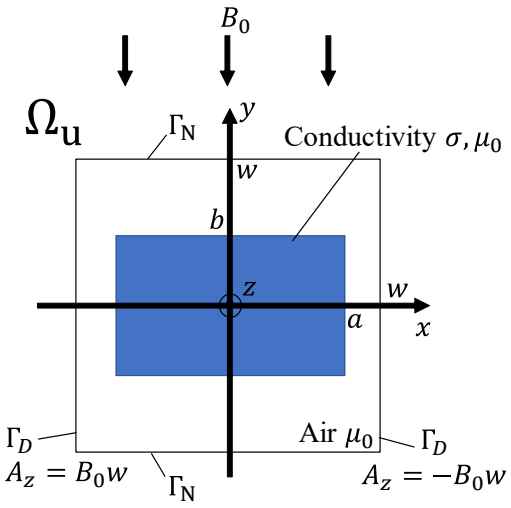

Figure4.14: Unit cell applied to the uniform magnetic field $H_0 = B_0/\mu_0$

where $\boldsymbol{n}$ is outer unit normal on the boundary $\partial\Omega_u$. Solving the MQS approximation of Maxwell's equations,

$$\nabla \times \boldsymbol{H} = \sigma \boldsymbol{E}, \tag{4.53}$$

$$\nabla \times \boldsymbol{E} = -\mathrm{j}\omega \boldsymbol{B}, \tag{4.54}$$

we obtain the electromagnetic fields $\boldsymbol{B}(\omega), \boldsymbol{E}(\omega)$ for each frequency. There are several methods to obtain the complex permeability $\langle \dot{\mu} \rangle$. One is the method using the average magnetization [56],

$$\langle \dot{\mu} \rangle = \frac{1}{1 - \frac{\mu_0 \overline{M}}{B_0}}, \tag{4.55}$$

$$\overline{M} = \mathrm{j}\omega \int_{\Omega_u} \sigma x A_z d\Omega. \tag{4.56}$$

This method is effective when we consider the conductor whose permeability is $\mu = 1$. The second is the method using the equivalence of the energy [57],

$$\langle \dot{\mu} \rangle = \frac{-\mathrm{j}\omega \int_{\Omega_u} |B|_0^2 d\Omega}{-\mathrm{j}\omega \int_{\Omega_u} |\boldsymbol{B}|^2/\mu d\Omega + \int_{\Omega_u} \sigma |\boldsymbol{E}|^2 d\Omega}. \tag{4.57}$$

The formula can be applied to the unit cell including the conductor whose permeability is not necessary $\mu = 1$.

Although this approach seems to be effective, one has to perform FEA to obtain $\langle \dot{\mu} \rangle$ for different frequencies and volume fractions of the homogeneous materials. To circumvent this problem, we have proposed a new method using the CVL algorithm 8 to obtain the closed form of the complex permeability $\langle \dot{\mu} \rangle$.

4.2 Model order reduction for unit cell analysis

4.2.1 Formulation

To obtain the complex permeability in a closed form, we make FE equation

$$(K + sN)\boldsymbol{x} = \boldsymbol{b}B_0 \tag{4.58}$$

where $\boldsymbol{x} \in \mathbb{C}^N, \boldsymbol{b} \in \mathbb{R}^N, s \in \mathbb{C}$ are the unknown and right hand side vectors, and complex frequency $\mathrm{j}\omega$, respectively. In two-dimensional case, we use the node interpolation functions w_i^n to obtain the FE equation. The matrices can be written as

$$K_{ij} = \int_\Omega \nabla w_i^n \cdot \nu \nabla w_j^n d\Omega, \tag{4.59}$$

$$N_{ij} = \int_\Omega \sigma w_i^n w_j^n d\Omega, \tag{4.60}$$

where ν is the magnetic resistivity. The right hand side vector becomes

$$b_i = \pm \sum_{j=1}^{N} \int_\Omega \nabla w_i^n \cdot \nu \nabla w_j^n d\Omega, \quad \text{where } i \in \Gamma_\mathrm{D}. \tag{4.61}$$

Note that the right hand side vector arises from the Dirichlet boundary condition. To obtain the complex permeability in the closed form, we have to make the transfer function. To do so, we first focus on the denominator of the complex permeability (4.57). The denominator represents the complex permeability stored in the unit cell. To express it by the FE matrices, we use the following deformation.

$$\mathrm{j}\omega \int_{\Omega_\mathrm{u}} \frac{|\boldsymbol{B}|^2}{\mu} d\Omega + \int_{\Omega_\mathrm{u}} \sigma |\boldsymbol{E}|^2 d\Omega = -\int_{\partial\Omega_\mathrm{u}} \boldsymbol{E} \times \boldsymbol{H}^* \boldsymbol{n} dS. \tag{4.62}$$

The right hand side, which represents the surface integral of the Poynting vector, is discretized by FEM to obtain

$$\begin{aligned} -\int_{\partial\Omega_\mathrm{u}} \boldsymbol{E} \times \boldsymbol{H}^* \cdot \boldsymbol{n} dS &= \mathrm{j}\omega \int_{\partial\Omega_\mathrm{u}} \boldsymbol{A} \times (\nabla \times \boldsymbol{A}^*) \cdot \boldsymbol{n} dS \\ &= \pm \mathrm{j}\omega w B_0 \int_{\partial\Omega_\mathrm{u}} \boldsymbol{e}_z \times (\nabla \times \boldsymbol{A}^*) \cdot \boldsymbol{n} dS \\ &= \mathrm{j}\omega \boldsymbol{c}^\top \boldsymbol{x}^* B_0 \\ &= \mathrm{j}\omega \boldsymbol{c}^\top (K - \mathrm{j}\omega N)^{-1} \boldsymbol{b} |B_0|^2 \end{aligned} \tag{4.63}$$

Substituting it into (4.57) yields

$$\begin{aligned} \langle \dot{\mu} \rangle &= \frac{-\mathrm{j}\omega \int_{\Omega_\mathrm{u}} |B|_0^2 d\Omega}{-\int_{\partial\Omega_\mathrm{u}} \boldsymbol{E}^* \times \boldsymbol{H} \cdot \boldsymbol{n} dS} \\ &= \frac{V}{\boldsymbol{c}^\top (K + \mathrm{j}\omega N)^{-1} \boldsymbol{b}} \end{aligned} \tag{4.64}$$

where $V = \int_{\Omega_u} d\Omega$ denotes the volume or are of the unit cell. To derive the Cauer representation of the complex permeability, we expand the denominator

$$\begin{aligned} \boldsymbol{c}^\top (K + \mathrm{j}\omega N)^{-1} \boldsymbol{b} &= \boldsymbol{l}^\top (I - sA)^{-1} \\ &= \boldsymbol{l}^\top \boldsymbol{r} + s\boldsymbol{l}^\top A\boldsymbol{r} + s^2 \boldsymbol{l}^\top A^2 \boldsymbol{r} + \cdots \\ &= \boldsymbol{l}^\top \boldsymbol{r} + s\boldsymbol{l}^\top (I - sA)^{-1} A\boldsymbol{r} \end{aligned} \tag{4.65}$$

where $\boldsymbol{l} = \boldsymbol{c}, \boldsymbol{r} = K^{-1}\boldsymbol{b}, A = -K^{-1}N$, and $s = \mathrm{j}\omega$. The first and second terms represent the dc inductance and frequency-dependent term. By applying CVL algorithm 8 to the second term, we obtain the finite continued fraction expression as follows:

$$\begin{aligned} \langle \dot{\mu} \rangle &= \frac{V}{\boldsymbol{l}^\top \boldsymbol{r} + s\boldsymbol{l}^\top (I - sA)^{-1} A\boldsymbol{r}} \\ &= \cfrac{1}{\cfrac{1}{\kappa_1} + \cfrac{1}{\cfrac{1}{s\kappa_2} + \cfrac{1}{\cfrac{1}{\kappa_3} + \cfrac{\ddots}{\cfrac{1}{\kappa_{2n-1}} + \cfrac{1}{\cfrac{1}{s\kappa_{2n}}}}}}} \\ &= \left[0; \tfrac{1}{\kappa_1}, \tfrac{1}{s\kappa_2}, \tfrac{1}{\kappa_3}, \cdots, \tfrac{1}{\kappa_{2n-1}}, \tfrac{1}{s\kappa_{2n}}\right] \end{aligned} \tag{4.66}$$

where $\kappa_1 = L_{\mathrm{dc}} = V/(\boldsymbol{l}^\top \boldsymbol{r}) = V/(\boldsymbol{c}^\top K^{-1}\boldsymbol{b})$.

The other way to obtain the complex permeability $\langle \dot{\mu} \rangle$ is to use the average magnetization (4.55). The average magnetization can be written as

$$\begin{aligned} \overline{M} &= \mathrm{j}\omega \int_{\Omega_u} \sigma x A_z d\Omega \\ &= \mathrm{j}\omega \boldsymbol{c}^\top \boldsymbol{x} \\ &= \mathrm{j}\omega \boldsymbol{c}^\top (K + sN)^{-1} \boldsymbol{b} B_0 \end{aligned} \tag{4.67}$$

Substituting it to the definition of the complex permeability (4.55), we have

$$\langle \dot{\mu} \rangle = \frac{1}{1 - \mu_0 s \boldsymbol{c}^\top (K + sN)^{-1} \boldsymbol{b}}. \tag{4.68}$$

Applying the CVL algorithm 8, we obtain

$$\begin{aligned}\langle\dot{\mu}\rangle &= \frac{V}{\boldsymbol{l}^\top \boldsymbol{r} + s\boldsymbol{l}^\top (I - sA)^{-1} A\boldsymbol{r}} \\ &= \cfrac{1}{\cfrac{1}{\kappa_1} + \cfrac{1}{\cfrac{1}{s\kappa_2} + \cfrac{1}{\cfrac{1}{\kappa_3} + \cfrac{\ddots}{\cfrac{1}{\kappa_{2n-1}} + \cfrac{1}{\cfrac{1}{s\kappa_{2n}}}}}}}} \\ &= \left[0; \tfrac{1}{\kappa_1}, \tfrac{1}{s\kappa_2}, \tfrac{1}{\kappa_3}, \cdots, \tfrac{1}{\kappa_{2n-1}}, \tfrac{1}{s\kappa_{2n}}\right] \end{aligned} \tag{4.69}$$

Note that (4.55) can only applied to the unit cell consisted of a conductor whose permeability is $\mu_r = 1$.

4.2.2 Numerical result

Cylindrical conductor

The proposed method is applied to the analysis of a unit cell, $2w \times 2w$, each of which includes a cylinder of radius a. The relative permeability and conductivity of the conductor are assumed to be 1 and 5.76×10^7 S/m, respectively. The complex permeability is computed by (4.66) and semi-analytical method based on the extended Ollendorff formula. The results are plotted in Fig. 4.15. The horizontal axis denotes the radius normalized by the skin depth $\delta = \sqrt{2/\omega\sigma\mu}$. We consider five different values of the ratio a/w. The continued fraction is truncated at $n = 5$. The results obtained by the proposed method are in good agreement with those obtained by the semi-analytical method. The values in the continued fraction are summarized in Table 4.1 which are obtained by different representations of the complex permeability (4.66), (4.69) where $a/w = 0.5$.

In Fig. 4.16, we plotted the relative error between the complex permeability obtained by the proposed method and Ollendorff formula. The number of the stage is fixed at $n = 5$. When the proportion of the radius to the width of the unit cell is $a/w = 0.9$, we observe that the relative errors are approximately 4.0 % for the real part, and 10 % for the imaginary part, respectively. We consider that the discrepancy comes from the difference of the formulation. Since this argue has not been validated, the validation is our future work.

Rectangular conductor

The proposed method can treat the unit cell including arbitrary-shaped conductors which cannot be accurately modeled by the semi-analytical method. The complex permeability

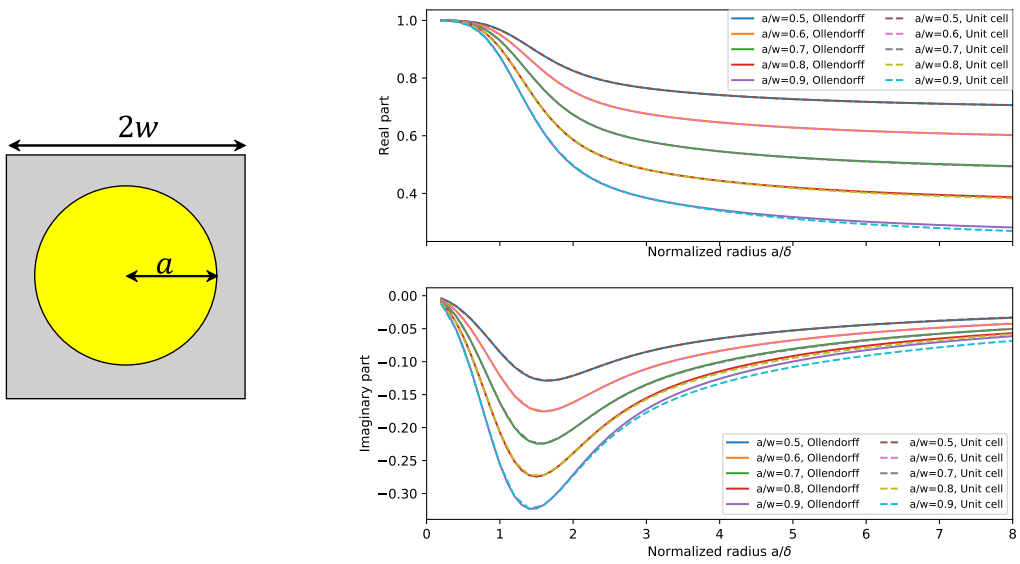

Figure4.15: Unit cell and dependence of the complex permeability on the normalized radius a/δ.

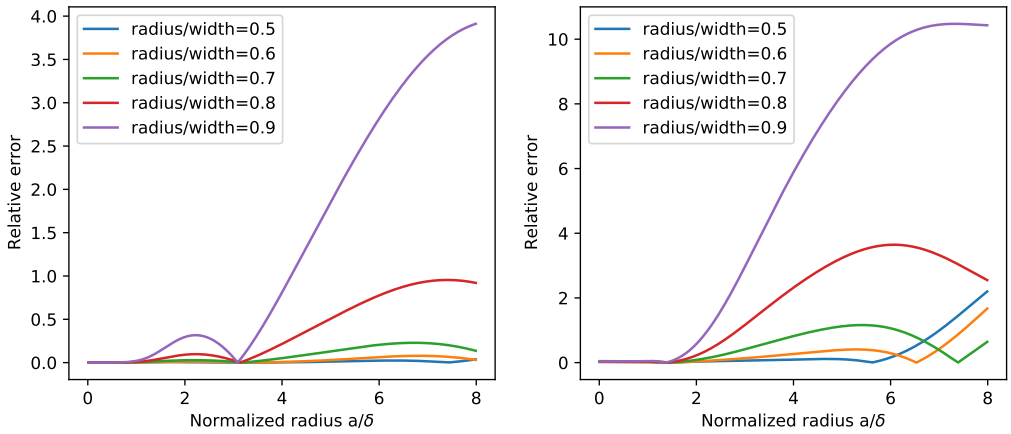

Figure4.16: The difference between the complex permeability obtained by the proposed method and Ollendorff formula.

Table4.1: Values in the continued fraction obtained by two representations of the complex permeability (cylinder $a/w = 0.5$).

	Average magnetization		Energy	
n	Odd term κ_{2n+1}	Even term κ_{2n+2}	Odd term κ_{2n+1}	Even term κ_{2n+2}
0	1.000×10^{0}	8.882×10^{-9}	1.000×10^{0}	8.883×10^{-9}
1	2.895×10^{0}	3.825×10^{-10}	2.895×10^{0}	3.817×10^{-10}
2	1.286×10^{1}	5.397×10^{-11}	1.291×10^{1}	5.364×10^{-11}
3	3.493×10^{1}	1.551×10^{-11}	3.527×10^{1}	1.303×10^{-11}
4	1.233×10^{3}	8.157×10^{-12}	7.496×10^{1}	4.316×10^{-12}

of a rectangular conductor computed by (4.66) is plotted against the frequency in Fig.4.17, where the complex permeability is anisotropic due to the rectangular conductor, which can be obtained by applying the uniform magnetic fields parallel to x and y axes independently. The values in the continued fraction are shown in Table 4.2.

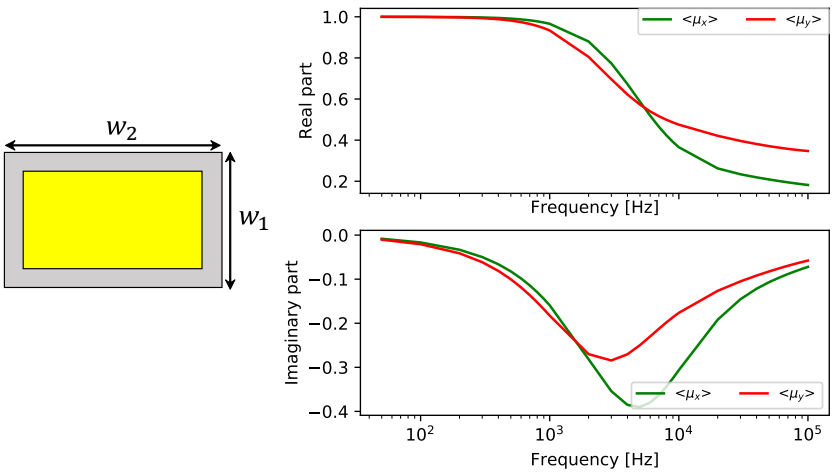

Figure4.17: Unit cell and dependence of the complex permeability on the frequency.

Elliptic conductor

The complex permeability of a elliptic conductor computed by (4.69) is plotted against the normalized frequency in Fig.4.18 and Fig.4.19, where the complex permeability is anisotropic due to the elliptic conductor, which can be obtained by applying the uniform magnetic fields parallel to x and y axes independently where $a/w = 0.9$. We consider five different values of the ratio b/w. The continued fraction is truncated at $n = 5$. The curves

Table4.2: Values in the continued fraction obtained by the representation of the energy (rectangular).

	$\langle\dot{\mu}_x\rangle_r$		$\langle\dot{\mu}_y\rangle_r$	
n	Odd term κ_{2n+1}	Even term κ_{2n+2}	Odd term κ_{2n+1}	Even term κ_{2n+2}
0	1.000×10^{0}	4.223×10^{-4}	1.000×10^{0}	2.530×10^{-4}
1	4.441×10^{-1}	5.364×10^{-5}	7.369×10^{-1}	3.213×10^{-5}
2	8.277×10^{-1}	1.030×10^{-5}	1.381×10^{0}	5.780×10^{-6}
3	1.732×10^{0}	2.826×10^{-6}	-7.016×10^{0}	-1.891×10^{-4}
4	3.286×10^{0}	8.729×10^{-7}	2.035×10^{0}	1.668×10^{-6}

for $b/w = 0.9$ is equivalent to that in Fig.4.15 for $a/w = 0.9$. The values in the continued fraction are shown in Table 4.3 where $a/w = 0.9, b/w = 0.5$.

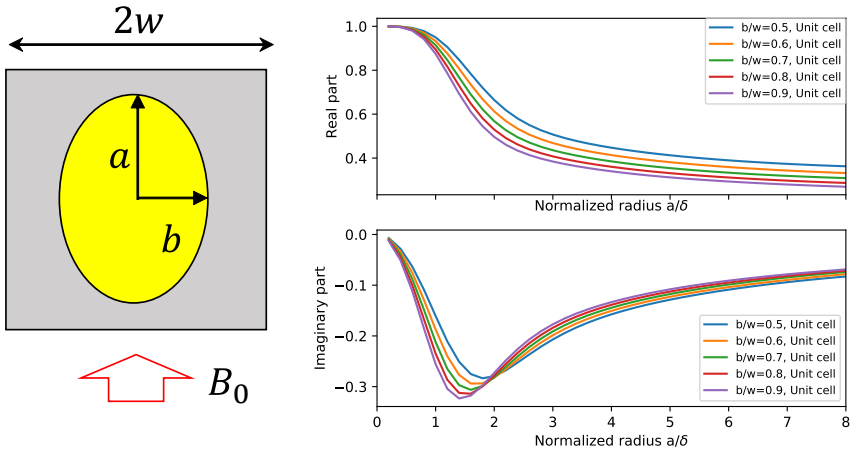

Figure4.18: Unit cell including elliptic conductor and frequency dependence of the complex permeability $\langle\dot{\mu}_y\rangle_r$.

Convergence analysis

As can be seen in Table 4.2, 4.3, the negative term appears in the latter term of the continued fraction. Since even terms $\kappa_{2n}, n = 1, 2, \ldots,$ are relatively small, we consider the negative terms are caused by the convergence criterion of the ICCG method and the discretization error of the unit cells. To verify these effects, we examine the changes in each term of the continued fraction by changing the convergence criterion and the size of the FE elements. In the following, we consider the case of the cylinder conductor

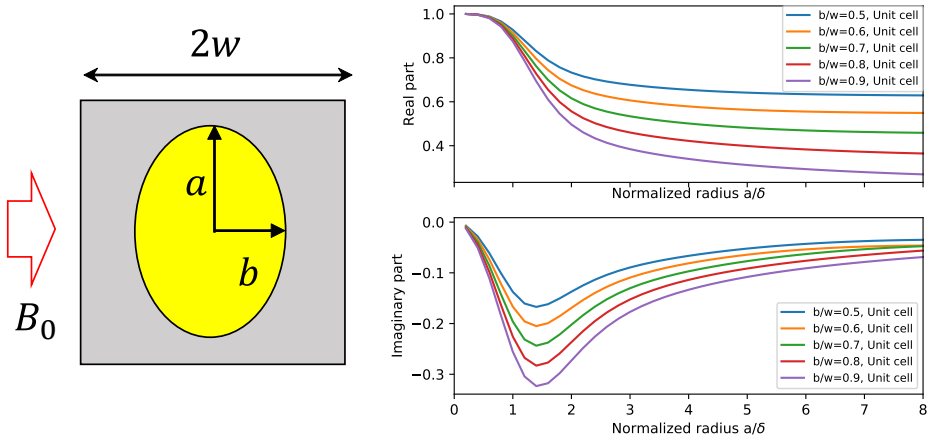

Figure4.19: Unit cell including elliptic conductor and frequency dependence of the complex permeability $\langle \dot{\mu}_x \rangle_r$.

Table4.3: Values in the continued fraction obtained by the representation of the average magnetization (ellipse, $a/w = 0.9, b/w = 0.5$).

	$\langle \dot{\mu}_y \rangle_r$		$\langle \dot{\mu}_x \rangle_r$	
n	Odd term κ_{2n+1}	Even term κ_{2n+2}	Odd term κ_{2n+1}	Even term κ_{2n+2}
0	1.000×10^{0}	1.598×10^{-8}	1.000×10^{0}	5.183×10^{-8}
1	2.000×10^{0}	6.960×10^{-10}	7.710×10^{-1}	6.625×10^{-9}
2	1.005×10^{1}	2.009×10^{-10}	1.663×10^{0}	1.592×10^{-9}
3	3.430×10^{1}	8.406×10^{-11}	3.402×10^{0}	5.506×10^{-10}
4	1.508×10^{2}	8.978×10^{-10}	5.976×10^{0}	-1.412×10^{-9}

whose ratio is $a/w = 0.6$. Table 4.4 summarizes the changes in the values of each term in the series of fractions when the convergence criterion of the ICCG method is varied as $\epsilon = 10^{-7}, 10^{-10}$, and 10^{-15} without changing the maximum element size 1.0μm. Table 4.4 shows that the value of κ_8 becomes positive when the criterion value is made more strict. This indicates that the influence of the convergence criterion appears in the latter stages of the Cauer circuit. However, the value of κ_9 is still negative even with a severe convergence criterion, which is considered to be the discretization error of the unit cell. Next, the same calculation was performed with the element size of 0.5μm to verify the effect of the unit cell discretization error. The results are summarized in Table 4.5. The results show that reducing the element size results in a positive value for κ_9. However, since negative values are found after κ_{10}, the effect of finite element discretization will

appear in the latter stages of the Cauer circuit.

Table4.4: Values of κ_n in continued fraction when $a/w = 0.6$. The convergence criterion is tested for $10^{-7}, 10^{-10}, 10^{-15}$ (maximum element size 1.0µm).

	$\epsilon = 10^{-7}$	$\epsilon = 10^{-10}$	$\epsilon = 10^{-15}$
n		κ_n	
1	1.000×10^{0}	1.000×10^{0}	1.000×10^{0}
2	1.842×10^{-8}	1.842×10^{-8}	1.842×10^{-8}
3	1.857×10^{0}	1.857×10^{0}	1.857×10^{0}
4	9.331×10^{-10}	9.333×10^{-10}	9.333×10^{-10}
5	7.443×10^{0}	7.440×10^{0}	7.440×10^{0}
6	1.368×10^{-10}	1.369×10^{-10}	1.369×10^{-10}
7	1.962×10^{1}	1.966×10^{1}	1.966×10^{1}
8	-1.092×10^{-13}	2.476×10^{-11}	2.476×10^{-11}
9	-4.467×10^{8}	-2.303×10^{8}	-2.304×10^{8}
10	1.089×10^{-13}	-9.532×10^{-11}	-9.531×10^{-11}

4.3 Finite element analysis of homogenization of Maxwell's equations

4.3.1 Formulation in frequency domain

Using the homogenization method, we can replace the microstructure by a homogeneous material. To obtain the eddy current losses, we solve the static Maxwell equations,

$$\nabla \times \nu \nabla \times \boldsymbol{A} = \boldsymbol{J}_0 \tag{4.70}$$

where the permeability is set to $\nu = \dot{\mu}^{-1}$ or $\nu = \langle \dot{\mu} \rangle^{-1}$ in the homogeneous material. The FE discretization results in

$$K(s)\boldsymbol{x} = \boldsymbol{b} \tag{4.71}$$

where the coefficient matrix $K(s) \in \mathbb{C}^{N \times N}$ depends on the complex frequency $s = \mathrm{j}\omega$. The complex power in the analysis domain can be computed by

$$P = \frac{\mathrm{j}\omega}{2} \int_\Omega \frac{|\boldsymbol{B}|^2}{\nu} d\Omega = \frac{\mathrm{j}\omega}{2} \int_\Omega \boldsymbol{A} \cdot \boldsymbol{J}_0 d\Omega. \tag{4.72}$$

The real part of the complex power represents the Joule losses due to the eddy currents in the homogeneous domain.

Table4.5: Values of κ_n in continued fraction when $a/w = 0.6$. The convergence criterion is tested for $10^{-7}, 10^{-10}, 10^{-15}$ (maximum element size 0.5µm).

	$\epsilon = 10^{-7}$	$\epsilon = 10^{-10}$	$\epsilon = 10^{-15}$
n		κ_n	
1	1.000×10^{0}	1.000×10^{0}	1.000×10^{0}
2	1.842×10^{-8}	1.842×10^{-8}	1.842×10^{-8}
3	1.857×10^{0}	1.857×10^{0}	1.857×10^{0}
4	9.328×10^{-10}	9.328×10^{-10}	9.328×10^{-10}
5	7.453×10^{0}	7.453×10^{0}	7.453×10^{0}
6	1.365×10^{-10}	1.365×10^{-10}	1.365×10^{-10}
7	1.980×10^{1}	1.980×10^{1}	1.980×10^{1}
8	3.408×10^{-11}	3.363×10^{-11}	3.363×10^{-11}
9	9.084×10^{1}	3.271×10^{1}	3.262×10^{1}
10	9.256×10^{-10}	-1.278×10^{-9}	-1.298×10^{-9}

4.3.2 Numerical result of frequency domain analysis

Let us consider an inductor consisted of an iron core and multi-turn coils. The multi-turn coil is composed of the round wires. The complex permeability of multi-turn coils can be computed by the proposed method. Here, the conductivity and relative permeability are assumed to be $\sigma = 5.76 \times 10^7$ S/m and $\mu_r = 1.0$. The full and homogenized inductor models are analyzed assuming that $a/\delta = 2$. In Fig.4.20, the flux lines are in good agreement although the coil region is not modeled in the homogenized model. As can be seen from Fig. 4.21, we do not have to generate the fine finite elements in the coil region. Therefore, the number of the total unknowns are reduced.

4.3.3 Formulation in time domain analysis

The homogenization method has a weak point that it is not straightforward to perform the time domain analysis because the complex permeability is a complex function formulated in the frequency-domain. The time-domain analysis is indispensable when quasi-static electromagnetic fields are analyzed considering the magnetic saturation. Although there are several methods of the time domain analysis of the homogenization method [100, 58], it depends on the low-frequency approximation of the complex permeability. Therefore, its accuracy would deteriorate as the driving frequency becomes higher.

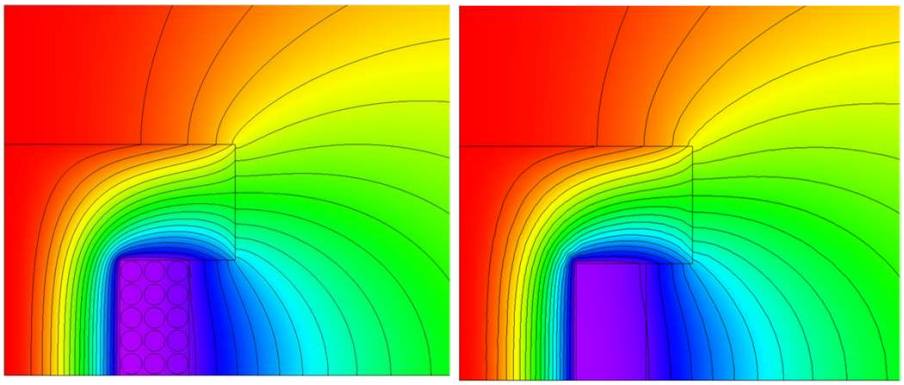

Figure4.20: Result of FEA of the full (right) and homogenized (left) models of an inductor.

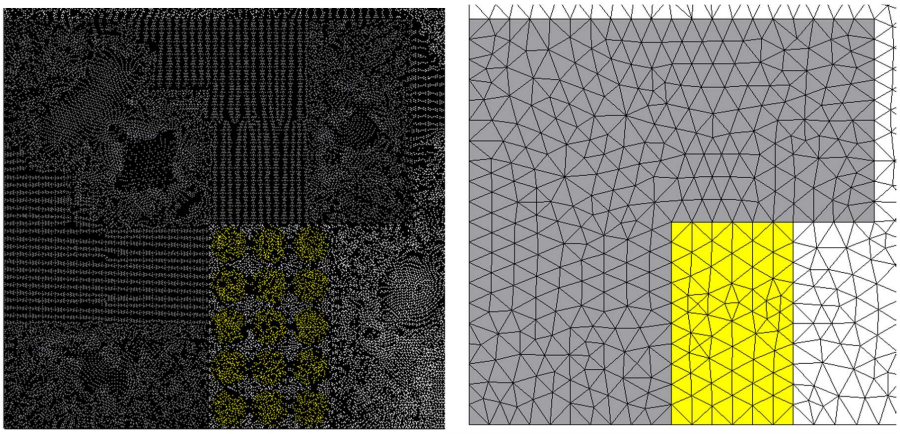

Figure4.21: Mesh configuration of the full (right) and homogenized (left) models of an inductor.

To overcome this difficulty, we represent the complex permeability by the Cauer circuit, which is accurate over a wide frequency range. In [60], the circuit equations for auxiliary unknowns coupled with the FE equation are solved simultaneously. Because the circuit equation is considered in all the finite elements in the homogenized region, a numerous auxiliary unknowns are involved. To solve this problem, we propose here a new method for the homogenization of Maxwell's equations in the time-domain that avoids the solution of the circuit equation in the transient computation.

Let us consider the analysis domain Ω including the homogeneous material Ω_{h}. The FE

equations depends on the complex permeability $\langle\dot{\mu}\rangle = \langle\dot{\nu}\rangle^{-1}$, can be written as

$$K(s)\boldsymbol{x} = \boldsymbol{b}I, \tag{4.73a}$$

$$(K(s)\boldsymbol{x})_i = \sum_j K_{ij}a_j = \sum_j \int_\Omega \nabla \times \boldsymbol{N}_i \cdot \nu\nabla \times \boldsymbol{N}_j d\Omega a_j, \tag{4.73b}$$

$$b_i = \int_\Omega \boldsymbol{N}_i \cdot \boldsymbol{j} d\Omega, \tag{4.73c}$$

where $K(s) \in \mathbb{C}^{N\times N}, \boldsymbol{x} \in \mathbb{C}^N, \boldsymbol{b} \in \mathbb{R}^N$ $\boldsymbol{j} \in \mathbb{R}^N, \boldsymbol{N}_i$, and I are the coefficient matrix, unknown vector whose j-th component is a_j, right hand vector, normalized current density defined so that $I\boldsymbol{j}$ corresponds to the current density, interpolation function and external current in the homogeneous material, respectively. In the homogeneous material, the permeability is set to $\nu = \langle\dot{\mu}\rangle^{-1}$. We convert (4.73) to the time-domain without introducing the auxiliary valuables. To do so, it is assumed that $\langle\dot{\mu}\rangle$ is expressed in the form of the continued fraction,

$$\langle\dot{\mu}\rangle = \left[0; \tfrac{1}{\kappa_1}, \tfrac{1}{s\kappa_2}, \tfrac{1}{\kappa_3}, \cdots, \tfrac{1}{\kappa_{2n-1}}, \tfrac{1}{s\kappa_{2n}}\right], \tag{4.74}$$

which can be obtained by the unit cell approach explained in the previous subsection. We obtain the time-domain representation by applying the inverse Laplace transform $\mathcal{L}^{-1}[\cdot]$ to both side of (4.73). Then, we evaluate the term $\mathcal{L}^{-1}[\langle\dot{\nu}\rangle a_j]$ by analogy with the circuit theory. We consider the correspondence $s\langle\dot{\mu}\rangle = \dot{Y}^{-1}$, $sa_j = \dot{V}$, $\langle\dot{\nu}\rangle a_j = \dot{I}$ where $\dot{Y}$, $\dot{V}$, and $\dot{I}$ are the admittance, current flowing $\dot{Y}$, and voltage across $\dot{Y}$, respectively. This analogy leads to the Cauer circuit shown in Fig. 3.11 because the continued fraction representation of $\dot{Y}$ corresponds to the admittance of the Cauer circuit. We readily obtain the circuit equations for the unknowns a_j as follows:

$$z_j(t) = \mathcal{L}^{-1}[\langle\dot{\nu}\rangle a_j] = \frac{a_j(t)}{\kappa_1} + z_1(t), \tag{4.75a}$$

$$\left(R + L\frac{d}{dt}\right)\boldsymbol{z}_j = \frac{da_j(t)}{dt}\boldsymbol{e}_1, \tag{4.75b}$$

$$R = \mathrm{diag}\left[\kappa_2^{-1}, \kappa_4^{-1}, \ldots, \kappa_{2n}^{-1}\right], \tag{4.75c}$$

$$L = \begin{bmatrix} \kappa_3 & -\kappa_3 & & \\ -\kappa_3 & \kappa_3+\kappa_5 & \ddots & \\ & \ddots & \ddots & -\kappa_{2n-1} \\ & & -\kappa_{2n-1} & \kappa_{2n-1} \end{bmatrix}. \tag{4.75d}$$

where $\boldsymbol{z}_j$ and $\boldsymbol{e}_1$ are the j-th auxiliary vector whose column is the loop currents in the Cauer circuit and the first column of the identity matrix I_n, respectively. By applying finite difference method to (4.75), we can express $\boldsymbol{z}_j$ at the n-th step in terms of the past

variables as

$$z_j^n = \frac{a_j^n}{\kappa_1} + z_1^n,$$
$$= \langle\nu\rangle a_j^n + \boldsymbol{e}_1^\top \left(R + \frac{1}{\Delta t}L\right)^{-1} \frac{-a_j^{n-1}\boldsymbol{e}_1 + L\boldsymbol{z}_j^{n-1}}{\Delta t}, \tag{4.76a}$$
$$\langle\nu\rangle = \left[\tfrac{1}{\kappa_1}; \tfrac{\Delta t}{\kappa_2}, \tfrac{1}{\kappa_3}, \cdots, \tfrac{1}{\kappa_{2n-1}}, \tfrac{\Delta t}{\kappa_{2n}}\right], \tag{4.76b}$$
$$\boldsymbol{z}_j^n = \left(R + \frac{1}{\Delta t}L\right)^{-1} \left(\frac{a_j^n - a_j^{n-1}}{\Delta t}\boldsymbol{e}_1 + \frac{1}{\Delta t}L\boldsymbol{z}_j^{n-1}\right) \tag{4.76c}$$

where Δt denotes the time difference. Note that the first-order accurate backward difference is applied to (4.75) whereas the second-order accurate backward difference is used in the numerical result. By inserting (4.76a) into the inverse Laplace transform of (4.73), we obtain the time-domain equation which does not include the auxiliary valuables as follows:

$$K\boldsymbol{x}^n = \boldsymbol{b}', \tag{4.77a}$$
$$(K\boldsymbol{x}^n)_i = \sum_j K_{ij} a_j^n = \sum_j \int_\Omega \nabla \times \boldsymbol{N}_i \cdot \nu \nabla \times \boldsymbol{N}_j d\Omega a_j^n, \tag{4.77b}$$
$$b_i' = b_i I^n + \sum_j \int_\Omega \nabla \times \boldsymbol{N}_i \cdot c_j^{n-1} \nabla \times \boldsymbol{N}_j d\Omega, \tag{4.77c}$$
$$c_j^{n-1} = \boldsymbol{e}_1^\top \left(R + \frac{1}{\Delta t}L\right)^{-1} \frac{-a_j^{n-1}\boldsymbol{e}_1 + L\boldsymbol{z}_j^{n-1}}{\Delta t}, \tag{4.77d}$$

where $\nu = \langle\nu\rangle$ in the homogeneous material Ω_h which can be obtained by simply replace s by Δt^{-1} in the continued fraction representation of the complex permeability. It is remarkable that the FE matrix in (4.77) has the same form as that in (4.73). Updating the right hand side vector, we can perform the time-domain analysis stepwise.

The terminal voltage can be computed from the interlink flux,

$$V = \frac{d}{dt}\int_\Omega \boldsymbol{A} \cdot \boldsymbol{j} d\Omega + R_{dc} I = \frac{d}{dt}\boldsymbol{b}^\top \boldsymbol{x} + R_{dc} I \tag{4.78}$$

where R_{dc} denotes the DC resistance of the winding. We can treat the voltage excitation by coupling (4.77) with (4.78).

In the frequency-domain, the complex power is expressed as

$$P = \frac{s}{2}\int_{\Omega_\mathrm{h}} \langle\dot{\nu}\rangle^* |\boldsymbol{B}|^2 d\Omega + \frac{s}{2}\int_{\Omega\setminus\Omega_\mathrm{h}} \nu |\boldsymbol{B}|^2 d\Omega + \frac{1}{2}R_{dc}I^2$$
$$= \frac{s}{2}\sum_{i,j\in\Omega_\mathrm{h}} \int_{\Omega_\mathrm{h}} \nabla \times \boldsymbol{N}_i \cdot \nabla \times \boldsymbol{N}_j d\Omega \langle\dot{\nu}\rangle^* a_i^* a_j + \frac{s}{2}\int_{\Omega\setminus\Omega_\mathrm{h}} \nu |\boldsymbol{B}|^2 d\Omega + \frac{1}{2}R_{dc}I^2. \tag{4.79}$$

Then, $s\langle\dot{\nu}\rangle^* a_i^* a_j$ are expanded as follows:

$$s\langle\dot{\nu}\rangle^* a_i^* a_j = s\frac{a_i^* a_j}{\kappa_1} + \boldsymbol{z}_i^\dagger (R + sL)\boldsymbol{z}_j \tag{4.80}$$

the first and second terms are real and purely imaginary because R and L are the symmetric matrices. Thus, the first term of (4.80) represents the Joule losses due to the eddy current. Consequently, we can compute the power dissipation in the time-domain from

$$W = \sum_{i,j \in \Omega_{\mathrm{h}}} \int_{\Omega_{\mathrm{h}}} \nabla \times \boldsymbol{N}_i \cdot (\boldsymbol{z}_i^{\top} R \boldsymbol{z}_j) \nabla \times \boldsymbol{N}_j d\Omega + R_{dc} I^2. \tag{4.81}$$

4.3.4 Numerical result of time domain analysis

Validation on proposed method: linear case

For validation, we apply the proposed method to the FE analysis of the axisymmetric inductor, which is composed of the multi-turn coil with 50 turns, wire radius 1 mm, and magnetic core, as shown in Fig. 4.22. The multi-turn coil is replaced by the homogeneous material whose complex permeability is in the form of the continued fraction, which represents the proximity effect in the coil. The number of the stage of the Cauer circuit is 5, which is summarized in Table. 4.6, and the relative permeability of the magnetic core is here assume to be 2000. A sinusoidal current, unit amplitude, at 1 MHz is input to the inductor. It is assumed that $\Delta t = 0.1[\mu\mathrm{s}]$, $T = 3.0[\mu\mathrm{s}]$. Although we can compute the eddy current losses due to the skin effect by introducing the equivalent skin effect impedance Z_{skin} [53], we ignore it in the analysis for simplicity.

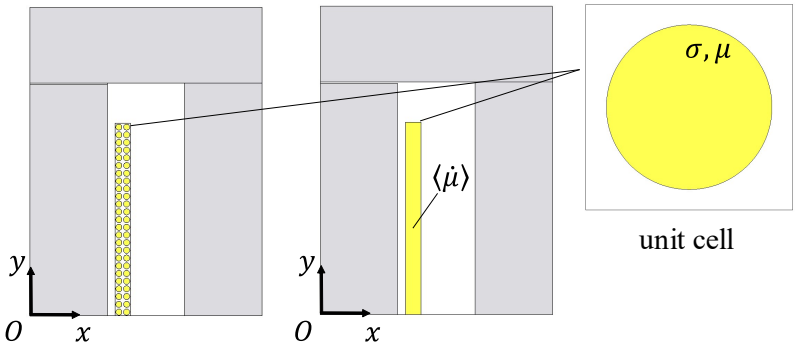

Figure4.22: Model configuration of the full (left) and homogeneous (right) models. ©2020IEEE

The power dissipation is plotted against time in Fig. 4.23. The relative error of the Joule losses per period is 1.2% at largest. There are 19,485 nodes and 9,845 elements in the conventional FE model, whereas 8,073 and 4,151 in the homogenized model. The computational time, 2 min 11 sec, for the conventional FEM is reduced to 1 min 7 sec for the proposed method. Since the proposed method does not include the auxiliary variables in the FE equation, we expect that its computational time is shorter than that of the method proposed in [60], where the FE equations are coupled with the Cauer circuit

Table4.6: Values in continued fraction which is obtained from unit cell in Fig. 4.22.

n	κ_{2n+1}	κ_{2n+2}
0	1.000×10^{0}	3.635×10^{-7}
1	8.246×10^{-1}	3.119×10^{-8}
2	2.244×10^{0}	5.569×10^{-9}
3	5.251×10^{0}	1.076×10^{-8}
4	1.040×10^{2}	1.762×10^{-9}

equations. The reduction in computational time by the proposed method becomes more significant for three-dimensional problems as will be shown below.

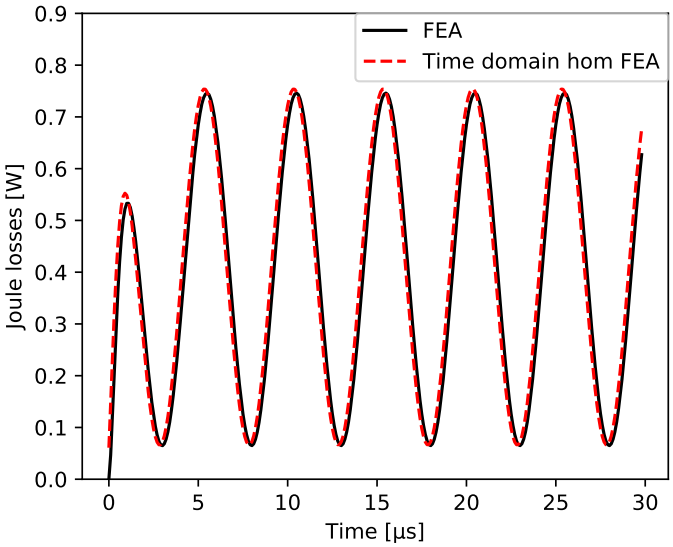

Figure4.23: Power dissipation versus time obtained with conventional and homogenization FEM. The magnetic core with constant permeability is considered with sinusoidal current input at 1MHz.

Validation on proposed method: nonlinear case

We apply the proposed method to the inductor considering the magnetic saturation. Since this problem only treats the eddy current losses in the winding, we can introduce the magnetic saturation in the usual way. If we consider the homogeneous material that has the nonlinear magnetic saturation, we can add the nonlinear current flux property in the first stage of the Cauer circuit [60]. The inductor is excited by the sinusoidal voltages, 200V

and 400V, at 100kHz. We assume that $\Delta t = 0.1[\mu s]$, $T = 30[\mu s]$. The time variation of the power dissipation is plotted in Fig. 4.24. The results obtained by the proposed method are in good agreement with those obtained by the conventional FEM. The waveform for 400V is deeply distorted by the magnetic saturation.

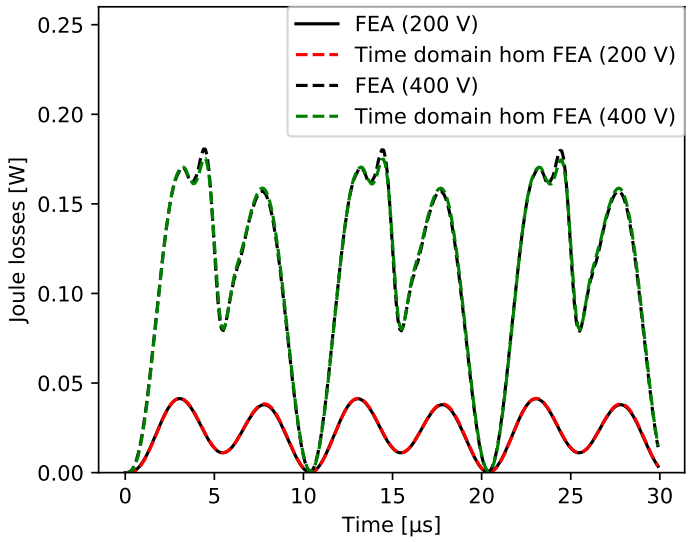

Figure4.24: Power dissipation versus time obtained with conventional and homogenization FEM. The saturable magnetic core is considered with sinusoidal voltage input at 100kHz.

Three-dimensional inductor model

The proposed method is applied to the three-dimensional inductor model, which has a homogeneous multi-turn coil, shown in Fig. 4.25. Due to the symmetry of the model, we model one-eights domain for FEA. The turn number and wire radius are the same as those in the two-dimensional model. We also consider the magnetic saturation in the magnetic core. It requires a heavy computational cost to analyze this model using conventional FEM. There would be more than 4,000,000 elements when we consider the skin depth at 100 kHz. On the other hand, the homogenized model requires only 173,866 elements and 210,676 edges. A pulsatile, 1V, at 100kHz, duty factor 0.5, shown in Fig. **??**, is input to the inductor. We assume that $\Delta t = 0.1[\mu s]$, $T = 30[\mu s]$. To conjunction with the external circuit, the FE equations is coupled with the circuit equation,

$$V = \frac{d}{dt}\boldsymbol{b}^{\top}\boldsymbol{x} + (R_{\rm dc} + R_{\rm load})I \tag{4.82}$$

where $R_{\rm load}$ is the load resistance. Here, we assume that $R_{\rm load} = 2[\Omega]$. The output current and the power dissipation are plotted against time in Fig. 4.26, respectively.

For comparison, the Joule losses of the inductor due to DC resistance is also plotted in Fig. 4.26. In periods $T \in [0,5],[10,15],[20,25]$, the current increases linearly and the DC loss has the quadratic increase whereas the Joule losses obtained by the proposed method has fairly complicated waveform due to the proximity effect. In periods $T \in [5,10],[15,20],[25,30]$ the current becomes constant, therefore, the Joule losses obtained by the proposed method has the nearly same value as the DC loss because there is no time variation in the electromagnetic field.

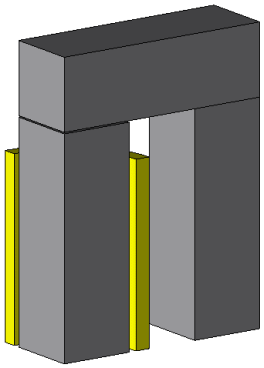

Figure4.25: Three-dimensional inductor one-eight model. ©2020IEEE

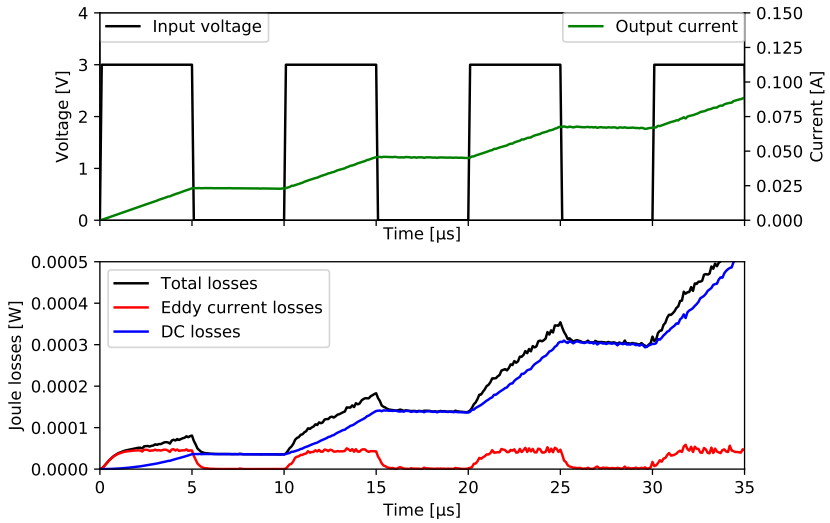

Figure4.26: Current and power dissipation versus time obtained with homogenization FEM. The inductor with a saturable magnetic core is excited by pulse voltage at 100kHz, duty factor 0.5, amplitude 3V.

4.4 Model order reduction and homogenization of Maxwell's equations

4.4.1 Formulation

Although the homogenization method is useful to reduce the computational cost, the time-domain analysis still requires a computational cost to solve the FE equation stepwise.

To tackle this problem, we propose here a new method that generates ROM from the homogenization of the Maxwell's equation. The resultant ROM corresponds to the equivalent circuit, which can easily be analyzed not only in the frequency domain but also in the time domain. Moreover, we can introduce the magnetic nonlinearity due to the core saturation to the equivalent circuit.

Let us consider the domain Ω including the homogeneous material Ω_{h} that has the macroscopic permeability $\langle\dot{\mu}\rangle$. We assume the linearity of the material. The governing equation is given as

$$K(s)\boldsymbol{x} = \boldsymbol{b}I, \tag{4.83a}$$

$$(K(s)\boldsymbol{x})_i = \sum_j K_{ij}a_j = \sum_j \int_\Omega \nabla\times\boldsymbol{N}_i\cdot\nu\nabla\times\boldsymbol{N}_j d\Omega a_j, \tag{4.83b}$$

$$b_i = \int_\Omega \boldsymbol{N}_i\cdot\boldsymbol{j}d\Omega, \tag{4.83c}$$

where $K(s)\in\mathbb{C}^{N\times N}, \boldsymbol{x}\in\mathbb{C}^N, \boldsymbol{b}\in\mathbb{R}^N$ $\boldsymbol{j}\in\mathbb{R}^N, \boldsymbol{N}_i$, and I are the coefficient matrix, unknown vector whose j-th component is a_j, right hand vector, normalized current density defined so that $I\boldsymbol{j}$ corresponds to the current density, interpolation function and external current in the homogeneous material, respectively. In the homogeneous material, the permeability is set to $\nu = \langle\dot{\mu}\rangle^{-1}$. The coefficient matrix K is a function of the complex permeability, that is, $K = K(\langle\dot{\mu}\rangle)$. If the complex permeability is expressed in the form of continued fraction,

$$\langle\dot{\mu}\rangle_r = \left[0; \tfrac{1}{\kappa_1}, \tfrac{1}{s\kappa_2}, \tfrac{1}{\kappa_3}, \cdots, \tfrac{1}{\kappa_{2n-1}}, \tfrac{1}{s\kappa_{2n}}\right], \tag{4.84}$$

which can be obtained by the unit cell approach explained in the previous subsection, we can write

$$K = K_1 + \chi(s)K_2, \tag{4.85a}$$

$$K_1 = K(0), \tag{4.85b}$$

$$K_{2ij} = \int_\Omega \nabla\times\boldsymbol{N}_i\cdot\nu\nabla\times\boldsymbol{N}_j d\Omega, \tag{4.85c}$$

$$\chi(s) = \left[0; \tfrac{1}{s\kappa_2}, \tfrac{1}{\kappa_3}, \cdots, \tfrac{1}{\kappa_{2n-1}}, \tfrac{1}{s\kappa_{2n}}\right] \tag{4.85d}$$

where $K(0)$ denotes the coefficient matrix of the static Maxwell equations. Note that $\nu = 1/\mu_0$ in the homogeneous material. The terminal voltage can be written as

$$\begin{aligned} V &= s\boldsymbol{b}^\top \boldsymbol{x} + Z_{\text{skin}} I \\ &= s\boldsymbol{b}^\top (K_1 + \chi K_2)^{-1} \boldsymbol{b} I + Z_{\text{skin}} I. \end{aligned} \tag{4.86}$$

where Z_{skin} is the impedance relevant to the skin effect in the coil. If we consider the round wire, it can be written as [53]

$$\begin{aligned} Z_{\text{skin}} &= R_{\text{dc}} \frac{z J_0(z)}{2 J_1(z)} \\ &= \left[R_{\text{dc}}; \frac{1}{\kappa_{s1}}, \frac{1}{s\kappa_{s2}}, \cdots, \frac{1}{\kappa_{s2m-1}}, \frac{1}{s\kappa_{s2m}} \right] \end{aligned} \tag{4.87}$$

where R_{dc} is the DC resistance of the wire. The impedance of the system can be written as

$$Z = s\boldsymbol{b}^\top (K_1 + \chi K_2)^{-1} \boldsymbol{b} + Z_{\text{skin}} \tag{4.88}$$

where the first term represents the eddy current losses due to the homogeneous materials. By applying the CVL algorithm 8 to the first term of the impedance, we get

$$Z = \left[0; \frac{1}{s\kappa_{h1}}, \frac{s}{\chi\kappa_{h2}}, \cdots, \frac{1}{s\kappa_{h2l-1}}, \frac{s}{\chi\kappa_{h2l}} \right] + \left[R_{\text{dc}}; \frac{1}{\kappa_{s1}}, \frac{1}{s\kappa_{s2}}, \cdots, \frac{1}{\kappa_{s2m-1}}, \frac{1}{s\kappa_{s2m}} \right] \tag{4.89}$$

where $\lambda_n, n = 1, 2, \ldots, 2l$ are the parameters obtained from the CVL algorithm. Since

$$\begin{aligned} \frac{s}{\chi\lambda_{2l}} &= \frac{1}{\kappa_{h2l}} \left[\frac{1}{\kappa_2}; \frac{1}{s\kappa_3}, \cdots, \frac{1}{s\kappa_{2n-1}}, \frac{1}{\kappa_{2n}} \right] \\ &= \left[\frac{1}{\kappa_{h2l}\kappa_2}; \frac{\kappa_{h2l}}{s\kappa_3}, \cdots, \frac{\kappa_{h2l}}{s\kappa_{2n-1}}, \frac{1}{\kappa_{h2l}\kappa_{2n}} \right] \end{aligned} \tag{4.90}$$

has the same topology as the Cauer circuit 3.4, we can express the impedance as the equivalent circuit shown in Fig. 4.27. The equivalent circuit has a hierarchical structure that is composed of the Cauer circuits. The upper and lower part of the circuit corresponding to the eddy current due to the homogeneous material, and skin effect, respectively. When we consider the multi-turn coil, the upper part represents the proximity effect. Therefore, we express multiple physical phenomena in the equivalent circuit separately.

From the structure of the equivalent circuit, we observe that the currents which flow in the higher stages of the equivalent circuit vanish in the stationary limit $\omega \to 0$. Thus, the currents only flow in the primary inductor of the first stage. It means that the primary inductor represents the magnetostatic property of the system. Based on this physical interpretation of the equivalent circuit, the primary inductor is replaced with the pre-computed current-flux property to express magnetic saturation, as shown in Fig. 4.28. We can compute the property by solving the nonlinear static Maxwell equations in advance.

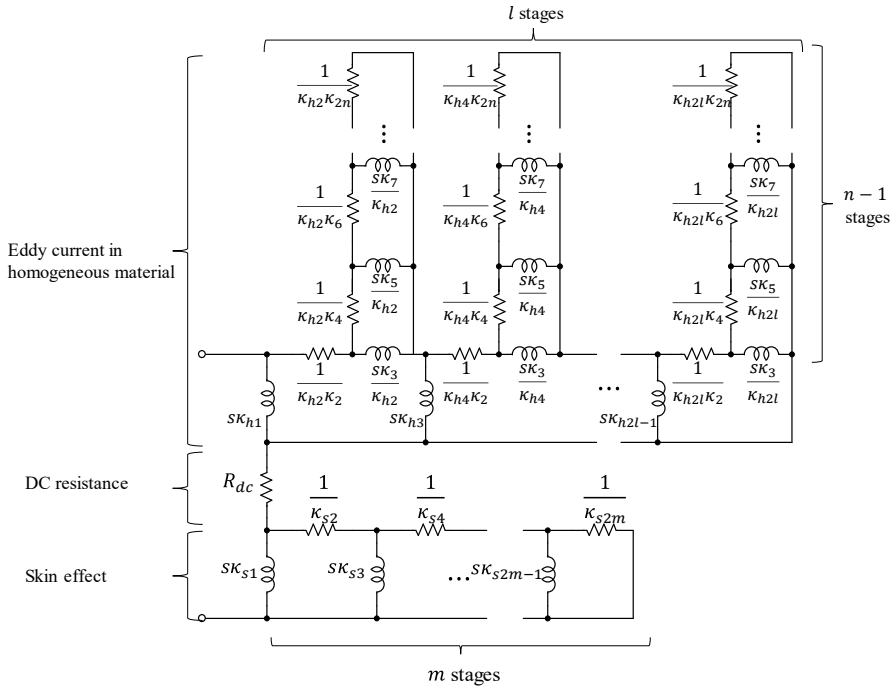

Figure4.27: Reduced-order model of the homogenization of Maxwell's equation.

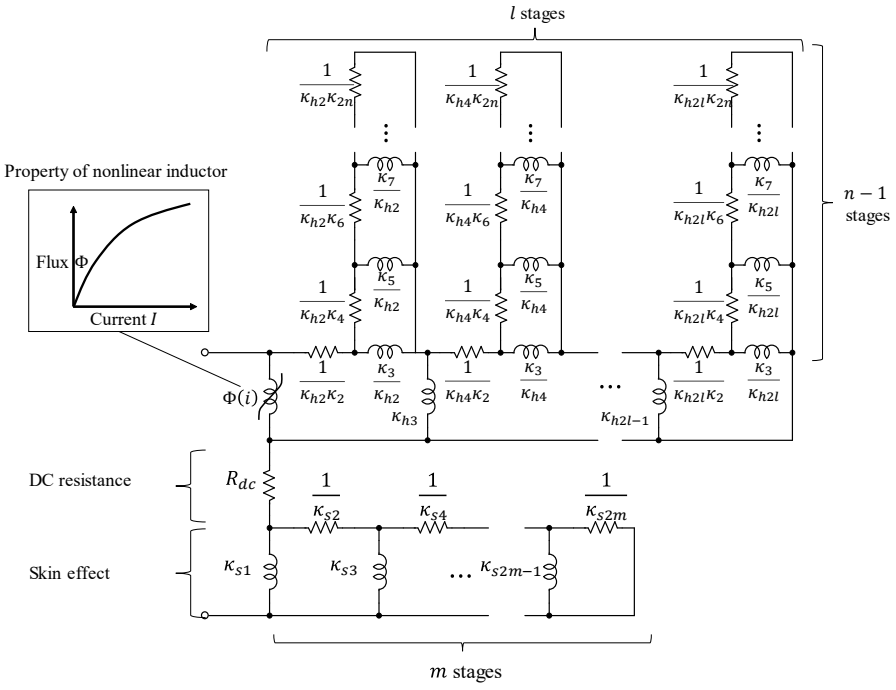

Figure4.28: Nonlinear reduced-order model of the homogenization of Maxwell's equation.

Note that this method is valid when the following two assumptions hold for the equivalent circuit.

1. The eddy currents have little effect on the magnetic field. And the main flux is well governed by the static Maxwell equations.
2. The circuit parameters in the higher stages, which represent the effect of the eddy currents, do not change by the nonlinear saturation. This assumption is valid when the magnetic field distribution and skin depth have little changes due to the magnetic saturation.

4.4.2 Numerical result

Validation on proposed method: linear case

Let us consider the axisymmetric reactor consisted of the homogeneous multi-turn coil and linear magnetic core, shown in Fig. 4.29. The model is homogeneous version of the reactor shown in Fig. 3.14. The specification of the multi-turn coil is summarized in Table 4.7. We assume that the relative permeability of the magnetic material is 950, the initial permeability of NL40S, and R_{dc} is set to 0.679Ω.

By applying the proposed method, we obtain the circuit parameters in Fig. 4.27. Each continued fraction is truncated at $l, m, n = 5$. All circuit parameters are summarized in 4.8. To validate the proposed method, we compare the frequency characteristic of the impedance obtained by the proposed method with that obtained by the conventional FEM. The impedance is plotted in Fig. 4.30 against the normalized radius a/δ. The result obtained by the proposed method is in good agreement with that obtained by conventional FEM. The discrepancy between the full and homogeneous model may be caused by the air gap. The linkage flux is not uniform around the air gap, and thus the assumed uniformity in the field is partially broken there. Note that this discrepancy is not due to the proposed method but to the homogenization method.

Now we can perform the time-domain analysis of the simple series circuit of DC resistance and linear DC inductance (DC model) and proposed linear equivalent circuit and conventional FEM. A source voltage has the pulse width modulation (PWM) excitation with 200 kHz, 5V carrier, as shown in Fig. 4.31. The Joule losses are plotted against the time in Fig. 4.31. The proposed equivalent circuit can accurately evaluate the eddy currents whereas the DC model cannot represent the eddy currents. The whole computational time, which is composed of the construction of the equivalent circuit and time-domain analysis, is 46.2 seconds (CPU: Intel Core i7-7700@3.6GHz, RAM: 8.00 GB), whereas it takes about 31 hours to perform the conventional FE analysis under the same environment.

Table4.7: Specification of multi-turn coil

Shape of conductor	Cylindrical wire
Radius a	0.175[mm]
Filling ratio η	0.601
Conductivity σ	5.76×10^7 [S/m]
Relative permeability μ_r	1
Turn number	50
Connection of winding	Series-connection

Table4.8: Values in equivalent circuit of the two-dimensional reactor obtained from homogenization FEA, skin effect impedance, and unit cell analysis.

	Homogenizaiton $\boldsymbol{b}^\top(K_1+\chi K_2)^{-1}\boldsymbol{b}$		Skin effect Z_{skin}		Unit cell $\langle\dot{\mu}\rangle_r$	
l,m,n	κ_{h2l-1}	κ_{h2l}	κ_{s2m-1}	κ_{s2m}	κ_{2n-1}	κ_{2n}
1	4.523×10^{-3}	7.198×10^{0}	1.633×10^{-6}	4.910×10^{-1}	1.000×10^{0}	2.660×10^{-7}
2	1.029×10^{-1}	4.343×10^{-1}	8.164×10^{-7}	2.946×10^{-1}	8.878×10^{-1}	2.060×10^{-8}
3	1.138×10^{0}	1.800×10^{-1}	5.443×10^{-7}	2.104×10^{-1}	2.722×10^{0}	3.440×10^{-9}
4	6.733×10^{-1}	9.322×10^{-1}	4.082×10^{-7}	1.637×10^{-1}	6.472×10^{0}	8.610×10^{-10}
5	3.068×10^{-2}	2.310×10^{-1}	3.266×10^{-7}	1.339×10^{1}	1.384×10^{-1}	3.000×10^{-10}

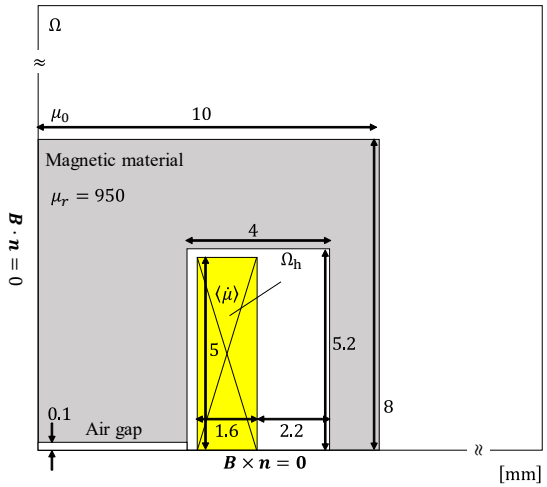

Figure4.29: Axisymmetric reactor consisted of homogeneous multi-turn coil and magnetic core.

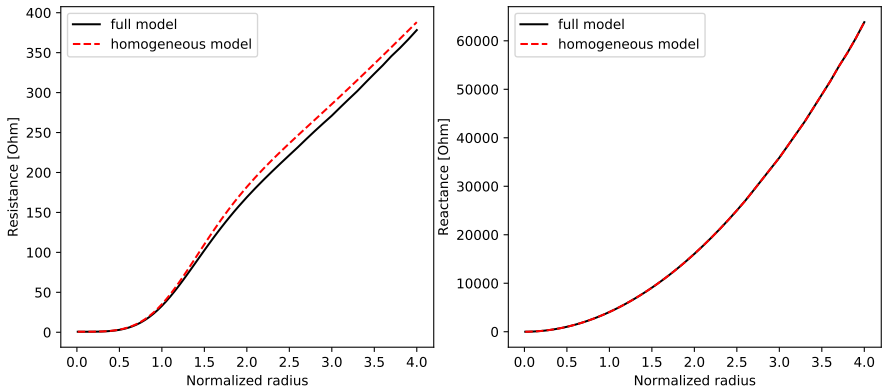

Figure4.30: Frequency profile of the two-dimensional reactor model.

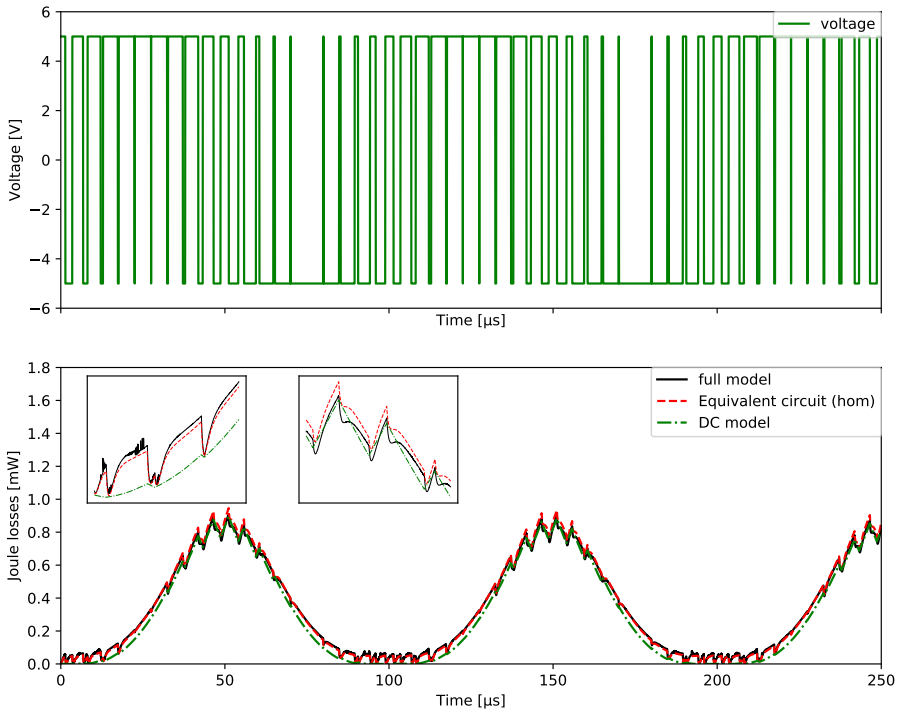

Figure4.31: Temporal changes in voltage and Joule losses obtained by the simple series circuit of DC resistance and inductance (DC model), and proposed linear equivalent circuit and FEM excited by PWM with 200 kHz, 5 V carrier.

Validation on proposed method: nonlinear case

Next, we perform the nonlinear analysis in the time-domain using the proposed equivalent circuit and conventional FEM for the PWM excitation with 200 kHz, 75 V carrier. In this case, we replace the core material with NL40S to consider the nonlinear magnetic saturation. The current flux characteristic is pre-computed by solving the nonlinear static Maxwell equations, which is shown in Fig. 4.32. The Joule losses are plotted against the time in Fig.4.33. We find the excellent correspondence between the results obtained by the proposed method and FEM. We also find that both waveforms are distorted by saturation in contrast to that obtained by the DC model.

Three-dimensional reactor model

Let us consider a one-eighth model of a reactor model consisted of a homogeneous multi-turn coil and magnetic core, as shown in Fig. 4.34. Note that it is difficult to analyze the eddy current loss of this model by the conventional FEM because this three-dimensional model contains fine windings which result in numerous finite elements. The material specification is the same as the two-dimensional reactor model provided in Table 4.7. We compute the current-flux characteristic by solving the static Maxwell equations, as shown in Fig. 4.36. The circuit parameters are summarized in Table 4.9. Since the unknowns of the synthesized equivalent circuit are much less than that of the original model, we can incorporate the equivalent circuit into a circuit simulator. In this study, we assemble it into the buck-boost converter. The circuit topology is illustrate in Fig. 4.35 where the capacitance and resistance are 200µF and 20Ω, respectively. Fig. 4.37 shows the time response of the terminal voltage of the linear and nonlinear equivalent circuit obtained by the proposed method. The differences between responses of the linear and nonlinear equivalent circuits. Also, we can compute the eddy current loss from the equivalent circuit. Since we can obtain the time response of the electromagnetic apparatuses considering the eddy currents at high speed, we consider that it is useful for the design considering the various operating conditions.

4.5 Extension of Dowell's method

To show the advantage of the Cauer representation, we apply the complex permeability in the form of the continued fraction to the evaluation of the eddy current losses due to the proximity effect in a copper winding. It is important to evaluate the eddy current losses due to the proximity effect for the design of high-frequency (HF) transformers, resonant inductors, motor windings. Although Dowell's method has been widely used to evaluate the eddy current losses, it has been pointed out that the accuracy deteriorates in

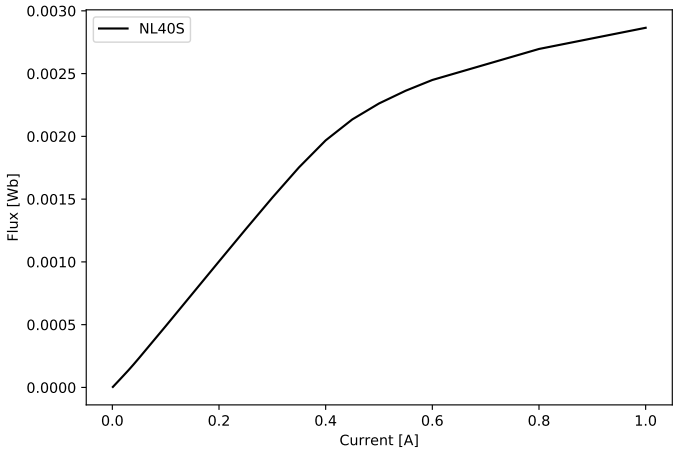

Figure4.32: Current-flux characteristic of the two-dimensional reactor which is pre-computed by solving the static Maxwell equations.

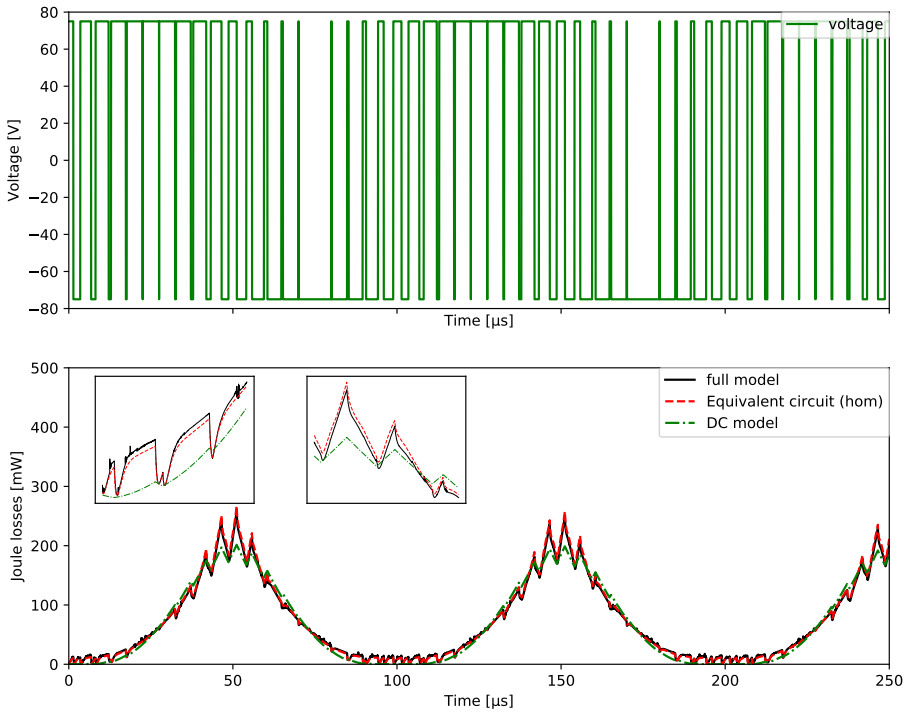

Figure4.33: Temporal changes in voltage and Joule losses obtained by the simple series circuit of DC resistance and inductance (DC model), and proposed nonlinear equivalent circuit and FEM excited by PWM with 200 kHz, 75 V carrier.

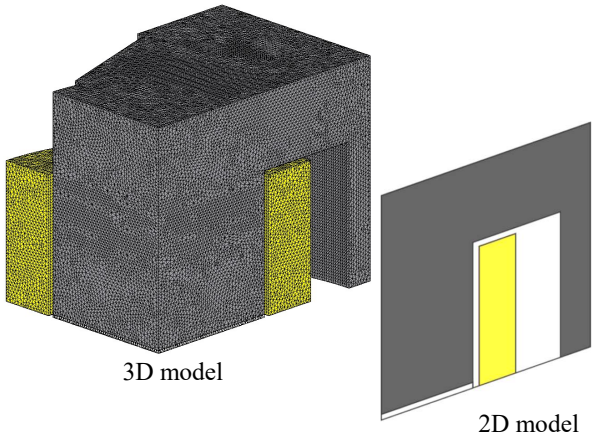

Figure4.34: Three-dimensional reactor consisted of homogeneous multi-turn coil and magnetic core.

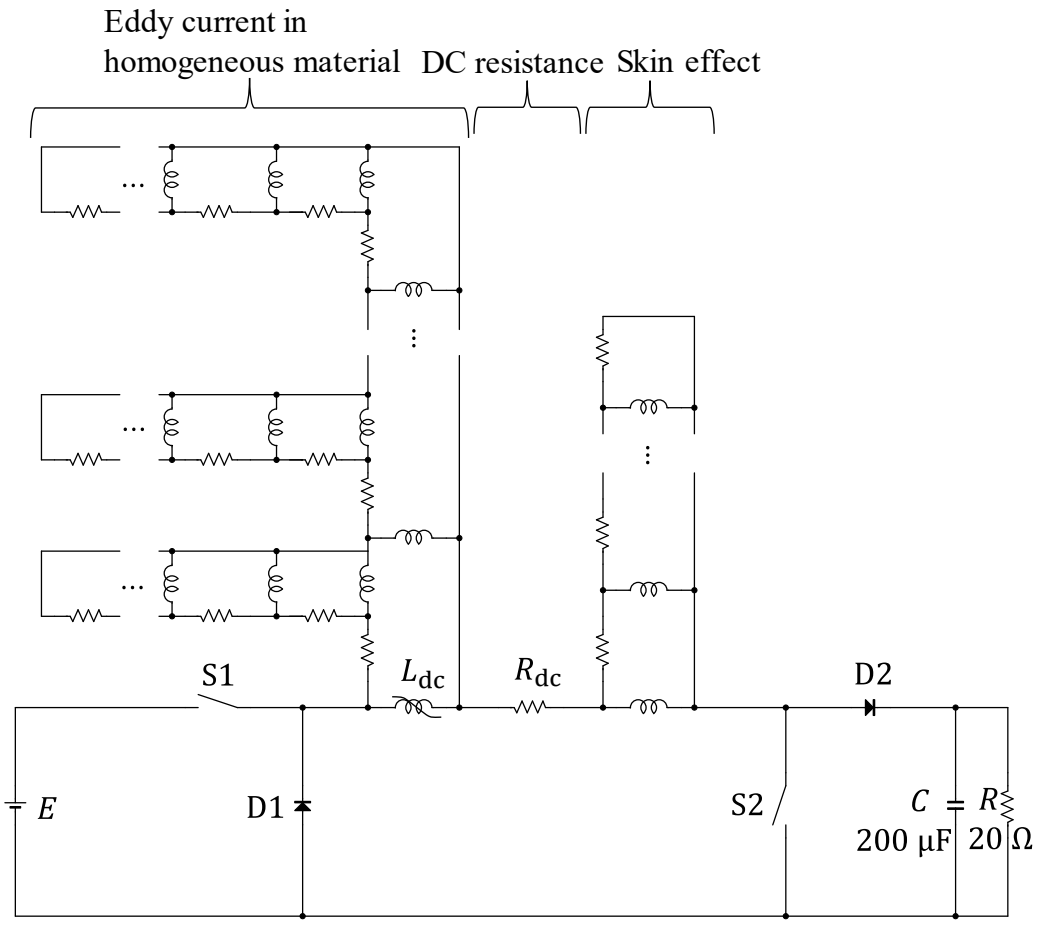

Figure4.35: Buck-boost converter circuit considering skin and proximity effects in the winding.

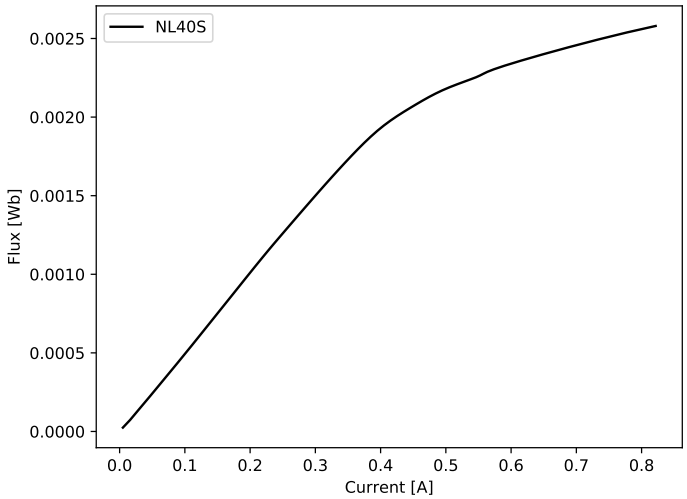

Figure4.36: Current-flux characteristic of the three-dimensional reactor which is pre-computed by solving the static Maxwell equations.

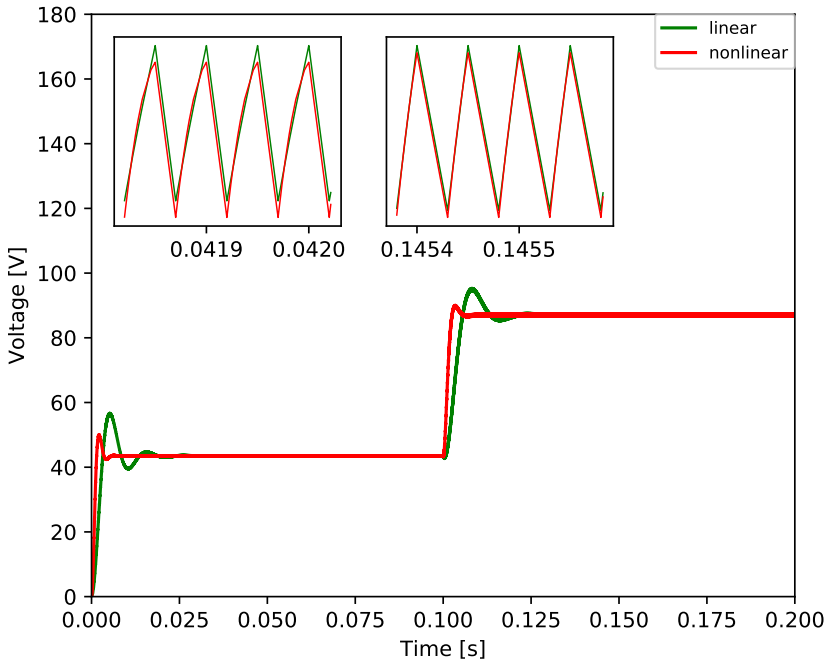

Figure4.37: Response of the voltage of the buck-boost converter.

Table4.9: Values in equivalent circuit of three-dimensional reactor obtained from homogenization FEA, skin effect impedance, and unit cell analysis.

	Homogenizaiton $\boldsymbol{b}^\top(K_1+\chi K_2)^{-1}\boldsymbol{b}$		Skin effect Z_{skin}		Unit cell $\langle\dot{\mu}\rangle_r$	
l,m,n	κ_{h2l-1}	κ_{h2l}	κ_{s2m-1}	κ_{s2m}	κ_{2n-1}	κ_{2n}
1	4.967×10^{-3}	5.694×10^{0}	1.110×10^{-6}	4.910×10^{-1}	1.000×10^{0}	2.660×10^{-7}
2	1.366×10^{-1}	3.406×10^{-1}	5.540×10^{-7}	2.946×10^{-1}	8.878×10^{-1}	2.060×10^{-8}
3	1.484×10^{0}	7.524×10^{-2}	3.690×10^{-7}	2.104×10^{-1}	2.722×10^{0}	3.440×10^{-9}
4	5.276×10^{0}	3.322×10^{-2}	2.770×10^{-7}	1.637×10^{-1}	6.472×10^{0}	8.610×10^{-10}
5	1.008×10^{1}	1.641×10^{-2}	2.220×10^{-7}	1.339×10^{-1}	1.384×10^{1}	3.000×10^{-10}

high-frequency. In this part, we propose a new method and validate it.

Let us consider the copper winding and homogeneous winding Ω_{h}, as shown in Fig. 4.38. The copper winding consists of $z_a \times z_t$-turn sub-conductors and is inserted in a slot whose permeability is infinite. The width and height of the sub-conductors and homogeneous winding are b_{c0}, h_{c0}, $b_c = z_a b_{\text{unit}}$ and $h_c = z_t h_{\text{unit}}$, respectively, where b_{unit} and h_{unit} are the width and height of the unit cell. Alternative current I parallel to z-axis flows in each conductor. The current density and net current in the homogeneous winding are J and $\int_{\Omega_h} JdS = z_a z_t I$, respectively.

From Dowell's method, the average resistance factor $k = R_{\text{ac}}/R_{\text{dc}}$ of the winding at frequency ω can be evaluated from

$$k = \zeta\frac{\sinh 2\zeta + \sin 2\zeta}{\cosh 2\zeta - \cos 2\zeta} + 2\zeta\frac{z_t^2-1}{3}\frac{\sinh\zeta - \sin\zeta}{\cosh\zeta + \cos\zeta}, \tag{4.91}$$

$$\zeta = h_{c0}\sqrt{\frac{1}{2}\omega\sigma\mu\frac{z_a b_{c0}}{b}} \tag{4.92}$$

where σ, μ are the conductivity and permeability, respectively. Note that this approach can be inaccurate when its main assumptions that the magnetic field is one-dimensional and the eddy currents in the sub-conductors have no influence on the global field do not hold.

Though the proposed method is available for 2D and 3D models, it is applied to the simple model shown in Fig. 4.38 for comparison. The permeability of the homogeneous winding $\langle\dot{\mu}\rangle$ can be computed from the unit cell approach. Using the proposed method, the impedance and resistance factor of the homogenized winding are expressed as

$$Z = z_a z_t R_{\text{dc}} + \text{j}\omega\langle\dot{\mu}_x\rangle\frac{h_c b_c l z_a^2 z_t^2}{3b^2}, \tag{4.93}$$

$$k = \frac{\text{Re}[Z]}{z_a z_t R_{\text{dc}}} = 1 - \text{Im}[\langle\dot{\mu}_x\rangle]\frac{\omega h_c b_c l z_a z_t}{3b^2 R_{\text{dc}}} \tag{4.94}$$

where l denotes the length of the sub-conductors. The DC resistance of a sub-conductor can be computed as $R_{\rm dc} = l/\sigma h_{\rm c0} b_{\rm c0}$. (4.93) is obtained by solving the one-dimensional equation for magnetostatic field while the two-dimensional structure is reflected in $\langle \dot{\mu}_x \rangle$, see Appendix B.

To validate the proposed model, we consider the winding shown in Fig. 4.39 for $h_{c0} = 2.38$mm, $b_{c0} = 10$mm, $b_c = 14$mm, $z_a = 1$, $z_t = 12$, $h_{\rm unit} = 2.38$mm, $b_{\rm unit} = 12$mm, and $\sigma = 5.76\times10^7$S/m. The resistance factors are computed by Dowell's method, proposed method and FEM shown in Fig. 4.40. In the FE analysis, we apply the homogeneous Neumann boundary condition to the boundary of the iron core. When frequency is relatively low, the three results are in good agreement. However, the conventional resistance factor evaluated from Dowell's method has discrepancies from the other two results as frequency increases. We consider that the discrepancies between the proposed method and FEA are caused because the assumption of the uniformity of the magnetic fields is locally broken at the edge of the sub-conductors.

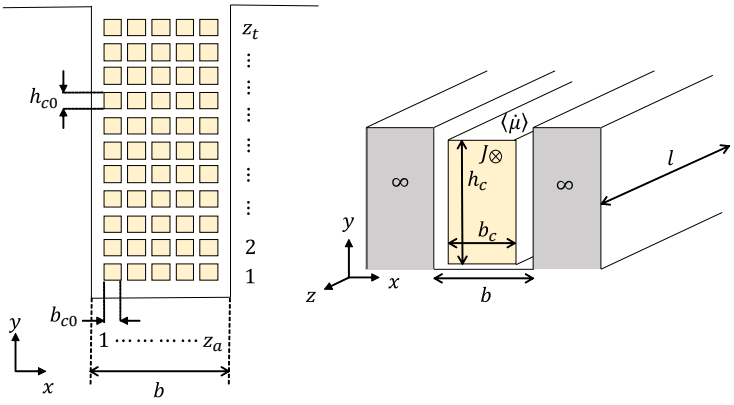

Figure4.38: Copper winding inserted in a slot whose permeability is infinite. The sub-conductors are connected in series. Left and right figures show the non-homogeneous and homogeneous windings. ©2020IEEE

The equivalent circuit of the winding can be developed by (4.93) because the complex permeability is represented by the continued fraction. The impedance of the winding can be written as follows:

$$Z = = \left[z_a z_t R_{\rm dc}; \frac{1}{sc\kappa_1}, \frac{c}{\kappa_2}, \cdots, \frac{1}{sc\kappa_{2n-1}}, \frac{c}{\kappa_{2n}} \right] \tag{4.95}$$

where $c = h_c b_c l z_a^2 z_t^2 / 3b^2$. Considering more general cases such as interleaved transformer winding, the equivalent circuit can be obtained by using magnetomotive force (m.m.f.) diagram which is utilized in Dowell's method. Analyzing the equivalent circuit by the circuit simulator, we can evaluate the eddy current losses even when the non-sinusoidal

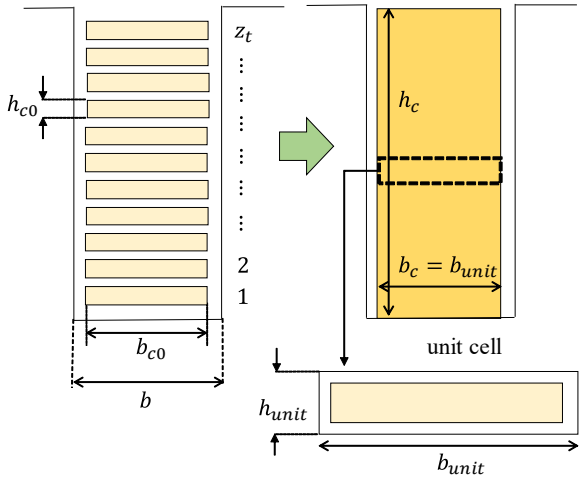

Figure4.39: Validation model. ©2020IEEE

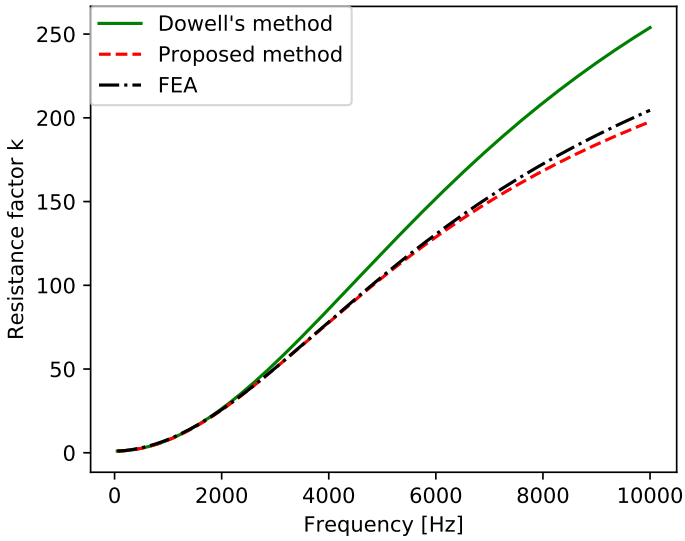

Figure4.40: Frequency characteristic of the resistance factor $k = R_{\mathrm{ac}}/R_{\mathrm{dc}}$.

current flows in the conductors.

Chapter 5.

Darwin model and model order reduction

5.1 Formulation

Let us consider a simple connected domain $\Omega = \Omega_{\mathrm{c}} + \Omega_{\mathrm{e}}$ where Ω_{c} and Ω_{e} is the conductive domain and non-conducting domain. Note that the non-conducting domain Ω_{e} does not include the boundary $\partial\Omega_{\mathrm{c}}$, i.e., $\Omega_{\mathrm{e}} = \Omega \setminus \overline{\Omega_{\mathrm{c}}}$. The boundary $\partial\Omega = \Gamma$ can be divided into three non-overlapping parts $\Gamma_0, \Gamma_1, \Gamma_{\mathrm{D}}$. We assume that the power supply is connected to the boundaries Γ_0, Γ_1. We consider the $A - \phi$ formulation of the Darwin model of Maxwell's equations in the complex phasor notation,

$$\nabla \times \nu \nabla \boldsymbol{A} + \sigma(\mathrm{j}\omega \boldsymbol{A} + \nabla\phi) + \mathrm{j}\omega\epsilon\nabla\phi = 0, \tag{5.1}$$

$$\nabla \cdot \sigma\Big(\mathrm{j}\omega \boldsymbol{A} + \nabla\phi\Big) + \mathrm{j}\omega\nabla \cdot \epsilon\nabla\phi = 0. \tag{5.2}$$

where $\mu, \sigma, \epsilon, \omega, \nu$ are the permeability, conductivity, permittivity, angular frequency, and magnetic resistivity. Note that $\sigma = 0$ in non-conductive domain, and $\epsilon = \epsilon_0$ in conductive domain where ϵ_0 is the vacuum permittivity. The boundary conditions are given as

$$\boldsymbol{A} \times \boldsymbol{n} = \boldsymbol{0}, \quad \phi = lU, \quad \text{on } \Gamma_l, l = 0, 1, U \in \mathbb{C}, \quad \text{(PEC)} \tag{5.3}$$

$$\boldsymbol{B} \cdot \boldsymbol{n} = 0, \quad \boldsymbol{D} \cdot \boldsymbol{n} = 0, \quad \text{on } \Gamma_{\mathrm{D}}, \quad \text{(Symmetric boundary)} \tag{5.4}$$

The FE discretization results in

$$\left(\begin{bmatrix} K & L_\sigma \\ 0 & M_\sigma \end{bmatrix} + \mathrm{j}\omega \begin{bmatrix} N & L_\epsilon \\ L_\sigma^\top & M_\epsilon \end{bmatrix} \right) \begin{bmatrix} \boldsymbol{a} \\ \boldsymbol{\phi} \end{bmatrix} = \begin{bmatrix} \boldsymbol{0} \\ \boldsymbol{0} \end{bmatrix} \tag{5.5}$$

where

$$(K)_{ij} = \int_{\Omega} \nabla \times \boldsymbol{w}_i^e \cdot \nu \nabla \times \boldsymbol{w}_j^e d\Omega, \tag{5.6}$$

$$(N)_{ij} = \int_{\Omega_c} \boldsymbol{w}_i^e \cdot \sigma \boldsymbol{w}_j^e d\Omega, \tag{5.7}$$

$$(L_\chi)_{ij} = \int_{\Omega} \boldsymbol{w}_i^e \cdot \chi \nabla w_j^n d\Omega, \tag{5.8}$$

$$(M_\chi)_{ij} = \int_{\Omega} \nabla w_i^n \cdot \chi \nabla w_j^n d\Omega. \tag{5.9}$$

Note $\boldsymbol{w}_i^e, w_i^n$ denote the i-th edge element, and i-th node interpolation function, respectively, and $\chi = \sigma$ or ϵ. By applying the boundary conditions to (5.5), we obtain

$$\left(\begin{bmatrix} K & L_\sigma \\ 0 & M_\sigma \end{bmatrix} + \mathrm{j}\omega \begin{bmatrix} N & L_\epsilon \\ L_\sigma^\top & M_\epsilon \end{bmatrix} \right) \begin{bmatrix} \boldsymbol{a} \\ \boldsymbol{\phi} \end{bmatrix} = \boldsymbol{b}_1 + \mathrm{j}\omega \boldsymbol{b}_2. \tag{5.10}$$

Note that the coefficient matrices are deformed by the operation explained in Section 2.8 to impose the Dirichlet boundary conditions. As a result, $\boldsymbol{b}_1$ and $\boldsymbol{b}_2$ come from the first and second coefficient matrices in (5.10), respectively.

We can see that (5.10) is the asymmetric equation, which can be solved by the iterative methods for the large sparse asymmetric equation such as BiCGstab [70]. Since the author's numerical experiments did not converge, it is suggested that some preprocessing and gauge conditions should be added. Although there are some symmetrization techniques using the gauge conditions, it may deteriorate the convergence of the iterative method [85] because the condition number of the coefficient matrix becomes large. Therefore, we try to apply the CVL method to (5.10) without any gauge conditions.

If we consider the model order reduction of (5.10), we find the following four difficulties in applying the CVL method to (5.10):

1. The right hand side of (5.10) results in two transfer functions due to the frequency dependent term. So, we have to apply the CVL method twice.
2. We cannot take to inverse of the first coefficient matrix of (5.10), which represents the stationary limit. This is because, in the stationary limit, Gauss's law in Ω_e vanishes from the governing equations, and we cannot determine ϕ in Ω_e.
3. We cannot compute $A^\top$ in the CVL algorithm 8 because the inconsistent equations are derived.
4. We have to solve the asymmetric equation in the CVL iteration.

Let us consider the first point. This is caused by the treatment of the Dirichlet boundary conditions. The treatment explained in Section 2.8 is introduced to make the coefficient matrix symmetry. If we allow the asymmetric matrix in the resultant equation, we can

make the right hand side frequency independent. To do so, we do not carry out the second operations in (2.83), (2.84) for the second coefficient matrix (5.5). Then, we can write

$$\left(\begin{bmatrix} K & L_\sigma \\ 0 & M_\sigma \end{bmatrix} + \mathrm{j}\omega \begin{bmatrix} N & L_\epsilon \\ L_\sigma^\top & M_\epsilon \end{bmatrix} \right) \begin{bmatrix} \boldsymbol{a} \\ \boldsymbol{\phi} \end{bmatrix} = \boldsymbol{b}_1. \tag{5.11}$$

Since the diagonal and non-diagonal component of the i-th row of the matrix becomes a constant and zeros, respectively, we confirm that the Dirichlet boundary condition is imposed correctly.

Then, let us consider the second point. If we consider to apply the CVL algorithm to

$$\mathcal{H}(s) = \boldsymbol{b}_1^\top \left(\begin{bmatrix} K & L_\sigma \\ 0 & M_\sigma \end{bmatrix} + \mathrm{j}\omega \begin{bmatrix} N & L_\epsilon \\ L_\sigma^\top & M_\epsilon \end{bmatrix} \right)^{-1} \boldsymbol{b}_1, \tag{5.12}$$

we have to take inverse of

$$\begin{bmatrix} K & L_\sigma \\ 0 & M_\sigma \end{bmatrix} \tag{5.13}$$

However, we cannot take inverse because M_σ^{nn} becomes zero matrix on the vertices in Ω_e. To circumvent this problem, we write the current continuity equation as follows:

$$\nabla \cdot (\sigma(\mathrm{j}\omega \boldsymbol{A} + \nabla\phi) + \mathrm{j}\omega\epsilon\nabla\phi) = 0, \quad \text{in } \overline{\Omega_\mathrm{c}}, \tag{5.14}$$

$$\nabla \cdot \epsilon\nabla\phi = 0, \quad \text{in } \Omega_\mathrm{e} \tag{5.15}$$

which is equivalent to the original current continuity equation (5.2). (5.42) denotes Gauss's law in the external domain of the conductor, and expresses that there is no true charge outside the conductor. Using this expression (5.14) and (5.42), we can solve the equation at the stationary limit $\omega \to 0$ because Gauss's law in Ω_e does not vanish from the governing equations. Then, we introduce the following notations:

$$\phi = \phi_i, \quad \text{in } \overline{\Omega_\mathrm{c}}, \tag{5.16}$$

$$\phi = \phi_e, \quad \text{in } \Omega_\mathrm{e}. \tag{5.17}$$

The FE discretization of (5.1), (5.14), and (5.42) results in

$$\left(\begin{bmatrix} K & L_{\sigma 1} & 0 \\ 0 & M_{\sigma 11} & 0 \\ 0 & M_{\epsilon 21} & M_{\epsilon 22} \end{bmatrix} + \mathrm{j}\omega \begin{bmatrix} N & L_{\epsilon 1} & L_{\epsilon 2} \\ L_{\sigma 1}^\top & M_{\epsilon 11} & M_{\epsilon 12} \\ 0 & 0 & 0 \end{bmatrix} \right) \begin{bmatrix} \boldsymbol{a} \\ \boldsymbol{\phi}_i \\ \boldsymbol{\phi}_e \end{bmatrix} = \boldsymbol{b}_1 \tag{5.18}$$

where

$$\begin{bmatrix} L_{\chi 1} & L_{\chi 2} \end{bmatrix} = L_\chi, \tag{5.19}$$

$$\begin{bmatrix} M_{\chi 11} & M_{\chi 12} \\ M_{\chi 21} & M_{\chi 22} \end{bmatrix} = M_\chi. \tag{5.20}$$

Now we can compute the inverse of

$$\begin{bmatrix} K & L_{\sigma 1} & 0 \\ 0 & M_{\sigma 11} & 0 \\ 0 & M_{\epsilon 21} & M_{\epsilon 22} \end{bmatrix} \tag{5.21}$$

because the matrix encompasses Gauss's law in Ω_{e}.

Let us consider the third point. When we apply the non-Hermitian CVL algorithm 8, we have to compute the transposition $A^{\top}$. In our problem, it corresponds to solve

$$\begin{bmatrix} K & 0 & 0 \\ L_{\sigma 1}^{\top} & M_{\sigma 11} & M_{\epsilon 12} \\ 0 & 0 & M_{\epsilon 22} \end{bmatrix} \boldsymbol{y} = \begin{bmatrix} N & L_{\sigma 1} & 0 \\ L_{\epsilon 1}^{\top} & M_{\epsilon 11} & 0 \\ L_{\epsilon 2}^{\top} & M_{\epsilon 21} & 0 \end{bmatrix} \boldsymbol{v}_i^{\bullet}. \tag{5.22}$$

By multiplying the discrete divergence operator $[G]^{\top}$ by the first line of (5.22), we have

$$0 = \begin{bmatrix} L_{\sigma 1}^{\top} & M_{\sigma 11} & 0 \end{bmatrix} \boldsymbol{v}_i^{\bullet}. \tag{5.23}$$

If we solve (5.22) by the iterative solvers, (5.23) must be consistent with the second and third lines of (5.22). Nevertheless, it seems to be inconsistent. Indeed, from the author's numerical experiments, we cannot solve (5.22) by the iterative solvers. The problem comes from the gauge freedoms of the edge elements $\boldsymbol{w}_i^e$. Although we consider that this problem can be solved by imposing the gauge condition on the curl-curl matrix K, we do not take this approach in this study because the gauge condition would deteriorate the convergence of the iterative solvers [85]. To overcome this difficulty, we avoid the computation of the transposition $A^{\top}$ by using the transposition free version of the CVL algorithm 9. Owing to the algorithm, we can compute κ_n in the reduced order model by computing A twice per iteration. Note that the computation of A is always consistent, and there is no difficulty on the convergence of the iterative method.

Finally, we can apply the CVL algorithm to the Darwin model of Maxwell's equation. However, we have to solve the asymmetric equations in each CVL iteration. In the CVL iteration, we solve

$$\begin{bmatrix} K & L_{\sigma 1} & 0 \\ 0 & M_{\sigma 11} & 0 \\ 0 & M_{\epsilon 21} & M_{\epsilon 22} \end{bmatrix} \boldsymbol{y} = \begin{bmatrix} N & L_{\epsilon 1} & L_{\epsilon 2} \\ L_{\sigma 1}^{\top} & M_{\epsilon 11} & M_{\epsilon 12} \\ 0 & 0 & 0 \end{bmatrix} \boldsymbol{z} \tag{5.24}$$

for $\boldsymbol{y}$. Although the matrix is asymmetric, we find the the equation is decoupled to three equations:

$$M_{\sigma 11}\boldsymbol{y}_i = L_{\sigma 1}^{\top}\boldsymbol{z}_a + M_{\epsilon 11}\boldsymbol{z}_i + M_{\epsilon 12}\boldsymbol{z}_e, \tag{5.25}$$

$$M_{\epsilon 22}\boldsymbol{y}_e = -M_{\epsilon 21}\boldsymbol{y}_i, \tag{5.26}$$

$$K\boldsymbol{y}_a = -L_{\sigma 1}\boldsymbol{y}_i + N\boldsymbol{z}_a + L_{\epsilon 1}\boldsymbol{z}_i + L_{\epsilon 2}\boldsymbol{z}_e \tag{5.27}$$

where $\boldsymbol{y} = [\boldsymbol{y}_a, \boldsymbol{y}_i, \boldsymbol{y}_e]^\top$, and $\boldsymbol{z} = [\boldsymbol{z}_a, \boldsymbol{z}_i, \boldsymbol{z}_e]^\top$. From top to bottom, the equations are the Poisson equation in Ω_c, Poinsson equation in Ω_e, and magnetostatic Maxwell's equations, respectively. Since the coefficient matrices of the three equations are symmetric, we can solve the equations by the iterative solvers for the symmetric equations. In this study, we use the ICCG method to solve the equations. Note that we have to set the different ICCG convergence conditions for each equation.

The above solutions are summarized as follows:

1. Hide the frequency dependent term into the left hand side by changing the operations to impose the Dirichlet boundary conditions.
2. Use Gauss's law in Ω_e by changing the expression of the current continuity law.
3. Use Algorithm 9 to avoid the computation of $A^\top$ in the CVL iteration.
4. Decouple the equations into three symmetric equations.

5.1.1 Reconstruction of the electromagnetic fields

Using Algorithm 9, we obtain

$$(D_n^{-1} - sT_nD_n^{-1})\boldsymbol{z} = \boldsymbol{e}_1 I(s) \tag{5.28}$$

where $D_n = [\kappa_1, \kappa_3, \ldots, \kappa_{2n-1}]$, and

$$T_nD_n^{-1} = \begin{bmatrix} -\kappa_2 & \kappa_2 & & & 0 \\ \kappa_2 & -(\kappa_2+\kappa_4) & \ddots & & \\ & \ddots & \ddots & & \\ & & -(\kappa_{2n-4}+\kappa_{2n-2}) & \kappa_{2n-2} & \\ 0 & & \kappa_{2n-2} & -(\kappa_{2n-2}+\kappa_{2n}) \end{bmatrix}. \tag{5.29}$$

The electromagnetic fields are reconstructed by using the basis vectors as follows:

$$\begin{bmatrix} \boldsymbol{a} \\ \boldsymbol{\phi}_i \\ \boldsymbol{\phi}_e \end{bmatrix} = \sum_{i=1}^{n} \frac{z_i}{\kappa_{2i-1}} \boldsymbol{u}_i. \tag{5.30}$$

5.2 Numerical results

5.2.1 Cylinder model

To validate the proposed method, we consider the cylindrical conductor model shown in Fig. 5.1. The conductivity σ, relative permittivity ϵ_r, and relative permeability μ_r of the conductor domain Ω_c are $1.0 \times 10^6 \mathrm{S/m}, 1.0$, and 1.0, respectively. On the boundaries Γ_0, Γ_1, the electric scalar potential is set to $\phi = 0, 1$. The number of the elements and

nodes in the finite element mesh is 208095 and 41775, respectively. The ICCG convergence criterion is set to $\epsilon_a = 10^{-10}$ for the static Maxwell equations, $\epsilon_c = 10^{-30}$ for the Poisson equation in Ω_c, $\epsilon_e = 10^{-30}$ for the Poisson equation in Ω_e, respectively. The values in the continued fraction obtained from the CVL iteration 9 are summarized in Table. 5.1. We observe that the negative values are obtained and the large scale differences between κ_{2n-1} and κ_{2n}. To evaluate the quality of the reconstructed electromagnetic fields, we compute the residuals of the reconstructed fields by

$$r(\omega) = \frac{|\boldsymbol{b}_1 - (\widetilde{K} + \mathrm{j}\omega\widetilde{N})\boldsymbol{x}_{\mathrm{rec}}|}{|\boldsymbol{b}_1|}, \tag{5.31}$$

$$\widetilde{K} = \begin{bmatrix} K & L_{\sigma 1} & 0 \\ 0 & M_{\sigma 11} & 0 \\ 0 & M_{\epsilon 21} & M_{\epsilon 22} \end{bmatrix}, \tag{5.32}$$

$$\widetilde{N} = \begin{bmatrix} N & L_{\epsilon 1} & L_{\epsilon 2} \\ L_{\sigma 1}^{\top} & M_{\epsilon 11} & M_{\epsilon 12} \\ 0 & 0 & 0 \end{bmatrix} \tag{5.33}$$

where $\boldsymbol{x}_{\mathrm{rec}}$ is the reconstructed solutions.

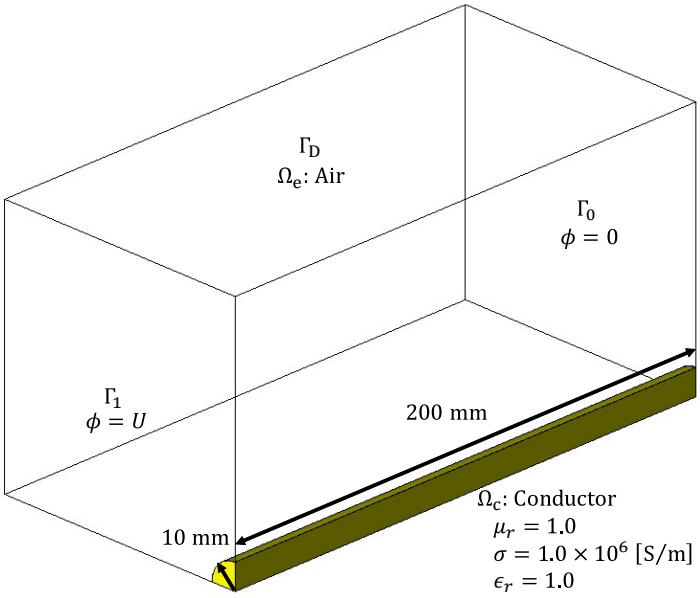

Figure5.1: Cylinder model supplied by U volt source.

The residual of the reconstructed electromagnetic fields at each frequency is shown in Fig. 5.2. We observe that the residual becomes smaller when we increase the number of the stages in the continued fraction. When the stage is 15, the residual becomes minimum around 10kHz. The skin depth is approximately 5mm at 10kHz, which is smaller than the

Table5.1: Values in the continued fraction obtained from the CVL algorithm applied to the cylinder model.

n	κ_{2n-1}	κ_{2n}
1	6.954×10^{4}	-3.082×10^{-12}
2	-5.363×10^{7}	-1.613×10^{-15}
3	-3.999×10^{9}	-2.975×10^{-16}
4	-8.204×10^{9}	-5.098×10^{-17}
5	-2.502×10^{9}	4.869×10^{-13}
6	2.847×10^{9}	-7.090×10^{-17}
7	-8.993×10^{10}	-1.366×10^{-17}
8	8.895×10^{10}	1.265×10^{-16}
9	-3.383×10^{10}	-1.067×10^{-15}
10	-1.220×10^{11}	3.508×10^{-18}
11	1.0371×10^{12}	-3.062×10^{-19}
12	4.064×10^{13}	5.016×10^{-19}
13	1.692×10^{12}	1.355×10^{-16}
14	-4.783×10^{11}	-3.643×10^{-18}
15	-1.426×10^{11}	7.428×10^{-17}

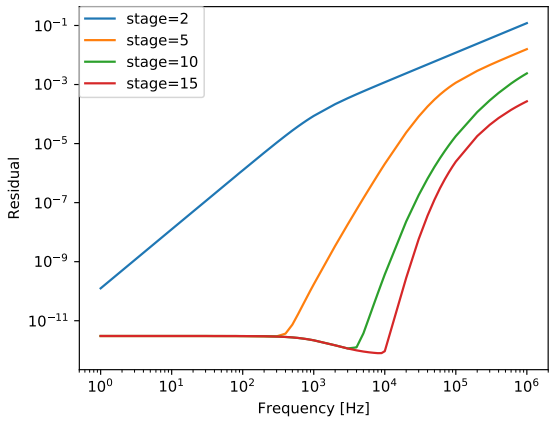

Figure5.2: Residual of the reconstructed electromagnetic fields.

radius of the conductor. In addition, since the element size in the conductor is 1mm, the finite element solutions are reliable up to around 10kHz. ROM obtained by the proposed method reproduces the electromagnetic fields at satisfactory accuracy.

To validate the reconstructed electromagnetic fields, we compare it with the solutions of the full Maxwell equations. We solve

$$\nabla \times \nu \nabla \times \boldsymbol{A} + \mathrm{j}\omega\sigma(\boldsymbol{A} + \nabla\Phi) + (\mathrm{j}\omega)^2\epsilon(\boldsymbol{A} + \nabla\Phi) = 0, \tag{5.34}$$

$$\mathrm{j}\omega\nabla \cdot \sigma(\boldsymbol{A} + \nabla\Phi) + (\mathrm{j}\omega)^2\nabla \cdot \epsilon(\boldsymbol{A} + \nabla\Phi) = 0, \tag{5.35}$$

for the boundary conditions:

$$\boldsymbol{A} \times \boldsymbol{n} = \boldsymbol{0}, \quad \phi = 1, \quad \text{on } \Gamma_l, l = 0, 1, \quad \text{(PEC)} \tag{5.36}$$

$$\boldsymbol{B} \cdot \boldsymbol{n} = 0, \quad \boldsymbol{D} \cdot \boldsymbol{n} = 0, \quad \text{on } \Gamma_{\mathrm{D}}, \quad \text{(Symmetric boundary)}. \tag{5.37}$$

The electromagnetic fields obtained by the proposed method and the full Maxwell equations are given in Figs. 5.3-5.6. The current density and flux density reconstructed from the CVL basis are in good agreement with those obtained by the full Maxwell equations, whereas the real and imaginary parts of the electric field are not correct in Ω_{e}. In the Darwin approximation, we ignore the displacement current $\boldsymbol{D}_{\mathrm{T}}$ due to the vector potential $\boldsymbol{A}$. This means that the displacement current due to the vector potential $\boldsymbol{A}$ does not carry the charge and there is no electric flux density. To restrict the vector potential, we consider Gauss's law in Ω_{e}.

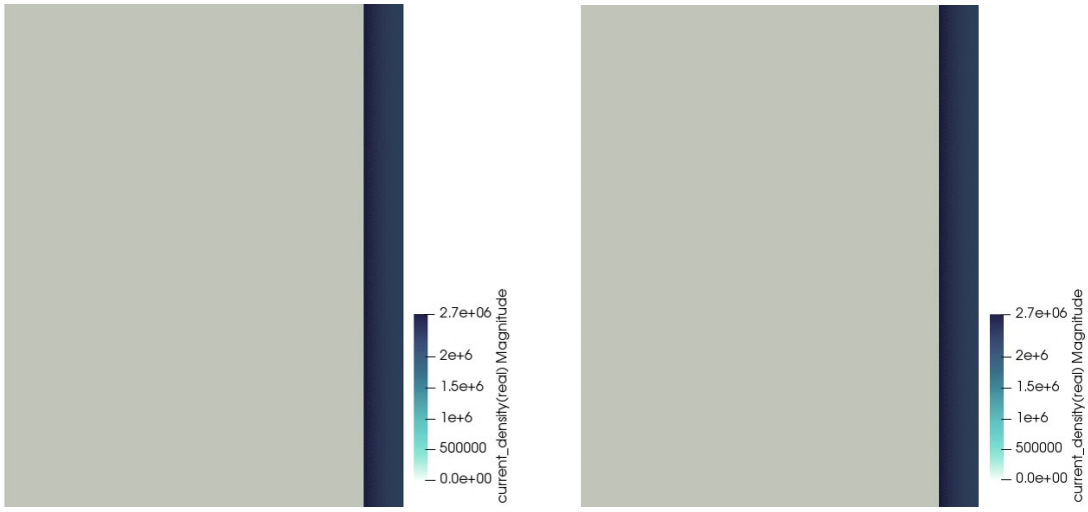

Figure5.3: Comparison of the real part of the current densities obtained by the proposed method (left) and full Maxwell's equations (right) at 1kHz.

$$\nabla \cdot \boldsymbol{D}_{\mathrm{T}} = 0, \quad \text{in } \Omega_{\mathrm{e}}. \tag{5.38}$$

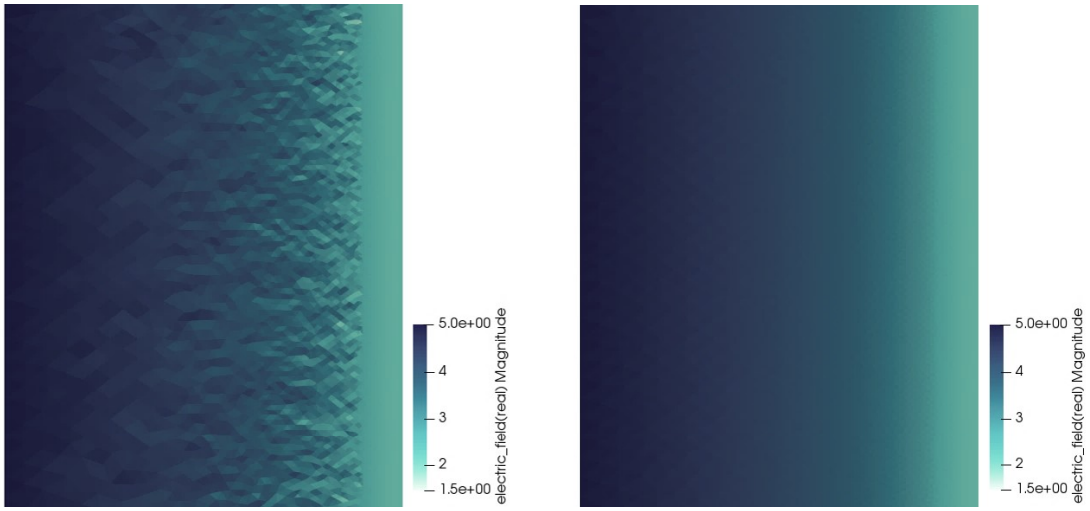

Figure5.4: Comparison of the real part of the electric fields obtained by the proposed method (left) and full Maxwell's equations (right) at 1kHz.

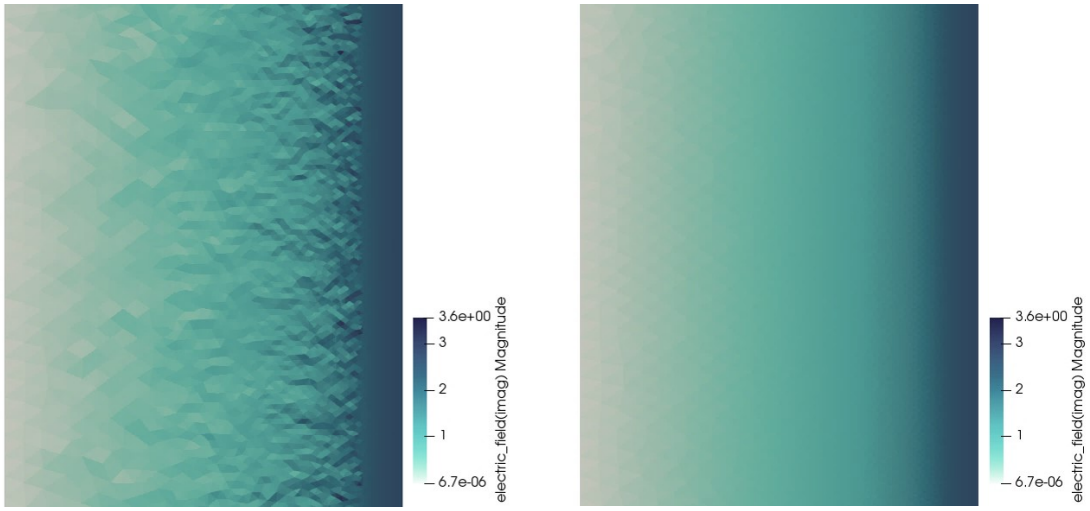

Figure5.5: Comparison of the imaginary part of the electric fields obtained by the proposed method (left) and full Maxwell's equations (right) at 1kHz.

To impose this condition on the vector potential, we modify the vector potential obtained by the proposed method by using the extra scalar potential χ. Since the vector potential has indeterminacy of the gradient component, we can modify it by

$$\nabla \cdot (\epsilon \boldsymbol{A} + \epsilon \nabla \chi) = 0, \quad \text{in } \Omega_{\mathrm{e}}. \tag{5.39}$$

By solving the equation for χ, we obtain the vector potential which satisfies (5.38). In the

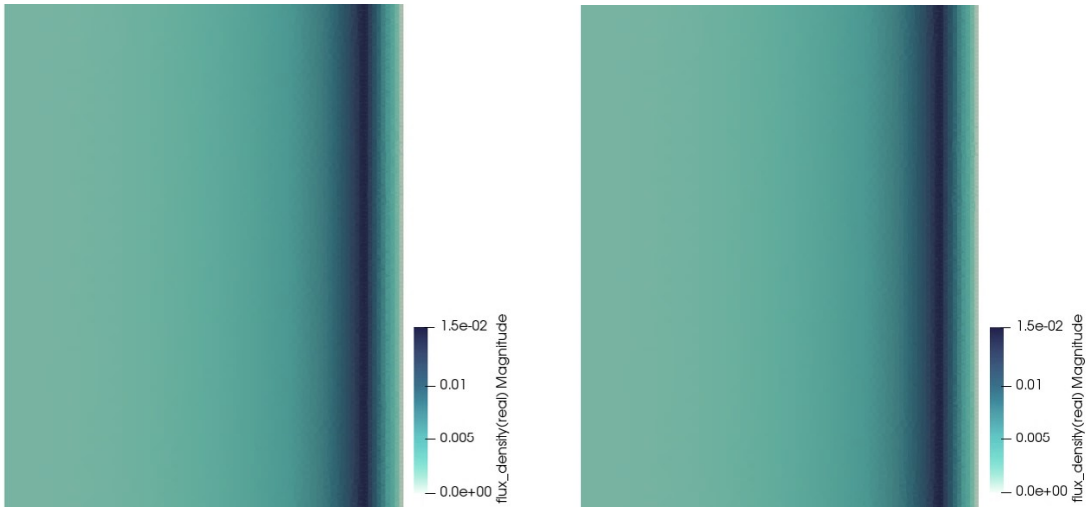

Figure5.6: Comparison of the real part of the flux densities obtained by the proposed method (left) and full Maxwell's equations (right) at 1kHz.

proposed method, we solve

$$\nabla \times \nu \nabla \boldsymbol{A} + \sigma(\mathrm{j}\omega \boldsymbol{A} + \nabla\phi) + \mathrm{j}\omega\epsilon\nabla\phi = 0, \tag{5.40}$$

$$\nabla \cdot (\sigma(\mathrm{j}\omega \boldsymbol{A} + \nabla\phi) + \mathrm{j}\omega\epsilon\nabla\phi) = 0, \quad \text{in } \overline{\Omega_{\mathrm{c}}}, \tag{5.41}$$

$$\nabla \cdot \epsilon\nabla\phi = 0, \quad \text{in } \Omega_{\mathrm{e}}, \tag{5.42}$$

$$\nabla \cdot (\epsilon \boldsymbol{A} + \epsilon\nabla\chi) = 0, \quad \text{in } \Omega_{\mathrm{e}}, \tag{5.43}$$

simultaneously. The FE discretization results in

$$\left(\begin{bmatrix} K & L_{\sigma 1} & 0 & 0 \\ 0 & M_{\sigma 11} & 0 & 0 \\ 0 & M_{\epsilon 21} & M_{\epsilon 22} & 0 \\ L_{\epsilon 2}^{\top} & 0 & 0 & M_{\epsilon 22} \end{bmatrix} + \mathrm{j}\omega \begin{bmatrix} N & L_{\epsilon 1} & L_{\epsilon 2} & 0 \\ L_{\sigma 1}^{\top} & M_{\epsilon 11} & M_{\epsilon 12} & 0 \\ 0 & 0 & 0 & 0 \\ 0 & 0 & 0 & 0 \end{bmatrix} \right) \begin{bmatrix} \boldsymbol{a} \\ \boldsymbol{\phi}_i \\ \boldsymbol{\phi}_e \\ \boldsymbol{\chi} \end{bmatrix} = \boldsymbol{b}_1. \tag{5.44}$$

In the CVL algorithm, we solve the decoupled four equations:

$$M_{\sigma 11}\boldsymbol{y}_i = L_{\sigma 1}^{\top}\boldsymbol{z}_a + M_{\epsilon 11}\boldsymbol{z}_i + M_{\epsilon 12}\boldsymbol{z}_e, \tag{5.45}$$

$$M_{\epsilon 22}\boldsymbol{y}_e = -M_{\epsilon 21}\boldsymbol{y}_i, \tag{5.46}$$

$$K\boldsymbol{y}_a = -L_{\sigma 1}\boldsymbol{y}_i + N\boldsymbol{z}_a + L_{\epsilon 1}\boldsymbol{z}_i + L_{\epsilon 2}\boldsymbol{z}_e, \tag{5.47}$$

$$M_{\epsilon 22}\boldsymbol{y}_\chi = -L_{\epsilon 2}^{\top}\boldsymbol{y}_a \tag{5.48}$$

where $\boldsymbol{y} = [\boldsymbol{y}_a, \boldsymbol{y}_i, \boldsymbol{y}_e, \boldsymbol{y}_\chi]^{\top}$, and $\boldsymbol{z} = [\boldsymbol{z}_a, \boldsymbol{z}_i, \boldsymbol{z}_e, \boldsymbol{z}_\chi]^{\top}$. Using this expression, we can modify the electric field in Ω_{e} by

$$\boldsymbol{E} = -\mathrm{j}\omega(\boldsymbol{A} + \nabla\chi) + \nabla\phi_e, \quad \text{in } \Omega_{\mathrm{e}}. \tag{5.49}$$

We can regularize the electric field by using the extra scalar potential χ.

In Figs. 5.7, 5.8, the electric field obtained by the above regularization is in good agreement with that obtained by the full Maxwell equations.

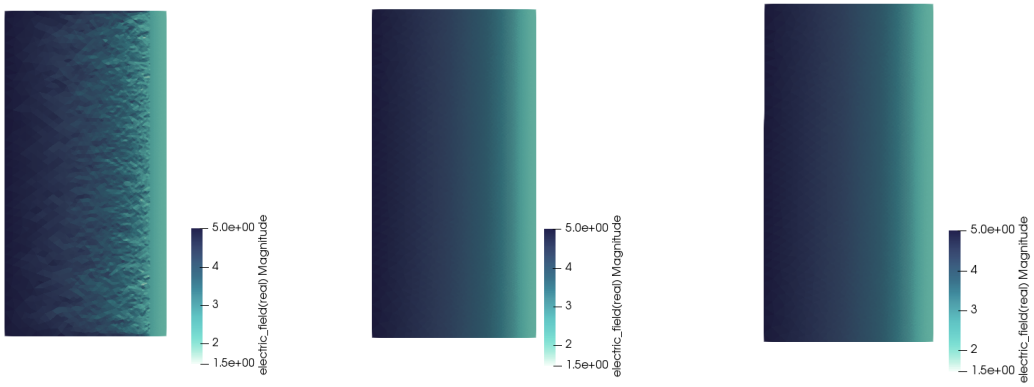

Figure5.7: Improvement the real part of the electric field reconstruction by the regularization. The electric fields obtained by the proposed method (left), regularization method (middle), and full Maxwell's equations (right) are shown.

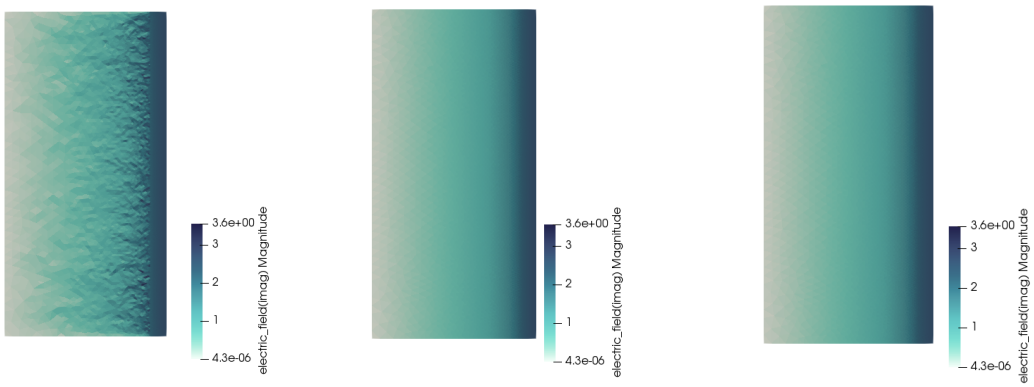

Figure5.8: Improvement the imaginary part of the electric field reconstruction by the regularization. The electric fields obtained by the proposed method (left), regularization method (middle), and full Maxwell's equations (right) are shown.

5.2.2 Massive conductor model

Next, we consider the massive conductor model shown in Fig. 5.9. The conductivity σ, relative permittivity ϵ_r, and relative permeability μ_r of the conductor domain Ω_c are $1.0 \times 10^4 \mathrm{S/m}, 1.0$, and 1.0, respectively. The conductor is embedded in the material whose relative permittivity is 10.0. On the boundaries Γ_0, Γ_1, the electric scalar potential is set to $\phi = 0, 1$. The number of the elements and nodes in the finite element mesh is 1305464 and 238536, respectively. The ICCG convergence criterion is set to $\epsilon_a = 10^{-7}$ for the static Maxwell equations, $\epsilon_c = 10^{-20}$ for the Poisson equation in Ω_c, $\epsilon_e = 10^{-20}$ for the

Poisson equation in Ω_e, respectively. The values in the continued fraction obtained from the CVL iteration 9 are summarized in Table. 5.2.

The residual of the reconstructed electromagnetic fields at each frequency is shown in Fig. 5.10. We observe that the residual becomes smaller when we increase the number of the stages in the continued fraction. In this case, we observe that the obtained ROM is accurate up to the frequency where the skin depth is larger than the finite elements in the conductive domain.

The electromagnetic fields obtained by the proposed method and the full Maxwell equations are given in Figs. 5.11-5.14. Each quantity obtained by the proposed method is in good agreement that obtained by the full Maxwell equations.

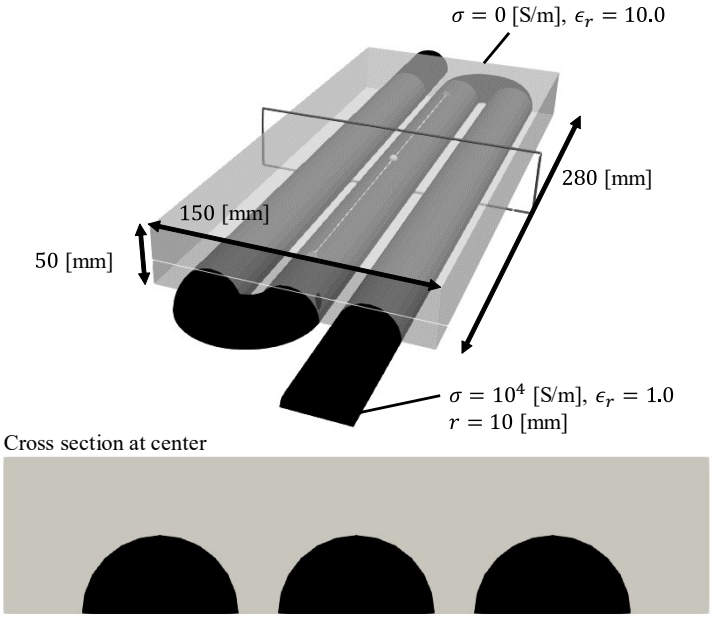

Figure5.9: massive conductor supplied by U volt source.

5.3 Concluding Remarks

We proposed a new method to generate ROM from the Darwin model of Maxwell's equations. Although the asymmetric equations arise from the FE discretization of the Darwin model, we can obtain ROM only by solving the symmetric equations such as Poisson equations and static Maxwell equations. Since the size of the obtained ROM is relatively small, we believe that the proposed method is effective when we consider the time-domain analysis.

Table5.2: Values in the continued fraction obtained from the CVL algorithm applied to the massive conductor model.

n	κ_{2n}	κ_{2n+1}
0	6.866×10^{3}	2.717×10^{-13}
1	1.207×10^{7}	1.681×10^{-14}
2	3.718×10^{7}	6.991×10^{-15}
3	7.020×10^{7}	1.265×10^{-15}
4	1.248×10^{8}	1.952×10^{-15}
5	3.144×10^{8}	4.231×10^{-16}
6	6.433×10^{8}	1.833×10^{-15}
7	7.847×10^{8}	1.331×10^{-15}
8	4.580×10^{8}	3.182×10^{-16}
9	7.908×10^{8}	3.985×10^{-16}
10	4.954×10^{8}	1.699×10^{-16}
11	-7.272×10^{8}	-5.424×10^{-15}
12	3.199×10^{8}	6.489×10^{-16}
13	-1.796×10^{9}	-2.614×10^{-15}
14	8.994×10^{6}	-2.641×10^{-13}

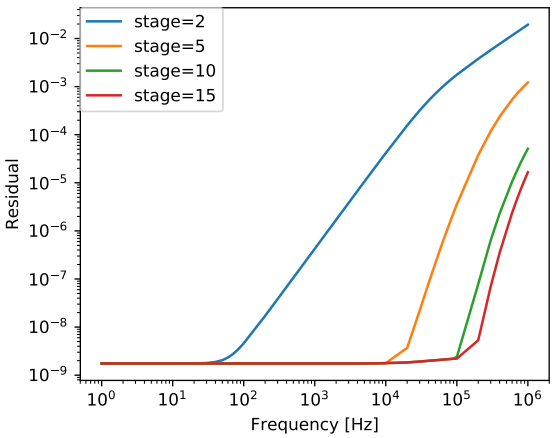

Figure5.10: Residual of the reconstructed electromagnetic fields of the massive conductor.

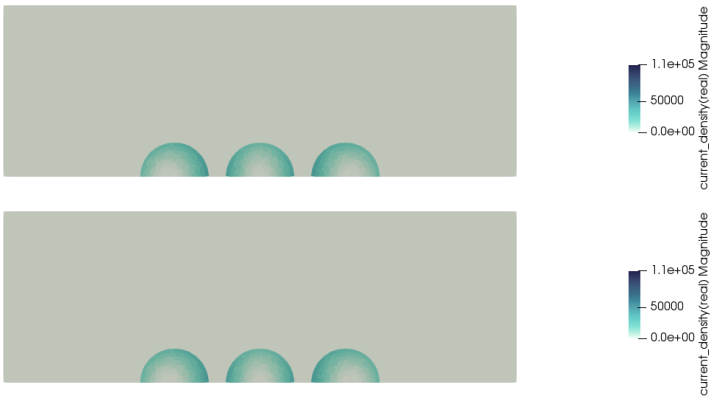

Figure5.11: Comparison of the real part of the current densities obtained by the proposed method (upper) and full Maxwell's equations (lower) at 100kHz.

Figure5.12: Comparison of the real part of the electric fields obtained by the proposed method (upper) and full Maxwell's equations (lower) at 100kHz.

Figure5.13: Comparison of the imaginary part of the electric fields obtained by the proposed method (upper) and full Maxwell's equations (lower) at 100kHz.

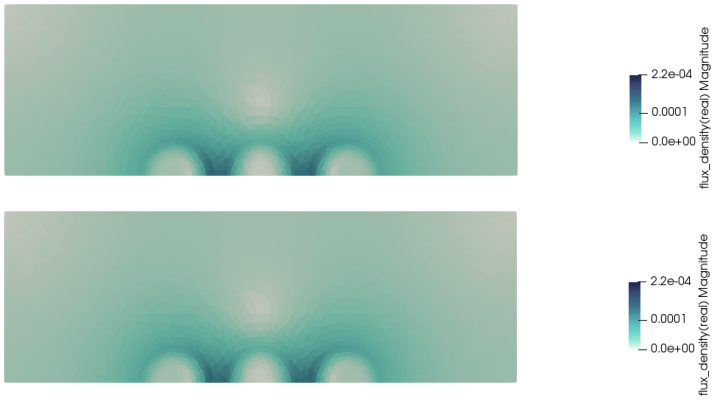

Figure5.14: Comparison of the real part of the flux densities obtained by the proposed method (upper) and full Maxwell's equations (lower) at 100kHz.

Chapter 6.

Conclusion and future work

In this thesis, we developed the MOR techniques based on the Krylov subspace methods. Moreover, we have applied the method to the homogenization and Darwin model of Maxwell's equations. We summarize the results of this thesis.

For the Krylov subspace methods based MOR, we developed the CVL algorithms that compute the continued fraction approximation of the transfer function $\mathcal{H}(s)$. We derived CVL from PVL, which computes the Padé approximation via the Lanczos algorithm, by changing the normalization condition. We also developed different algorithms for the computation of CVL. We applied the CVL algorithms to the FE equations of the electromagnetic apparatuses and obtained the Cauer circuit as a reduced-order model. We confirmed that we could perform the time-domain analysis faster than FEM.

For the homogenization method, we applied the CVL algorithm to the homogenization method. So far, we had to solve the equations at each frequency to determine the complex permeability of the arbitrary shaped-conductor for the wide frequency range. Using the proposed method, we can obtain it by solving the equations for few times. By using the obtained complex permeability, we can reduce the number of unknowns and the computational costs because the microstructure of the materials are replaced by homogeneous materials. We also proposed a method to perform the time-domain analysis of the homogenization of Maxwell's equations by utilizing the Cauer circuit representation of the complex permeability. To reduce the computational cost of the homogenization farther, we proposed a method to derive the equivalent circuit from the homogenization of Maxwell's equations. Owing to the method, we can reduce the computational cost because the size of the equivalent circuit is much smaller than the homogenization of Maxwell's equations. Utilizing the physical meaning of the equivalent circuit, we can introduce the nonlinearity due to the core saturation into the obtained equivalent circuit. We applied the complex permeability to Dowell's equations and showed that the proposed method can effectively.

For the Darwin model of Maxwell's equations, we applied the CVL algorithm to the equations and obtained ROM which is accurate in the wide frequency range. Although

the FE discretization of the Darwin model of Maxwell's equations results in the asymmetric equations, we can obtain ROM only by solving the Poisson equations and static Maxwell's equations, which are symmetric equations.

It has been difficult to evaluate the eddy current losses considering the external control systems due to the computational cost of the FE equations. Using the CVL algorithm, we can obtain the Cauer circuit, which is accurate in the wide frequency range, whose size is much smaller than the FE equations. Moreover, we can introduce the nonlinearity due to the magnetic core saturation in the Cauer circuit. The obtained Cauer circuit can be used in the usual circuit simulators such as the SPICE simulator and can be solved with the external control systems at high speed. Therefore, we consider the proposed algorithms can fill the gap between the FEM and circuit simulation. We consider that the methods can be useful for the optimization of electromagnetic systems.

There are several open problems that we suggest for future works. We describe a list of them below.

1. When we consider the symmetric transfer function such as the symmetric positive-definite matrices and the same input-output vectors, we can obtain the passive ROM because we can show that the circuit parameters are always positive. However, if the conditions are not satisfied, we cannot preserve the passivity of the original system on ROM. This property has been widely known, and there are lots of studies and methods on these topics. We consider the passivity is important especially for the time-domain analysis of the Darwin model of Maxwell's equations. Therefore, we have to check the stability of the obtained ROMs.
2. We have introduced nonlinearity due to the magnetic saturation into the Cauer circuit. Although this method seems to effective, we consider that we have to validate the effectiveness and accuracy of the nonlinear Cauer circuit quantitatively because the introduction of the nonlinearity is followed by the physical intuition.
3. The time-domain analysis of the Darwin model is also important. Since the FE discretization of the Darwin model results in large ill-conditioned asymmetric equations, it is difficult to solve it repeatedly. In contrast, the reduced-order model obtained by the proposed method results in small symmetric equations, which can readily be solved by the direct method. Therefore, we can expect that we can perform the time-domain analysis much faster than the FE equations. However, we have not yet validated the time-domain analysis of ROM of the Darwin model. Since the circuit parameters are negative, there is a concern about the instability in the time-domain analysis. This problem relates to the first point. We consider further study has to be done.

Acknowledgements

I sincerely thank my supervisor, Professor Hajime Igarashi, for giving me the opportunity to study as a Ph. D student in Hokkaido University. The study cannot be accomplished without enormous continuous support and insightful comments.

I would like to thank Professor Yuh Yamashita, Professor Hiroyuki Kita, and Associate Professor So Noguchi for being on my committee.

Special thanks go to past and present members of Applied Electromagnetic Laboratory for my pleasant days in the laboratory. I am also grateful to Dr. Shogo Fujita, Mr. Teki Imai, Mrs. Hisayo Saito for their great support and advices for the study, computer environment and procedures. And I would like to express my gratitude to all the staff and students whom I have met during my doctoral life at Hokkaido University.

I would like to thank the members of L2EP for their warm hospitality during my visit to France. I would also like to take this opportunity to thank Professor Stéphane Clénet, Professor Johan Gyselinck, and Professor Ruth V. Sabariego for the enthusiastic discussion on the model order reduction and homogenization method.

Finally, I would like to extend my indebtedness to my family for their understanding and support during the course of my study.

References

[1] A. De Almeida, J. Fong, C. Brunner, R. Werle, and M. Van Werkhoven, "New technology trends and policy needs in energy efficient motor systems - a major opportunity for energy and carbon savings," *Renewable and Sustainable Energy Reviews*, vol. 115, p. 109384, 2019. [Online]. Available: http://www.sciencedirect.com/science/article/pii/S1364032119305921

[2] P. P. Silvester and R. L. Ferrari, *Finite elements for electrical engineers*. Cambridge university press, 1996.

[3] X. Nan and C. R. Sullivan, "Simplified high-accuracy calculation of eddy-current loss in round-wire windings," in *2004 IEEE 35th Annual Power Electronics Specialists Conference (IEEE Cat. No. 04CH37551)*, vol. 2. IEEE, 2004, pp. 873–879.

[4] R. Wojda and M. Kazimierczuk, "Winding resistance of litz-wire and multi-strand inductors," *IET Power Electronics*, vol. 5, no. 2, pp. 257–268, 2012.

[5] C. Vollaire and L. Nicolas, "Preconditioning techniques for the conjugate gradient solver on a parallel distributed memory computer," *IEEE transactions on magnetics*, vol. 34, no. 5, pp. 3347–3350, 1998.

[6] T. Iwashita and M. Shimasaki, "Parallel processing of 3-d eddy current analysis with moving conductor using parallelized iccg solver with renumbering process," *IEEE transactions on magnetics*, vol. 36, no. 4, pp. 1504–1509, 2000.

[7] R. Hiptmair, "Multigrid method for h (div) in three dimensions," *Electron. Trans. Numer. Anal*, vol. 6, no. 1, pp. 133–152, 1997.

[8] D. N. Arnold, R. S. Falk, and R. Winther, "Multigrid in h (div) and h (curl)," *Numerische Mathematik*, vol. 85, no. 2, pp. 197–217, 2000.

[9] K. Fujiwara, T. Nakata, N. Okamoto, and K. Muramatsu, "Method for determining relaxation factor for modified newton-raphson method," *IEEE transactions on magnetics*, vol. 29, no. 2, pp. 1962–1965, 1993.

[10] K. Fujiwara, T. Nakata, and H. Fusayasu, "Acceleration of convergence characteristic of the iccg method," *IEEE transactions on magnetics*, vol. 29, no. 2, pp. 1958–1961, 1993.

[11] Y. Sato and H. Igarashi, "Generation of equivalent circuit from finite-element model using model order reduction," *IEEE transactions on magnetics*, vol. 52, no. 3, pp.

1–4, 2015.

[12] A. Pierquin, T. Henneron, S. Clenet, and S. Brisset, "Model-order reduction of magnetoquasi-static problems based on pod and arnoldi-based krylov methods," *IEEE Transactions on Magnetics*, vol. 51, no. 3, pp. 1–4, 2015.

[13] M. R. Hasan, R. V. Sabariego, C. Geuzaine, and Y. Paquay, "Proper orthogonal decomposition versus krylov subspace methods in reduced-order energy-converter models," in *2016 IEEE International Energy Conference (ENERGYCON)*. IEEE, 2016, pp. 1–6.

[14] T. Henneron and S. Clenet, "Model order reduction of non-linear magnetostatic problems based on pod and dei methods," *IEEE Transactions on Magnetics*, vol. 50, no. 2, pp. 33–36, 2014.

[15] Y. Sato, M. Clemens, and H. Igarashi, "Adaptive subdomain model order reduction with discrete empirical interpolation method for nonlinear magneto-quasi-static problems," *IEEE transactions on magnetics*, vol. 52, no. 3, pp. 1–4, 2015.

[16] L. Montier, A. Pierquin, T. Henneron, and S. Clénet, "Structure preserving model reduction of low-frequency electromagnetic problem based on pod and deim," *IEEE Transactions on Magnetics*, vol. 53, no. 6, pp. 1–4, 2017.

[17] Y. Kiarashinejad, S. Abdollahramezani, and A. Adibi, "Deep learning approach based on dimensionality reduction for designing electromagnetic nanostructures," *npj Computational Materials*, vol. 6, no. 1, pp. 1–12, 2020.

[18] P. Benner, S. Gugercin, and K. Willcox, "A survey of projection-based model reduction methods for parametric dynamical systems," *SIAM review*, vol. 57, no. 4, pp. 483–531, 2015.

[19] Y. Zhu and A. C. Cangellaris, "A new finite element model for reduced order electromagnetic modeling," *IEEE microwave and wireless components letters*, vol. 11, no. 5, pp. 211–213, 2001.

[20] H. Wu and A. C. Cangellaris, "Model-order reduction of finite-element approximations of passive electromagnetic devices including lumped electrical-circuit models," *IEEE transactions on microwave theory and techniques*, vol. 52, no. 9, pp. 2305–2313, 2004.

[21] Y. Sato, T. Shimotani, and H. Igarashi, "Synthesis of cauer-equivalent circuit based on model order reduction considering nonlinear magnetic property," *IEEE Transactions on Magnetics*, vol. 53, no. 6, pp. 1–4, 2017.

[22] L. T. Pillage and R. A. Rohrer, "Asymptotic waveform evaluation for timing analysis," *IEEE Transactions on Computer-Aided Design of Integrated Circuits and Systems*, vol. 9, no. 4, pp. 352–366, 1990.

[23] A. Bultheel and M. Van Barel, "Padé techniques for model reduction in linear system

theory: a survey," *Journal of Computational and Applied Mathematics*, vol. 14, no. 3, pp. 401–438, 1986.

[24] K. Gallivan, E. Grimme, and P. Van Dooren, "Asymptotic waveform evaluation via a lanczos method," *Applied Mathematics Letters*, vol. 7, no. 5, pp. 75–80, 1994.

[25] P. Feldmann and R. W. Freund, "Efficient linear circuit analysis by padé approximation via the lanczos process," *IEEE Transactions on Computer-Aided Design of Integrated Circuits and Systems*, vol. 14, no. 5, pp. 639–649, 1995.

[26] ——, "Reduced-order modeling of large linear subcircuits via a block lanczos algorithm," in *Proceedings of the 32nd annual ACM/IEEE Design Automation Conference*, 1995, pp. 474–479.

[27] R. W. Freund and P. Feldmann, "Reduced-order modeling of large passive linear circuits by means of the sypvl algorithm," in *Proceedings of International Conference on Computer Aided Design*. IEEE, 1996, pp. 280–287.

[28] L. M. Silveira, M. Kamon, I. Elfadel, and J. White, "A coordinate-transformed arnoldi algorithm for generating guaranteed stable reduced-order models of rlc circuits," *Computer Methods in Applied Mechanics and Engineering*, vol. 169, no. 3-4, pp. 377–389, 1999.

[29] A. Odabasioglu, M. Celik, and L. T. Pileggi, "Prima: Passive reduced-order interconnect macromodeling algorithm," in *The Best of ICCAD*. Springer, 2003, pp. 433–450.

[30] R. W. Freund, "Model reduction methods based on krylov subspaces," *Acta Numerica*, vol. 12, pp. 267–319, 2003.

[31] Z. Bai, "Krylov subspace techniques for reduced-order modeling of large-scale dynamical systems," *Applied numerical mathematics*, vol. 43, no. 1-2, pp. 9–44, 2002.

[32] E. Grimme, "Krylov projection methods for model reduction," Ph.D. dissertation, 1997.

[33] A. Kameari, H. Ebrahimi, K. Sugahara, Y. Shindo, and T. Matsuo, "Cauer ladder network representation of eddy-current fields for model order reduction using finite-element method," *IEEE Transactions on Magnetics*, vol. 54, no. 3, pp. 1–4, 2017.

[34] Y. Shindo, T. Miyazaki, and T. Matsuo, "Cauer circuit representation of the homogenized eddy-current field based on the legendre expansion for a magnetic sheet," *IEEE Transactions on Magnetics*, vol. 52, no. 3, pp. 1–4, 2015.

[35] T. Miyazaki, T. Mifune, T. Matsuo, Y. Shindo, Y. Takahashi, and K. Fujiwara, "Equivalent circuit modeling of dynamic hysteretic property of silicon steel under pulse width modulation excitation," *Journal of Applied Physics*, vol. 117, no. 17, p. 17D110, 2015.

[36] K. Sugahara, A. Kameari, H. Ebrahimi, Y. Shindo, and T. Matsuo, "Finite-element

analysis of unbounded eddy-current problems using cauer ladder network method," *IEEE Transactions on Magnetics*, vol. 54, no. 3, pp. 1–4, 2017.

[37] K. Kuriyama, A. Kameari, H. Ebrahimi, T. Fujiwara, K. Sugahara, Y. Shindo, and T. Matsuo, "Cauer ladder network with multiple expansion points for efficient model order reduction of eddy-current field," *IEEE Transactions on Magnetics*, vol. 55, no. 6, pp. 1–4, 2019.

[38] H. Eskandari and T. Matsuo, "Cauer ladder network representation of a nonlinear eddy-current field using a first-order approximation," *IEEE Transactions on Magnetics*, vol. 56, no. 2, pp. 1–4, 2020.

[39] T. Matsuo, T. Fujiwara, K. Kuriyama, K. Sugahara, A. Kameari, T. Tokumasu, and Y. Shindo, "Multi-port model order reduction using a matrix cauer ladder network," *IEEE Transactions on Magnetics*, vol. 56, no. 2, pp. 1–5, 2020.

[40] Y. Shindo, R. Yamamoto, K. Sugahara, T. Matsuo, and A. Kameari, "Equivalent circuit in cauer form for eddy current field including a translational mover," *IEEE Transactions on Magnetics*, 2020.

[41] T. Matsuo, A. Kameari, K. Sugahara, and Y. Shindo, "Matrix formulation of the cauer ladder network method for efficient eddy-current analysis," *IEEE Transactions on Magnetics*, vol. 54, no. 11, pp. 1–5, 2018.

[42] P. H. Mellor, R. Wrobel, and N. McNeill, "Investigation of proximity losses in a high speed brushless permanent magnet motor," in *Conference Record of the 2006 IEEE Industry Applications Conference Forty-First IAS Annual Meeting*, vol. 3. IEEE, 2006, pp. 1514–1518.

[43] M. Popescu and D. G. Dorrell, "Proximity losses in the windings of high speed brushless permanent magnet ac motors with single tooth windings and parallel paths," *IEEE Transactions on Magnetics*, vol. 49, no. 7, pp. 3913–3916, 2013.

[44] R. Wrobel, A. Mlot, and P. H. Mellor, "Contribution of end-winding proximity losses to temperature variation in electromagnetic devices," *IEEE Transactions on Industrial Electronics*, vol. 59, no. 2, pp. 848–857, 2011.

[45] J. Acero, P. J. Hernandez, J. M. Burdio, R. Alonso, and L. Barragdan, "Simple resistance calculation in litz-wire planar windings for induction cooking appliances," *IEEE Transactions on magnetics*, vol. 41, no. 4, pp. 1280–1288, 2005.

[46] Z. Yang, W. Liu, and E. Basham, "Inductor modeling in wireless links for implantable electronics," *IEEE Transactions on Magnetics*, vol. 43, no. 10, pp. 3851–3860, 2007.

[47] P. Dowell, "Effects of eddy currents in transformer windings," in *Proceedings of the Institution of Electrical Engineers*, vol. 113, no. 8. IET, 1966, pp. 1387–1394.

[48] E. Bennett and S. C. Larson, "Effective resistance to alternating currents of multi-

layer windings," *Electrical Engineering*, vol. 59, no. 12, pp. 1010–1016, 1940.

[49] M. Perry, "Multiple layer series connected winding design for minimum losses," *IEEE Transactions on Power Apparatus and Systems*, no. 1, pp. 116–123, 1979.

[50] J. A. Ferreira, "Improved analytical modeling of conductive losses in magnetic components," *IEEE transactions on Power Electronics*, vol. 9, no. 1, pp. 127–131, 1994.

[51] J. Ferreira, "Analytical computation of ac resistance of round and rectangular litz wire windings," in *IEE Proceedings B (Electric Power Applications)*, vol. 139, no. 1. IET, 1992, pp. 21–25.

[52] X. Nan and C. R. Sullivan, "An improved calculation of proximity-effect loss in high-frequency windings of round conductors," in *IEEE 34th Annual Conference on Power Electronics Specialist, 2003. PESC'03.*, vol. 2. IEEE, 2003, pp. 853–860.

[53] H. Igarashi, "Semi-analytical approach for finite-element analysis of multi-turn coil considering skin and proximity effects," *IEEE Transactions on Magnetics*, vol. 53, no. 1, pp. 1–7, 2016.

[54] O. Franz, "Magnetostatik der massekerne," *Archiv für Elektrotechnik*, vol. 25, pp. 436–447, 1931.

[55] M. El Feddi, Z. Ren, A. Razek, and A. Bossavit, "Homogenization technique for maxwell equations in periodic structures," *IEEE Transactions on magnetics*, vol. 33, no. 2, pp. 1382–1385, 1997.

[56] A. D. Podoltsev, I. N. Kucheryavaya, and B. B. Lebedev, "Analysis of effective resistance and eddy-current losses in multiturn winding of high-frequency magnetic components," *IEEE Transactions on Magnetics*, vol. 39, no. 1, pp. 539–548, 2003.

[57] J. Gyselinck and P. Dular, "Frequency-domain homogenization of bundles of wires in 2-d magnetodynamic fe calculations," *IEEE transactions on magnetics*, vol. 41, no. 5, pp. 1416–1419, 2005.

[58] J. Gyselinck, R. Sabariego, and P. Dular, "Time-domain homogenization of windings in 2-d finite element models," *IEEE transactions on magnetics*, vol. 43, no. 4, pp. 1297–1300, 2007.

[59] R. V. Sabariego, P. Dular, and J. Gyselinck, "Time-domain homogenization of windings in 3-d finite element models," *IEEE transactions on magnetics*, vol. 44, no. 6, pp. 1302–1305, 2008.

[60] Y. Sato and H. Igarashi, "Time-domain analysis of soft magnetic composite using equivalent circuit obtained via homogenization," *IEEE Transactions on Magnetics*, vol. 53, no. 6, pp. 1–4, 2017.

[61] R. V. Sabariego and J. Gyselinck, "Eddy-current-effect homogenization of windings in harmonic-balance finite-element models," *IEEE transactions on magnetics*, vol. 53, no. 6, pp. 1–4, 2017.

[62] K. Niyomsatian, J. Gyselinck, and R. V. Sabariego, "Time-domain homogenization of multiturn windings based on rl cauer ladder networks," *International Journal of Numerical Modelling: Electronic Networks, Devices and Fields*, vol. 33, no. 5, p. e2649, 2020.

[63] Y. Sato and H. Igarashi, "Homogenization method based on model order reduction for fe analysis of multi-turn coils," *IEEE Transactions on Magnetics*, vol. 53, no. 6, pp. 1–4, 2017.

[64] J. Larsson, "Electromagnetics from a quasistatic perspective," *American Journal of Physics*, vol. 75, no. 3, pp. 230–239, 2007.

[65] C. Liao and L.-A. Ying, "An analysis of the darwin model of approximation to maxwell's equations in 3-d unbounded domains," *Communications in Mathematical Sciences*, vol. 6, no. 3, pp. 695–710, 2008.

[66] S. E. Kruger, "The three quasistatic limits of the maxwell equations," *arXiv preprint arXiv:1909.11264*, 2019.

[67] S. Koch, H. Schneider, and T. Weiland, "A low-frequency approximation to the maxwell equations simultaneously considering inductive and capacitive phenomena," *IEEE transactions on magnetics*, vol. 48, no. 2, pp. 511–514, 2012.

[68] Z. Badics, J. Pávó, S. Bilicz, and S. Gyimóthy, "Subdomain perturbation finite-element method for quasi-static darwin approximation," *IEEE Transactions on Magnetics*, vol. 56, no. 1, pp. 1–4, 2019.

[69] Y. Saad and M. H. Schultz, "Gmres: A generalized minimal residual algorithm for solving nonsymmetric linear systems," *SIAM Journal on scientific and statistical computing*, vol. 7, no. 3, pp. 856–869, 1986.

[70] M. H. Gutknecht, "Variants of bicgstab for matrices with complex spectrum," *SIAM journal on scientific computing*, vol. 14, no. 5, pp. 1020–1033, 1993.

[71] S. Ho, Y. Zhao, W. Fu, and P. Zhou, "Application of edge elements to 3-d electromagnetic field analysis accounting for both inductive and capacitive effects," *IEEE Transactions on Magnetics*, vol. 52, no. 3, pp. 1–4, 2015.

[72] Y. Zhao and W. Fu, "A new stable full-wave maxwell solver for all frequencies," *IEEE Transactions on Magnetics*, vol. 53, no. 6, pp. 1–4, 2016.

[73] Y. Zhao and Z. Tang, "A novel gauged potential formulation for 3-d electromagnetic field analysis including both inductive and capacitive effects," *IEEE Transactions on Magnetics*, vol. 55, no. 6, pp. 1–5, 2019.

[74] H. Igarashi and T. Honma, "On convergence of iccg applied to finite-element equation for quasi-static fields," *IEEE transactions on magnetics*, vol. 38, no. 2, pp. 565–568, 2002.

[75] P. Sonneveld, "Cgs, a fast lanczos-type solver for nonsymmetric linear systems,"

SIAM journal on scientific and statistical computing, vol. 10, no. 1, pp. 36–52, 1989.

[76] H. K. Dirks, "Quasi-stationary fields for microelectronic applications," *Electrical Engineering*, vol. 79, no. 2, pp. 145–155, 1996.

[77] L. Klinkenbusch, W. Mathis, T. Steinmetz, S. Kurz, and M. Clemens, "Domains of validity of quasistatic and quasistationary field approximations," *COMPEL-The international journal for computation and mathematics in electrical and electronic engineering*, 2011.

[78] P. Degond and P.-A. Raviart, "An analysis of the darwin model of approximation to maxwell' s equations," in *Forum Math*, vol. 4, no. 4, 1992, pp. 13–44.

[79] H. Weitzner and W. Lawson, "Boundary conditions for the darwin model," *Physics of Fluids B: Plasma Physics*, vol. 1, no. 10, pp. 1953–1957, 1989.

[80] R. Hiptmair, F. Kramer, and J. Ostrowski, "A robust maxwell formulation for all frequencies," *IEEE transactions on magnetics*, vol. 44, no. 6, pp. 682–685, 2008.

[81] R. Hiptmair, "Finite elements in computational," *Acta Numerica 2002: Volume 11*, no. 11, p. 237, 2002.

[82] J.-C. Nédélec, "Mixed finite elements in r3," *Numerische Mathematik*, vol. 35, no. 3, pp. 315–341, 1980.

[83] A. Bossavit, "Whitney forms: A class of finite elements for three-dimensional computations in electromagnetism," *IEE Proceedings A (Physical Science, Measurement and Instrumentation, Management and Education, Reviews)*, vol. 135, no. 8, pp. 493–500, 1988.

[84] J. B. Manges and Z. J. Cendes, "A generalized tree-cotree gauge for magnetic field computation," *IEEE Transactions on Magnetics*, vol. 31, no. 3, pp. 1342–1347, 1995.

[85] H. Igarashi, "On the property of the curl-curl matrix in finite element analysis with edge elements," *IEEE transactions on magnetics*, vol. 37, no. 5, pp. 3129–3132, 2001.

[86] M. R. Hestenes, E. Stiefel *et al.*, "Methods of conjugate gradients for solving linear systems," *Journal of research of the National Bureau of Standards*, vol. 49, no. 6, pp. 409–436, 1952.

[87] C. Lanczos, *An iteration method for the solution of the eigenvalue problem of linear differential and integral operators*. United States Governm. Press Office Los Angeles, CA, 1950.

[88] J. Liesen and Z. Strakos, *Krylov subspace methods: principles and analysis*. Oxford University Press, 2013.

[89] B. N. Parlett, D. R. Taylor, and Z. A. Liu, "A look-ahead lanczos algorithm for unsymmetric matrices," *Mathematics of computation*, vol. 44, no. 169, pp. 105–124, 1985.

[90] R. W. Freund, M. H. Gutknecht, and N. M. Nachtigal, "An implementation of

the look-ahead lanczos algorithm for non-hermitian matrices," *SIAM journal on scientific computing*, vol. 14, no. 1, pp. 137–158, 1993.

[91] R. W. Freund, "Krylov-subspace methods for reduced-order modeling in circuit simulation," *Journal of Computational and Applied Mathematics*, vol. 123, no. 1-2, pp. 395–421, 2000.

[92] L. Shieh and M. Goldman, "Continued fraction expansion and inversion of the cauer third form," *IEEE transactions on Circuits and Systems*, vol. 21, no. 3, pp. 341–345, 1974.

[93] Y. Gerstenmaier, W. Kiffe, and G. Wachutka, "Combination of thermal subsystems modeled by rapid circuit transformation," in *2007 13th International Workshop on Thermal Investigation of ICs and Systems (THERMINIC)*. IEEE, 2007, pp. 115–120.

[94] J. H. Krah, "Optimum discretization of a physical cauer circuit," *IEEE transactions on magnetics*, vol. 41, no. 5, pp. 1444–1447, 2005.

[95] E. Kuhn, C. Forgez, P. Lagonotte, and G. Friedrich, "Modelling ni-mh battery using cauer and foster structures," *Journal of power sources*, vol. 158, no. 2, pp. 1490–1497, 2006.

[96] S. R. Best, "The foster reactance theorem and quality factor for antennas," *IEEE Antennas and Wireless Propagation Letters*, vol. 3, no. 1, pp. 306–309, 2004.

[97] R. M. Foster, "A reactance theorem," *Bell System technical journal*, vol. 3, no. 2, pp. 259–267, 1924.

[98] T. Fry, "The use of continued fractions in the design of electrical networks," *Bulletin of the American Mathematical Society*, vol. 35, no. 4, pp. 463–498, 1929.

[99] O. Brune, "Synthesis of a finite two-terminal network whose driving-point impedance is a prescribed function of frequency," Ph.D. dissertation, Massachusetts Institute of Technology, 1931.

[100] J. Gyselinck and P. Dular, "A time-domain homogenization technique for laminated iron cores in 3-d finite-element models," *IEEE transactions on magnetics*, vol. 40, no. 2, pp. 856–859, 2004.

[101] A. Berthault, D. Rousselle, and G. Zerah, "Magnetic properties of permalloy microparticles," *Journal of magnetism and magnetic materials*, vol. 112, no. 1-3, pp. 477–480, 1992.

[102] M. Y. Koledintseva, J. L. Drewniak, R. E. DuBroff, K. N. Rozanov, and B. Archambeault, "Modeling of shielding composite materials and structures for microwave frequencies," *Progress In Electromagnetics Research*, vol. 15, pp. 197–215, 2009.

List of publications

Publications

Journal papers

(1) S. Hiruma, H. Igarashi, "Fast 3-D Analysis of Eddy Currents in Litz Wire Using Integral Equation," *IEEE Transactions on Magnetics*, vol. 53, no. 6, Art no. 7000704, Jan. 2017.

(2) S. Hiruma, Y. Otomo, H. Igarashi, "Eddy Current Analysis of Litz Wire Using Homogenization-Based FEM in Conjunction with Integral Equation," *IEEE Transactions on Magnetics*, vol. 54, no. 3, Art no. 7001404, Mar. 2018.

(3) S. Hiruma, H. Igarashi, "Fast computation of copper and iron losses using model order reduction," *International Journal of Applied Electromagnetics and Mechanics*, vol. 60, no. 1, pp.79-86, May 2019.

(4) S. Hiruma and H. Igarashi, "Time-Domain Analysis of Homogenized Finite-Element Method for Eddy Current Analysis With Reduced Unknown Variables," *IEEE Transactions on Magnetics*, vol. 56, no. 1, Art no. 7501604, Dec. 2019.

(5) S. Hiruma, H. Igarashi, "Homogenization Method Based on Cauer Circuit via Unit Cell Approach," *IEEE Transactions on Magnetics*, vol. 56, no. 2, Art no. 7505805, Feb. 2020.

(6) S. Hiruma, H. Igarashi, "Model Order Reduction for Linear Time-Invariant System With Symmetric Positive-Definite Matrices: Synthesis of Cauer-Equivalent Circuit," *IEEE Transactions on Magnetics*, vol. 56, no. 3, Art no. 7400608, March 2020.

(7) S. Hiruma, H. Igarashi, "Synthesis of Equivalent Circuit from Homogenized FE Equation using Model Order Reduction," 電気学会論文誌 B, vol. 140, no. 2, pp. 134-139, 2020.

Proceedings of international conferences

(1) S. Hiruma, H. Igarashi, "Homogenization Based on Continued Fraction: Application to Magnetic field Analysis," JSST2018, OS2, Muroran, Japan, Sep. 2018.

(2) W. She, S. Hiruma, H. Igarashi, "Efficient and Accurate Iron Loss Computation of

Permanent-Magnet Synchronous Motors Using Behavior Model," JSST2019, pp.260-263, Miyazaki, Japan, Nov. 2019.

(3) H. Sato, S. Hiruma, H. Igarashi, "Multi-Phase Topology Optimization Using Radial Basis Function for Design of Permanent Magnet Motor," JSST2019, pp. 231-234, Miyazaki, Japan, Nov. 2019.

Related papers

(1) S. Fujita, S. Hiruma and H. Igarashi, "Time-Domain Analysis of Magnetically Shielded Wire Coils Using Homogenized Finite-Element Method," *IEEE Transactions on Magnetics*, vol. 56, no. 2, Art no. 7506504, Feb. 2020.

Appendix A

S-fraction representation

Let us consider the reduced-order transfer function

$$\mathcal{H}_n(s) = \kappa_1 \boldsymbol{e}_1^\top (I - sT_n)^{-1} \boldsymbol{e}_1 \tag{A.1}$$

where

$$T_n = \begin{bmatrix} -\kappa_1\kappa_2 & \kappa_3\kappa_2 & & 0 \\ \kappa_1\kappa_2 & -\kappa_3(\kappa_2+\kappa_4) & \ddots & \\ & \ddots & \ddots & \\ & & -\kappa_{2n-3}(\kappa_{2n-4}+\kappa_{2n-2}) & \kappa_{2n-1}\kappa_{2n-2} \\ 0 & & \kappa_{2n-3}\kappa_{2n-2} & -\kappa_{2n-1}(\kappa_{2n-2}+\kappa_{2n}) \end{bmatrix}. \tag{A.2}$$

In this chapter, we demonstrate that (A.1) is equivalent to (3.112). First, (A.1) can be written as

$$\mathcal{H}_n(s) = \frac{\kappa_1 |A_{n-1}|}{|A_n|}, \tag{A.3}$$

where $|A_n|$ is the determinant of $I - sT_n$, and

$$|A_{n-1}| = \begin{vmatrix} 1+s\kappa_3(\kappa_2+\kappa_4) & -s\kappa_5\kappa_4 & & 0 \\ -s\kappa_3\kappa_4 & 1+s\kappa_5(\kappa_4+\kappa_6) & \ddots & \\ & \ddots & \ddots & \\ & & 1+s\kappa_{2n-3}(\kappa_{2n-4}+\kappa_{2n-2}) & -s\kappa_{2n-1}\kappa_{2n-2} \\ 0 & & -s\kappa_{2n-3}\kappa_{2n-2} & 1+s\kappa_{2n-1}(\kappa_{2n-2}+\kappa_{2n}) \end{vmatrix}. \tag{A.4}$$

$|A_{n-1}|$ is the (1,1) cofactor of A_n. The cofactor expansion along the first column of A_n gives:

$$|A_n| = (1+s\kappa_1\kappa_2)|A_{n-1}| - s^2\kappa_1\kappa_2^2\kappa_3|A_{n-2}|. \tag{A.5}$$

By substituting it into (A.3), we obtain

$$\begin{aligned}
\mathcal{H}_n(s) &= \frac{\kappa_1|A_{n-1}|}{(1+s\kappa_1\kappa_2)|A_{n-1}| - s^2\kappa_1\kappa_2^2\kappa_3|A_{n-2}|} \\
&= \cfrac{1}{\cfrac{1}{\kappa_1} + \cfrac{s\kappa_2|A_{n-1}| - s^2\kappa_2^2\kappa_3|A_{n-2}|}{|A_{n-1}|}} \\
&= \cfrac{1}{\cfrac{1}{\kappa_1} + \cfrac{1}{\cfrac{|A_{n-1}|}{s\kappa_2|A_{n-1}| - s^2\kappa_2^2\kappa_3|A_{n-2}|}}} \\
&= \cfrac{1}{\cfrac{1}{\kappa_1} + \cfrac{1}{\cfrac{1}{s\kappa_2} + \cfrac{\kappa_3|A_{n-2}|}{|A_{n-1}| - s\kappa_2\kappa_3|A_{n-2}|}}}.
\end{aligned} \tag{A.6}$$

We can find that the denominator of the last line of the continued fraction

$$|A_{n-1}| - s\kappa_2\kappa_3|A_{n-2}| = \begin{vmatrix}
1+s\kappa_3\kappa_4 & -s\kappa_5\kappa_4 & & & 0 \\
-s\kappa_3\kappa_4 & 1+s\kappa_5(\kappa_4+\kappa_6) & \ddots & & \\
& \ddots & \ddots & & \\
& & & 1+s\kappa_{2n-3}(\kappa_{2n-4}+\kappa_{2n-2}) & -s\kappa_{2n-1}\kappa_{2n-2} \\
0 & & & -s\kappa_{2n-3}\kappa_{2n-2} & 1+s\kappa_{2n-1}(\kappa_{2n-2}+\kappa_{2n})
\end{vmatrix} \tag{A.7}$$

has the equivalent form to $|A_n|$. Therefore, we can deduce

$$\begin{aligned}
\mathcal{H}_n(s) &= \frac{\kappa_1|A_{n-1}|}{|A_n|} \\
&= \left[0; \frac{1}{\kappa_1}, \frac{1}{s\kappa_2}, \frac{\kappa_3|A_{n-2}|}{|A_{n-1}| - s\kappa_2\kappa_3|A_{n-2}|}\right] \\
&= \left[0; \frac{1}{\kappa_1}, \frac{1}{s\kappa_2}, \frac{1}{\kappa_3}, \frac{1}{s\kappa_4}, \frac{\kappa_5|A_{n-3}|}{|A_{n-2}| - s\kappa_4\kappa_5|A_{n-3}|}\right] \\
&= \left[0; \frac{1}{\kappa_1}, \frac{1}{s\kappa_2}, \frac{1}{\kappa_3}, \frac{1}{s\kappa_4}, \dots, \frac{1}{\kappa_{2n-5}}, \frac{1}{s\kappa_{2n-4}}, \frac{\kappa_{2n-3}|A_1|}{|A_2| - s\kappa_{2n-4}\kappa_{2n-3}|A_1|}\right]
\end{aligned} \tag{A.8}$$

where

$$|A_2| = \begin{vmatrix}
1+s\kappa_{2n-3}(\kappa_{2n-4}+\kappa_{2n-2}) & -s\kappa_{2n-1}\kappa_{2n-2} \\
-s\kappa_{2n-3}\kappa_{2n-2} & 1+s\kappa_{2n-1}(\kappa_{2n-2}+\kappa_{2n})
\end{vmatrix}, \tag{A.9}$$

$$|A_1| = 1 + s\kappa_{2n-1}(\kappa_{2n-2}+\kappa_{2n}). \tag{A.10}$$

Thus, we have

$$\begin{aligned}
\frac{\kappa_{2n-3}|A_1|}{|A_2| - s\kappa_{2n-4}\kappa_{2n-3}|A_1|} &= \frac{\kappa_{2n-3}|A_1|}{(1+s\kappa_{2n-3}\kappa_{2n-2})|A_1| - s^2\kappa_{2n-3}\kappa_{2n-2}^2\kappa_{2n-1}} \\
&= \cfrac{1}{\cfrac{1}{\kappa_{2n-3}} + \cfrac{s\kappa_{2n-2}|A_1| - s\kappa_{2n-2}^2\kappa_{2n-1}}{|A_1|}} \\
&= \cfrac{1}{\cfrac{1}{\kappa_{2n-3}} + \cfrac{1}{\cfrac{|A_1|}{s\kappa_{2n-2}(|A_1| - s\kappa_{2n-2}\kappa_{2n-1})}}} \\
&= \cfrac{1}{\cfrac{1}{\kappa_{2n-3}} + \cfrac{1}{\cfrac{1}{s\kappa_{2n-2}} + \cfrac{\kappa_{2n-1}}{|A_1| - s\kappa_{2n-2}\kappa_{2n-1}}}} \\
&= \cfrac{1}{\cfrac{1}{\kappa_{2n-3}} + \cfrac{1}{\cfrac{1}{s\kappa_{2n-2}} + \cfrac{\kappa_{2n-1}}{1+s\kappa_{2n-1}\kappa_{2n}}}} \\
&= \cfrac{1}{\cfrac{1}{\kappa_{2n-3}} + \cfrac{1}{\cfrac{1}{s\kappa_{2n-2}} + \cfrac{1}{\cfrac{1}{\kappa_{2n-1}} + s\kappa_{2n}}}},
\end{aligned} \tag{A.11}$$

and

$$\mathcal{H}_n(s) = \left[0; \frac{1}{\kappa_1}, \frac{1}{s\kappa_2}, \frac{1}{\kappa_3}, \frac{1}{s\kappa_4}, \ldots, \frac{1}{\kappa_{2n-3}}, \frac{1}{s\kappa_{2n-2}}, \frac{1}{\kappa_{2n-1}}, \frac{1}{s\kappa_{2n}}\right]. \tag{A.12}$$

Appendix B

Impedance of slot conductor

Let us consider the infinite long homogeneous winding immersed in a slot, as shown in Fig. 4.38. A uniform current I flows in the winding. If the permeability of the iron is infinite, the magnetic field $\boldsymbol{H}$ generated by the current has only the x-component. Applying Amepère's law, we obtain

$$-\frac{H_x(y)}{\partial y} = \frac{b_c}{b} J \tag{B.1}$$

where J is a uniform current density in the winding. Note that we can consider the eddy current losses by the complex permeability $\langle \dot{\mu}_x \rangle$ owing the homogenization method. Therefore, the eddy current term σE_z does not appear in the equation. The equation can be solved to obtain

$$H_x(y) = -\frac{b_c J}{b} y + c \tag{B.2}$$

where c is a constant. From the boundary condition

$$H_x(0) = 0, \tag{B.3}$$

we obtain $c = 0$ and

$$H_x(y) = -\frac{b_c J}{b} y. \tag{B.4}$$

The impedance of the homogenization domain can be obtained from the complex power which can be computed as

$$\begin{aligned} Z = \frac{2P}{|I|^2} &= z_a z_t R_{dc} + \mathrm{j}\omega \int_{\Omega_\mathrm{h}} \langle \dot{\mu} \rangle |\boldsymbol{H}|^2 d\Omega / |I|^2 \\ &= z_a z_t R_{dc} + \mathrm{j}\omega \frac{\langle \dot{\mu} \rangle}{|I|^2} \int_0^{b_c} \int_0^{h_c} \int_0^{l} \frac{b_c^2 J^2}{b^2} y^2 dx dy dz \\ &= z_a z_t R_{dc} + \mathrm{j}\omega \langle \dot{\mu} \rangle \frac{h_c b_c l z_a^2 z_t^2}{3 b^2}. \end{aligned} \tag{B.5}$$